



Università degli Studi di Napoli *Federico II*



Università di Camerino



Consiglio Nazionale
delle Ricerche

DOTTORATO DI RICERCA IN QUANTUM TECHNOLOGIES

Ciclo XXXV

Coordinatore: prof. Francesco Tafuri

The Josephson Digital Phase Detector: principle, design and operation

Settore Scientifico Disciplinare FIS/03

Dottorando
Luigi Di Palma

Tutor
Prof. Davide Massarotti
Prof. Francesco Tafuri

Anni 2019/2023

Contents

| | | |
|----------|--|-----------|
| 1 | Superconducting circuits and qubits | 8 |
| 1.1 | Superconductivity | 9 |
| 1.2 | Josephson junctions | 9 |
| 1.3 | Superconducting Qubits | 12 |
| 1.3.1 | Advantages and Disadvantages of the superconducting quantum platform | 14 |
| 1.4 | Single-Flux-Quantum Logic | 16 |
| 2 | Readout in superconducting quantum bits | 19 |
| 2.1 | Criteria for superconducting qubit readout | 19 |
| 2.2 | Dispersive Measurement | 21 |
| 2.3 | Heterodyne detection | 22 |
| 2.3.1 | Scalability in heterodyne detection technique | 26 |
| 2.4 | The Josephson Photon Multiplier (JPM) | 27 |
| 2.4.1 | SFQ architectures to detect the JPM state | 29 |
| 3 | The Josephson Digital Phase detection (JDPD) | 32 |
| 3.1 | Device model | 34 |
| 3.2 | Principle of operations | 36 |
| 3.3 | Study of the detection protocol in classical regime | 38 |
| 3.4 | Study of the detection protocol in quantum regime | 42 |
| 3.5 | Asymmetries correction | 48 |
| 3.6 | JDPD technique applied to superconducting qubit readout | 50 |
| 4 | JDPD chip design | 54 |
| 4.1 | JDPD coupled to a CPW resonator | 54 |
| 4.2 | JDPD coupled to a lumped RLC resonator | 58 |
| 4.3 | Towards a scalable platform: JDPD-SFQ architecture | 62 |
| 4.3.1 | SFQ Comparator coupled to JDPD | 63 |
| 4.3.2 | SFQ Flux generator coupled to JDPD | 67 |
| 5 | Measurements and Data Analysis | 70 |
| 5.1 | Experimental technique | 70 |
| 5.2 | Experimental setup | 71 |
| 5.3 | Spectroscopy calibration | 73 |
| 5.4 | Double well demonstration | 76 |

| | | |
|-----------------------------|---|------------|
| 5.5 | Symmetry point determination | 80 |
| 5.6 | Phase detection demonstration | 83 |
| 5.6.1 | Input signal through dc lines | 86 |
| 5.6.2 | Input signal through input line | 88 |
| List of Publications | | 108 |

Abstract

Quantum computing platforms based on superconducting qubits have emerged as one of the most promising candidates in the race to build a large-scale quantum computer. However, while the performance of small superconducting quantum processors has advanced the threshold necessary for fault tolerance, the current technique to control and readout the qubit state imposes severe system scaling challenges. Within this framework, digital control based on energy-efficient superconducting Single Flux Quantum (eSFQ) logic, is being adapted to perform qubit control and readout for scalable quantum architectures, thus leading to the development of innovative concepts for control and benchmarking in this linked digital-quantum hybrid system.

I present a new SFQ-compatible readout technique based on a flux-switchable Quantum Flux Parametron (QFP), which is capable of discriminating between two phase values of a coherent input tone. In the proposed detection protocol, the QFP is at first flux-biased into harmonic configuration to sense the input coherent tone, then quickly flux-switched to a bistable configuration to store the information on the input tone phase. We name our device Josephson Digital Phase Detector (JDPD), since the result of the detection is naturally encoded in the occupation probability of a phase particle in either of the wells in the bistable configuration.

In this work, the JDPD approach has been completely investigated from a theoretical and experimental perspective. Numerical simulations demonstrate that detection can be accomplished in a time scale of few nanoseconds with fidelity approaching 1. During the operations, the JDPD is not required to be in resonance with the input signal frequency. Thus, the device can be designed to have precise energy transitions, which reduce the backaction on the surrounding circuitry. Theoretical predictions are supported by experimental outcomes obtained on several devices. Digital phase detection has been demonstrated in a wide range of operation regimes and device configurations up to a frequency of 1 GHz .

As a future perspective, I will discuss a possible implementation of this device to readout the state of a superconducting qubit, which can be accomplished by properly adjusting the JDPD design parameters. Therefore, we envision the JDPD as part of a more complex architecture, in which the classical qubit control, measurement, and data processing are performed by a classical SFQ processor. This approach would have tremendous advantages to superconducting quantum systems' scalability, which remains a big engineering challenge to realize practical

error-corrected quantum computers.

Introduction

Quantum computing platforms based on superconducting circuits have emerged as one of the most promising candidates in the race to build a large-scale quantum computer[1]. Superconducting qubits have achieved both gate [2, 3] and measurement fidelity [4] at the threshold for fault-tolerant operation [5]. Recent demonstrations of quantum supremacy [6] and surface codes [7, 8] stimulate efforts to build larger multiqubit chips, compatible with robust error correction protocols.

However, theoretical estimates indicate that a practical error-corrected quantum computer will require more than one million physical qubits [3, 9]. This goal is quite hard to achieve given the actual experimental technique involving microwave pulses to control and readout the state of a superconducting qubit. In fact, to deliver signals in and out of the fridge, this approach requires microwave electronics and components, such as high-bandwidth cables from room temperature (RT) to millikelvin temperatures, and bulky non-reciprocal microwave insulators, that bring severe technical and economic challenges to system scaling [10]. It is highly desirable to integrate the control and measurement circuitry in the cryostat in order to reduce wiring heat load, power consumption, and the overall system footprint, and to allow for low-latency operations [3, 9, 11].

A possible candidate for such cold control system is energy-efficient superconducting Single Flux Quantum (SFQ) logic [12–15], in which classical bits of information are stored in propagating fluxons, voltage pulses whose time integral equals the superconducting flux quantum $\Phi_0 = h/2e$ [16]. Superconducting SFQ circuits can be proximally located to the qubit chips due to their low power. The ability to operate at very high speed (tens of gigahertz clock) opens a way for digitizing and fast processing qubit output data for error correction and generation of qubit control signals [9, 15].

In this thesis, I present a new SFQ-compatible readout technique based on a flux-switchable Quantum Flux Parametron (QFP), which is capable of discriminating between two phase values of a coherent input tone at GHz frequency. For instance, such tone can be a readout pulse whose phase encodes the outcome of a qubit measurement. In our readout protocol, the QFP is at first flux-biased into harmonic configuration to sense the input coherent tone, then quickly flux-switched to a bistable configuration to store the information on the input tone phase. We name our device Josephson Digital Phase Detector (JDPD), since the result of the detection is naturally encoded in the occupation probability of a phase particle in either of the wells in the bistable configuration.

The JDPD readout technique is characterized by unique features. First of all, the JDPD is not required to be in resonance with the qubit or cavity. Thus, the device can be designed to have precise energy transitions in order to reduce as much as possible the backaction on the rest of the circuit. The JDPD shows robustness with respect to asymmetries or parameters spread that could, in principle, affect the device's performance. One can recover the ideal operating point by adjusting properly the fluxes threading the device's loops.

When operated by co-located SFQ circuits, the JDPD can accomplish the operations in a time scale of nanoseconds and the measurement outcomes can be converted naturally into classical bits of information in form of propagating fluxons. We also estimate that a single detector can be employed to readout multiple qubits at a time, which is of particular relevance in order to reduce the system footprint.

All these properties are discussed in detail in this work, which is organized as follows. In Chapter 1, I will briefly introduce the main concepts of superconducting quantum computation, with particular emphasis on the Single Flux Quantum (SFQ) logic proposed as a solution to enhance the scalability of a quantum processor.

Chapter 2 is dedicated to illustrating the main techniques for readout the state of a superconducting qubit. I will focus on the dispersive readout approach, based on heterodyne detection, which is suitable in any kind of superconducting qubits. This technique is widely adopted in literature and allows to achieve high fidelity levels [4]; however, the massive use of bulky microwave components brings severe problems in the realization of large-scale quantum processors [9, 11, 15].

In the framework of SFQ-compatible circuits to enhance the system scalability, I will introduce the Josephson Photon Multiplier (JPM), proposed as a scalable approach to accomplish digital superconducting qubit readout. Despite the advantages of this technique, some drawback limits the JPM application to large systems. To overcome these difficulties, I present the JDPD in Chapter 3. I will describe the circuit model and its theoretical background. The main features of our detection technique will be illustrated, starting from numerical analysis performed by using PSCAN2 [17] and QuTip[18]. According to the parameters determined in simulations, in Chapter 4 I will present the JDPD chip layouts that I have designed to investigate experimentally the feasibility of our readout approach.

The experimental characterization will be reported in Chapter 5. I will discuss our experimental technique to set and readout the JDPD state, and the main part of the experimental setup. In order to prepare the JDPD for phase detection, I will present the necessary steps to calibrate the system. Finally, I will exhibit the results of phase detection, performed by exploring various regimes and configurations, demonstrated up to a frequency of 1 *GHz*.

Chapter 1

Superconducting circuits and qubits

Quantum mechanics has revolutionized our understanding of nature. Its description of nature is full of unexpected rules that remain counterintuitive even after over a century of experimental confirmations. In the past decades, there were rapid developments in technology and control over quantum systems. These technologies aim to harness the specific properties of quantum mechanics for real-life applications such as secure communication [19], high-precision sensing [20], and information processing [21]. These pioneering goals have driven a tremendous effort in the implementation of quantum devices in a variety of platforms such as trapped ions [22–25], ultracold atoms [26–28], electron spins in silicon [29–31] and quantum dots [32–34], nitrogen-vacancies in diamonds [35, 36] polarized photons [37–39], and superconducting circuits [40]. Each platform has specific advantages over the others; for example, photons seem to be more appropriate for transmitting quantum information [37–39], while atoms can serve as long-lived quantum memories [26–28]. Superconducting circuits have gained a lot of attention as a flexible platform for scalable quantum computation [9, 41, 42]. Compared to other platforms, which all encode quantum information in microscopic systems, superconducting circuits exhibit quantum mechanical effects despite they are macroscopic in size; this has led to the notion of macroscopic quantum effects [43] in order to describe these phenomena [44, 45]. An advantage of superconducting circuits is the fact that microscopic features such as energy spectra, coupling strengths, and coherence rates depend on macroscopic circuit parameters and can be properly designed and engineered [46, 47]. For this reason, superconducting quantum circuits are sometimes referred to as artificial atoms. Apart from computational goals, superconducting devices are a powerful architecture to explore quantum physics and can serve as a testbed for fundamental questions in science. This is due, in part, to the features of quantum systems composed of artificial atoms, which are relatively simple to control. This creates opportunities for investigating complex quantum systems using versatile superconducting circuit design.

1.1 Superconductivity

For an integrated circuit to behave quantum mechanically, the first requirement is an extremely low level of dissipation [41]. Superconductors show zero dc electric resistance and perfect diamagnetic behaviour. The reason, as explained by the theory of Bardeen, Cooper and Schrieffer (BCS), is that in a given superconductor electrons are condensed in pairs called Cooper pairs, which have charge $2e$, mass $2m_e$ and commonly spin-zero, and are responsible for carrying a supercurrent. The condensate is described by a unique macroscopic wavefunction $\Psi(\vec{r}, t)$. Being a complex function the wavefunction $\Psi(\vec{r}, t)$ can be written as the product of an amplitude and a factor involving the phase φ :

$$\Psi(\vec{r}, t) = |\Psi(\vec{r}, t)|e^{i\varphi} \quad (1.1)$$

which is related to the supercurrent density J_s [46–48].

The fact that the system condensates in a single macroscopic state also leads to the phenomenon of flux quantization, which will turn into an essential tool for engineering various types of superconducting qubits [1]. When a closed ring is cooled through its superconducting transition temperature in a magnetic field and the field is then switched off, the magnetic flux Φ in the ring — maintained by a circulating supercurrent — is quantized in integer values of the flux quantum $\Phi_0 \equiv h/2e$. This quantization arises from the requirement that $\Psi(\vec{r}, t)$ is single-valued [1].

1.2 Josephson junctions

Other intriguing phenomena arise when two superconductors are weakly coupled through a sufficiently thin non-superconducting barrier, as shown in Fig. 1.1. In this situation, it's possible to observe the tunnelling of Cooper-pair electrons through the barrier. This phenomenon is known as the *Josephson Effect* [49]. The dynamic of a Josephson junction is governed by the Josephson relations which link the phase difference $\varphi = \varphi_R - \varphi_L$ between the wavefunctions associated with the left and right superconducting electrodes $\Psi_L(\vec{r}, t)$ and, respectively, $\Psi_R(\vec{r}, t)$ to current and voltage across the junction's electrodes :

$$\begin{aligned} I &= I_c \sin(\varphi) \\ V &= \frac{\Phi_0}{2\pi} \frac{d\varphi}{dt}. \end{aligned} \quad (1.2)$$

Here I_c is the critical current, i.e the maximum current that the junction can sustain without dissipation and $\Phi_0 = 2.067 \cdot 10^{-15} \text{ Wb}$ is the flux quantum. The variable φ is nothing else than an electromagnetic flux Φ in dimensionless units [41, 42]:

$$\varphi = \Phi \text{ mod } 2\pi. \quad (1.3)$$

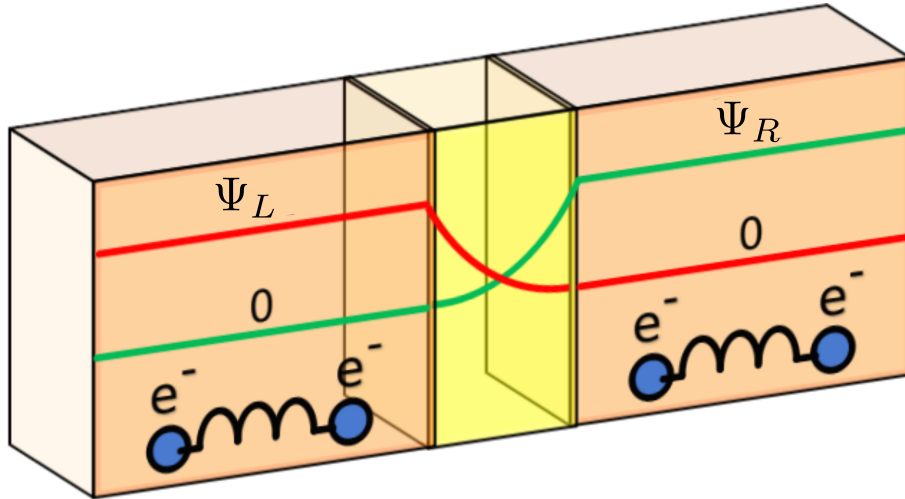


Figure 1.1: Sketch of a tunnel Josephson junction with an insulating barrier. The red curve represents the wavefunction behaviour of the left electrodes Ψ_L , while the green line refers to the wavefunction Ψ_R

More generally, combining the Josephson equations [47], it can be shown that a Josephson element behaves as a non-linear inductor [41, 42] :

$$L(\varphi) = \frac{\Phi_0}{2\pi I_c} \frac{1}{\cos(\varphi)} \quad (1.4)$$

This is the manifestation, at the level of collective electrical variables, of the inertia of Cooper pairs tunnelling across the insulator [41].

A more general model to describe the dynamics of a Josephson junction consists in the *Resistively and Capacitively Shunted Junction* (RCSJ) model [47]. In this framework, the current flowing through a Josephson junction is given by the sum of:

- $I_S = I_c \sin(\varphi)$, corresponding to the Josephson contribution
- $I_N = V/R$, related to the junction resistive contribution
- $I_C = CdV/dt$, associated with the charge accumulation at the interfaces between the superconducting electrodes and the barrier, that generates a displacement current

Considering an external bias current attached to Josephson junction I_b and the Josephson equations defined in Eqs. 1.2, the total current contribution is:

$$I_b = I_s + I_N + I_C = I_c \sin(\varphi) + \frac{2e}{\hbar R} \frac{d\varphi}{dt} + \frac{2eC}{\hbar} \frac{d^2\varphi}{dt^2}. \quad (1.5)$$

The latter equation points out that the phase dynamics of a current-biased Josephson junction is analogue to the dynamics of a damped particle, referred to as phase particle, subject to a washboard potential [43]:

$$U(\varphi) = -\frac{\Phi_0}{2\pi} \left(I_c \cos(\varphi) + I\varphi \right) \quad (1.6)$$

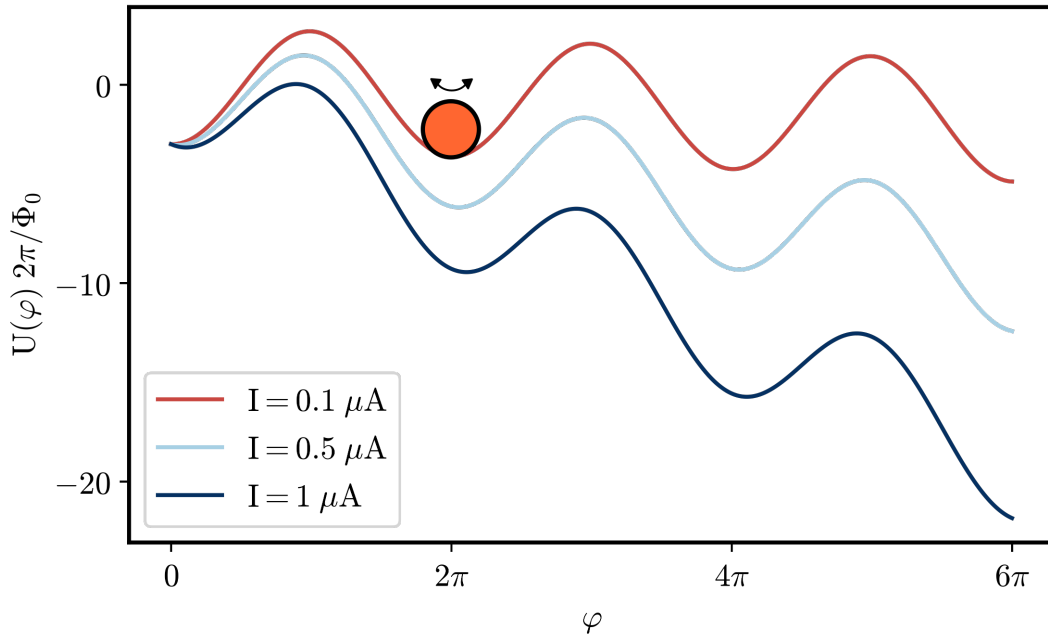


Figure 1.2: Washboard potential in the case of $I_C = 3 \mu A$ and for three values of the bias current. Increasing the bias level, the potential tilts more with respect to the x-axis. In absence of thermal and quantum fluctuations, the phase particle escapes from the well when $I = I_c$.

Initially, when $I_b = 0$, the phase particle oscillates in the minimum of one of these wells with mass m :

$$m = C \quad (1.7)$$

characterized by the plasma frequency:

$$\omega_p = \frac{1}{\sqrt{L_j C}} = \sqrt{\frac{2eI_c}{\hbar C}} \quad (1.8)$$

When the $I_b > I_c$, the phase particle escapes from the well, and a non-zero voltage difference is observed across the junction. The phase particle is essentially rolling down the tilted washboard potential with a velocity proportional to $d\varphi/dt$, leading to a measurable voltage according to the second Josephson equation in Eq.1.2.

Reducing I_b below I_c , the inertia of the phase particle, related to the junction capacitance C can keep the junction in the voltage state until a lower, re-trapping current is reached. This determines a hysteretic behaviour in the current-voltage (IV) characteristic that depends on the junction parameters. In particular, we can introduce the Stewart-McCumber parameter β , defined as [50]:

$$\beta = I_c R^2 C \frac{2e}{\hbar} \quad (1.9)$$

When $\beta > 1$, a hysteretic IV characteristic is observed.

In the digital logic discussed later in Section 1.4, the information is generated and

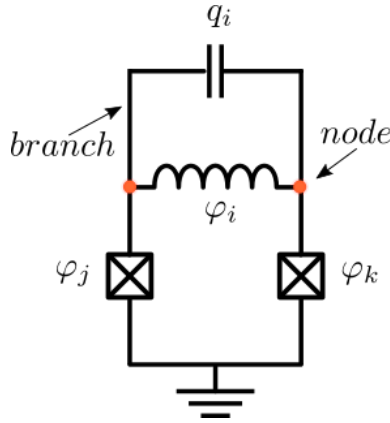


Figure 1.3: An electrical circuit consisting of two-pole elements forming the branches of the network and meeting at nodes. Loops are formed when there is more than one path between two nodes. Branch fluxes φ_i and branch charges q_i are indicated.

transmitted through the switching of JJs. Consequently, it is preferable that the junction return to its superconducting condition as soon as possible without the need to change any bias currents. Therefore for digital applications, junctions with $\beta \leq 1$ are typically employed.

1.3 Superconducting Qubits

Usually, we think of electrical circuits in the domain of classical physics, but if the circuits are made of low-loss superconducting components, then they show a quantum mechanical behaviour at sufficiently low temperatures [41, 42, 51].

A quantum mechanical description of electrical circuits can be obtained from the quantization of the classical Hamiltonian, as widely discussed in Refs. [1, 41, 42]. The classical Hamiltonian is composed of the energy contributions of each electrical element expressed in terms of the branch fluxes φ_i and branch charges q_i , as shown in Fig. 1.3.

In our superconducting circuit toolbox there are three fundamental elements to work with: capacitors, inductors and Josephson junctions. Each of them is a lossless energy storage element and contributes either to the kinetic or the potential energy terms in the Hamiltonian description of the circuit.

The energy storage formula for the inductance L is:

$$E_L = \left(\frac{\Phi_0}{2\pi} \right)^2 \frac{\varphi^2}{2L} \quad (1.10)$$

where φ is the normalized magnetic flux defined in Eq.1.3. Thus, the inductors contribute harmonically to the potential energy in the φ coordinates.

The kinetic energy is:

$$E_c = \frac{Q^2}{2C} \quad (1.11)$$

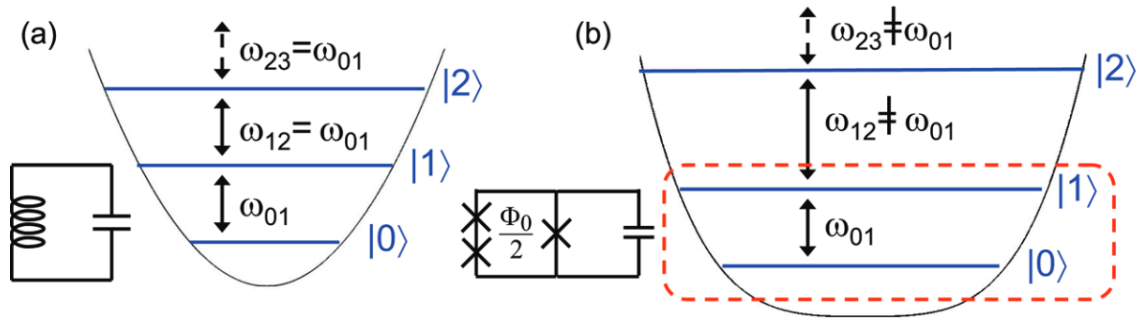


Figure 1.4: Adapted from [51]: (a) Harmonic oscillator formed by an inductor and a capacitor forms a quantum system in which all energy levels are equally spaced. (b) When adding Josephson junctions, the system becomes anharmonic, giving rise to energy levels that are not equally spaced. (Dashed red box) The lowest two levels are then identified by a unique frequency, allowing the system to be used as a qubit.

is directly analogous to the kinetic energy $p^2/2m$ of particles in mechanics where the charge Q is the momentum p , and capacitance C is the mass.

However, in a circuit composed only of inductors and capacitors, it's not possible to observe non-trivial quantum effects since the energy transitions cannot be distinguished from each other [41].

The Josephson junctions play a fundamental role in superconducting circuits because they act as nonlinear inductors and affect the potential so that quantum levels are not equally spaced, as shown in Fig. 1.4. In this way, it's possible to isolate a 0–1 transition that can be used as a qubit. The energy stored in the Josephson Junction can be computed from Eq.1.2 and it's equal to:

$$E_J = \int_t^{-\infty} I(t')V(t')dt' = -\frac{I_C\Phi_0}{2\pi}\cos(\varphi) \quad (1.12)$$

Given the fundamentals “bricks” discussed above, we can distinguish different elementary types of superconducting qubits, classified by the ratio E_J/E_C [52, 53], as represented in Fig. 1.5:

- **Charge qubit:** A charge qubit consists of a small superconducting island connected to a large superconducting reservoir via a Josephson junction, which leads to $E_J/E_C < 1$. A capacitively coupled gate voltage controls the charge offset n_g on the island, and it is used to tune the qubit frequency [55]. The quantum states correspond to charge states, which differ from each other on the number of Cooper pairs on the island.
- **Flux qubit:** Flux qubits are implemented in a looped superconducting circuit interrupted by one or more Josephson junctions [1] and are characterized by $E_J/E_C > 50$. The two quantum states correspond to currents circulating anticlockwise and clockwise in the loop. The device state can be controlled by applying an external magnetic flux.

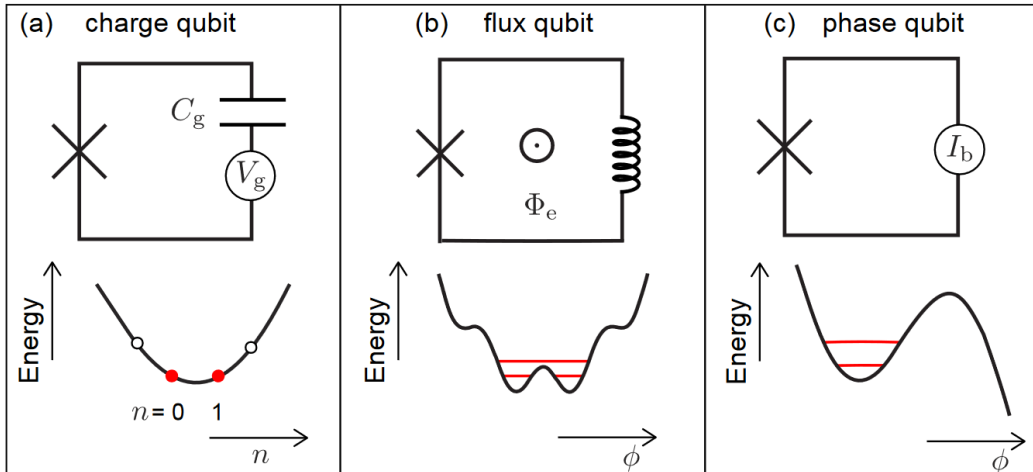


Figure 1.5: Adapted from [54]: Schematic diagrams of the three basic superconducting quantum circuits and their potential energies. (a) Charge qubit, (b) flux qubit, and (c) phase qubit

- Phase qubit:** This circuit consists of a large Josephson junction with $E_J/E_C \gg 1$. The tilted washboard shape of the junction's potential energy is controlled through an applied dc bias current I_b or, alternatively, by a flux threading the phase-qubit loop [54]. The phase qubit uses the lowest two energy levels in the local minimum of the washboard potential [1].

To achieve long coherence times, which is a measure of how well a qubit's quantum state persists with time, the three basic superconducting qubits discussed above have been further improved and modified according to various types of superconducting-circuit designs [54], as in the case of the fluxonium [56–58] and the transmon [59–61].

Cavity resonators also play a key role in superconducting quantum circuits [51], since they constitute additional quantum harmonic oscillator degrees of freedom. Resonators can interact with the qubit to stabilize its frequency and to serve as memory [62], to allow transfer to long-lived memory states, mediate coherent interactions with other qubits [63], and to provide an effective bandpass filter to reject most of the environmental noise [64].

It's important to define the quality factor Q of the resonator, related to its intrinsic damping [65]. Typical cavities adopted in superconducting resonators have large values of Q ($10^6, 10^7$), which indicate low values of losses [66].

1.3.1 Advantages and Disadvantages of the superconducting quantum platform

Superconducting circuits allow enormous flexibility in choosing the parameters for quantum circuits because their physical properties, such as energy transitions, are determined and tuned by a suitable design rather than by constants

of nature.

Beyond this important advantage, there are some others that make this platform very attractive to develop a large-scale quantum computer. Of course, superconducting circuits have some drawbacks that should be overcome. In the next, the main advantages and disadvantages are reported.

Advantages

- **Easy control in the microwave regime:** Superconducting quantum circuits typically work in the range $3 - 20 \text{ GHz}$ [41] and at a temperature of 20 mK . In fact, in order to observe quantum effects, the spacing between energy levels must be larger than the typical energy $k_B T$ of thermal fluctuations, where T is the temperature of the system. For example, at 1 K these noise fluctuations correspond to about 20 GHz . One possibility to reduce the noise effects is, in principle, increasing the working frequency of the superconducting devices. However, this is not feasible because, according to the Mattis Bardeen formula [67], the residual resistivity of a BCS superconductor increases linearly with frequency and becomes dominant at $\omega/2\pi \simeq 2\Delta/h$.

A different solution is to use a conventional dilution refrigerator which attains temperatures of ten to a few tens of mK. In this way at $T = 20 \text{ mK}$, we would need a frequency of 3 GHz to keep the thermal occupation of the qubit's excited state below a part in one thousand [41, 42]. This microwave frequency range is readily accessible with relatively cheap commercial electronic hardware such as spectrum analyzers, sources, and even arbitrary waveform generators.

- **Easy to fabricate:** Due to the prevalence of CMOS technology, the fabrication of electrical circuits is an extremely well-developed industry. Even the most complicated superconducting qubit chips requiring seven layers of lithography can be made in a couple of days. Realization by photo and e-beam lithography also directly enables scaling to larger system sizes on chip.
- **High on chip connectivity:** Thanks to fabrication performed by photo and e-beam lithography, the on-chip connectivity of superconducting quantum circuits is subject only to the constraints of on-chip wiring and this allows for very complex connection schemes as in the case of the DWave "Chimera Graph" [68].
- **Fast Gate Operation:** Superconducting qubits have fast gate times, which means that similar computations can be performed quicker than on other quantum platforms [69]. This is important since useful computations will likely have millions of logical operations.

Disadvantages

- **Not true 2-level systems** Superconducting qubits are not true 2-level systems. The one-dimensional potentials admit higher quantum levels which can be accidentally populated during the quantum gates operations. Unwanted transitions to higher levels ruin information processing protocols, as the qubit leaves the expected space of states.
- **Spread of fabrication parameters** Contrary to qubits that rely on individual particles as their basis, the individual qubits in a large array of superconducting qubits aren't all guaranteed to be equivalent. Inefficiency during the manufacturing process of superconducting qubits can lead to devices with different inductance and capacitance. When the qubit oscillation frequency can't be tuned in situ, this poses a severe challenge.
- **Scalability** Despite the actual quantum processors have surpassed the necessary fault tolerance threshold [70], significant scaling challenges still need to be addressed before a larger quantum computing system can be constructed [3]. Current systems are built by connecting cryogenic quantum chips using expensive, lossy, meters-long coaxial cables with qubit control and measurement by using classical electronics at room temperature. This approach brings severe technical and economic challenges to system scaling such as the heat load, latency, and noise associated with delivering signals [9, 11].

A possible solution, proposed in the works [9, 10, 14, 15], explores the use of superconducting Single Flux Quantum circuits, that can be proximally located to the qubit chips, due to their low power. This approach allows the reduction of connections from room temperature to the qubit stage, with enormous benefits to system scalability.

1.4 Single-Flux-Quantum Logic

Single Flux Quantum (SFQ) logic is a type of digital logic that uses superconducting circuits to perform digital operations [48].

Superconducting digital circuits were explored as early as the 1950s [71] and advanced quickly with the discovery of the Josephson effect in the mid-1960s [72, 73].

There are different implementations of superconducting devices to perform digital operations [46, 48], but Rapid Single-Flux-Quantum (RSFQ) became the dominant logic family over the following several decades [16].

In RSFQ logic, the basic unit of information is a single flux quantum (SFQ) pulse, which is a very fast voltage pulse with a quantized area [16, 74, 75]:

$$\Phi_0 = \int V(t) dt. \quad (1.13)$$

1.4. SINGLE-FLUX-QUANTUM LOGIC

These pulses can be generated, reproduced and memorized by elementary circuits comprising Josephson junctions [16]. Typically, these junctions are critically damped ($\beta = 1$) with a shunt resistor, which is the optimal value to achieve the faster switching time [16, 74, 76].

Considering the standard characteristics of the JJs adopted in these circuits, the SFQ pulses have a height $V = I_C R_n \simeq 1 \text{ mV}$, which leads, starting from Eq. 1.13, to pulse length of the order of a few picoseconds [16, 74, 76]. This is a very low value and allows the circuit to be clocked at very high speeds. For instance, the highest reported RSFQ circuit operates at 770 GHz, which is two orders of magnitude larger than the clock speed used in semiconductor devices [77].

Furthermore, in the eRSFQ (efficient-RSFQ) family of logic circuits, characterized by a zero static energy dispersion, the dissipation per switch is around $10^{-20} J$, which is an extremely low value compared, for example, with the typical dissipation observed in semiconductor devices [12, 13, 46].

The SFQ logic has been initially proposed as a valid alternative to the semicon-

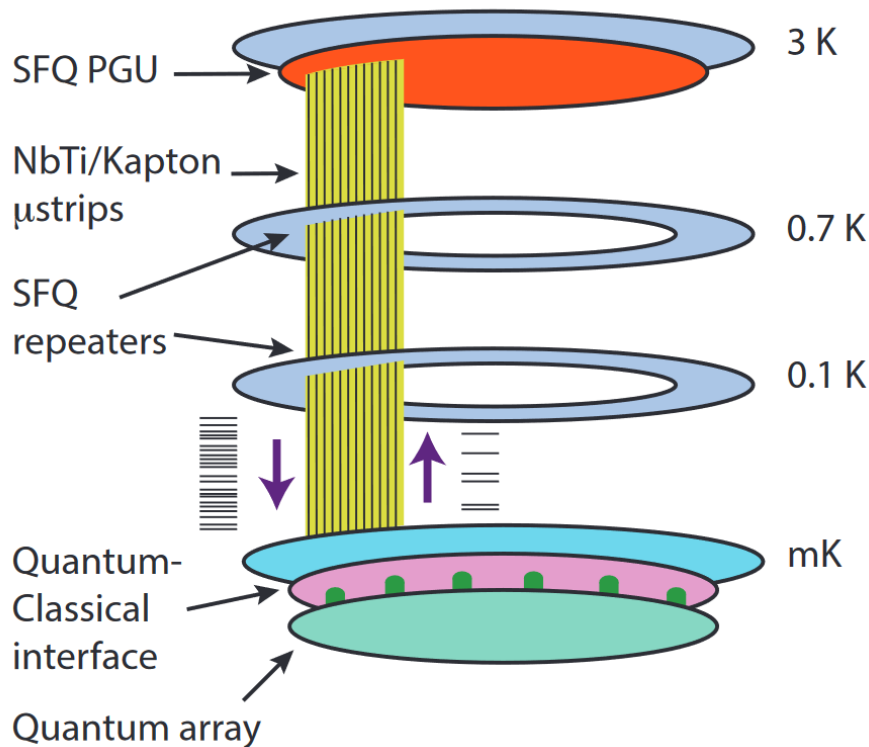


Figure 1.6: Adapted from Ref. [9]: Conceptual view of hybrid quantum-classical scalable quantum computing systems consisting of superconducting qubits and classical SFQ chips located at various temperature stages of a dilution refrigerator

ductive CMOS technology, given its enormous advances in terms of clock speed and power dissipation [16, 75]. Later, the advent of qubits based on superconducting circuits make the SFQ architectures an obvious candidate for the cold control of superconducting quantum processors [9, 10, 15]. There are a lot of the-

oretical and experimental studies involving the SFQ platform to manipulate and readout the state of a superconducting qubit [3, 78]. Following this approach, in this manuscript, I will propose a new technique to perform the measurement of the qubit state, based on a superconducting circuit that operates as a buffer between the quantum chip and a cold SFQ processor ¹.

¹any references to SFQ in this thesis imply eRSFQ

Chapter 2

Readout in superconducting quantum bits

Fast and accurate measurement of qubits is a key step for having a functional quantum computer. High-fidelity gates and long-lived qubits are not useful in a quantum algorithm if the final state cannot be accurately measured. For error-correcting codes to be useful, qubits and their errors must be measured in a timescale that is short compared to the coherence time of the qubits.

In this Chapter, I will describe the standard technique, based on heterodyne detection, to measure the state of superconducting qubits. Despite this approach is widely used and allows detection with very high fidelity [6], it poses serious problems to the quantum processor's scalability [9].

A possible solution to overcome this problem involves the integration of a cold SFQ processor to control the quantum processor. In this framework, a recent technique, based on a Josephson Photon Multiplier (JPM), has been exploited to measure the state of a superconducting qubit. The JPM performs a digital readout of the qubit state by projective measurement of the microwave cavity pointer states [79–81]. This technique is compatible with the SFQ-logic since the resulting output can be naturally converted into propagating fluxons [81]. Despite the JPM has the potential to provide a scalable system to measure the qubit state in large superconducting quantum processors, this approach to qubit readout has some drawbacks that restrict its real applicability. This motivated us to explore a different readout technique, based on the Josephson Digital Phase Detector, that will be presented in Chapter 3.

2.1 Criteria for superconducting qubit readout

The fragility of qubit quantum state and the recent developments of quantum error correction protocols for fault-tolerant quantum computing [82] have made the qubit read-out an essential process towards the development of the first commercial quantum computer [83]. However, the construction of an apparatus to measure the quantum state of a superconducting qubit is intrinsically difficult. To access the quantum state, in fact, we must physically couple the qubit to some

kind of measurement apparatus, which introduces undesirable leakage channels and can destroy the fragile qubit's state. In order to make a good measurement, the system must accurately distinguish a quantum state on demand without affecting its coherence. Here are the criteria required for a successful superconducting qubit measurement system.

- **Fidelity:** Existing theoretical protocols to ensure quantum fault tolerance requires that a qubit state can be measured with an accuracy of at least 90% if all other parts of the computer, such as logic gates, function flawlessly. However, in a real system with imperfect gates, current protocols require an accuracy of 99%. Therefore, we need to be able to distinguish the two computational states with a level of accuracy of 99%. Additionally, the requirement for high accuracy also means that the measurement time must be a small fraction of the qubit's lifespan so that the qubit does not change state during measurement.
- **Fast repetition:** In order to be useful in cyclic fault tolerance protocols like the surface code, any reset time in the measurement apparatus must be short compared to the qubit lifetime.
- **Coherence:** The measurement apparatus itself must not destroy the quantum coherence of the qubit states during the coherent part of the computer's operation. The process of measuring a quantum state destroys its coherence by construction, so it is essential that the measurement process can be switched off. If it cannot, then the qubit lifetime can never exceed the measurement time. Furthermore, the measurement system must not inject noise into the qubits or load them with too much damping.
- **Non-demolition:** For the purpose of fault tolerance, when measuring a qubit we want to know which state it was in when the measurement was first turned on. Once we have that information, the qubit does not actually have to be in that same state at the end of the measurement. As long as we know which state the qubit was in at the end of the measurement, we can put it into whatever other state we wish with control pulses. A measurement process in which there is a one-to-one correspondence between the measurement output and the final state of the measured system is said to be "non-demolitive". A measurement system without this property leaves the qubit in an unknown state after measurement, in which case the qubit cannot be reliably reused.
- **Multiplexing:** In order for a qubit measurement system to be usable in a quantum processor, it must work not only for single qubits but for large qubit systems. This requirement means that the measurement apparatus should be comparable to or smaller than the qubits in size, and should not significantly increase the number of control wires needed to operate the processor.

2.2 Dispersive Measurement

Several ways to perform the read-out of superconducting qubits have been validated in the literature. Most of these techniques exploit the peculiar functioning of each superconducting qubit [84–88] and thus are specific to the particular kind of superconducting qubit under test. For example, in a charge qubit the measured physical quantity is the electric charge on the superconducting island that can be detected by a single electron transistor (SET) [84, 85]. For a flux qubit, the two basic states of the qubit are defined by persistent currents circulating in the clockwise and counter-clockwise directions, which can be detected by using a current detector, for example, a DC SQUID [86]. In the case of a phase-qubit, its states are measured using the tunnelling out of the zero-voltage state of a current-biased Josephson junction [88].

A more general approach, that can be adapted to readout any kind of superconducting qubit, takes its origin from Circuit Quantum Electrodynamics (cQED) and it involves the interaction between artificial superconducting atoms and a classical microwave field in superconducting cavities [54].

When the resonator and the superconducting atom interact together under certain conditions, photons in the cavity are “dispersed” in a way that depends on the qubit state. Therefore this method provides information on the state of the superconducting atom without interacting directly with it. This technique allows quantum non-demolition (QND) measurements of the qubit state, which implies that subsequent measurements of the same variable will give the same result as the first measurement [54].

Mathematically, the interaction between a superconducting qubit and cavity can be described in the framework of the Jaymes-Cummings model [83, 89]:

$$\begin{aligned}\hat{H} &= \hat{H}_r + \hat{H}_q + \hat{H}_{int} \\ \hat{H} &= \hbar\omega_r \left(\hat{a}^\dagger \hat{a} + \frac{1}{2} \right) + \frac{\hbar\omega_q}{2} \hat{\sigma}_z + \hbar g \left(\hat{\sigma}_+ \hat{a} + \hat{\sigma}_- \hat{a}^\dagger \right).\end{aligned}\tag{2.1}$$

Here, H_r is the standard harmonic oscillator Hamiltonian with frequency $\omega_r/2\pi$, containing lowering and raising operators \hat{a} and \hat{a}^\dagger associated with the superconducting cavity. In the context of an electrical resonator, in fact, with inductance L_r and capacitance C_r , we can define \hat{a} and \hat{a}^\dagger as:

$$\begin{aligned}\hat{a}^\dagger &= \frac{(L_r C_r)^{1/4}}{\sqrt{2\hbar}} \left(\frac{\hat{\varphi}_r}{L_r} + i \frac{\hat{Q}_r}{C_r} \right) \\ \hat{a} &= \frac{(L_r C_r)^{1/4}}{\sqrt{2\hbar}} \left(\frac{\hat{\varphi}_r}{L_r} - i \frac{\hat{Q}_r}{C_r} \right)\end{aligned}\tag{2.2}$$

where $\hat{\varphi}$ and \hat{Q} are the quantized operators associated with the normalized magnetic flux and charge introduced in Eqs. 1.10 and 1.11.

In an analogous way, \hat{H}_q is the hamiltonian of the two-level qubit system, with the Pauli operators $\hat{\sigma}_z$, $\hat{\sigma}_+$ and $\hat{\sigma}_-$ and frequency $\omega_q/2\pi$. The term H_{int} describes

the electrical-dipole interaction between a qubit and a resonator field with coupling strength g , consisting of a single swap photon per time.

The James Cumming model is valid under the following assumptions:

- Qubit is a perfect two-level system, which means, the probability of incurring transitions other than the one from the ground state to the excited state and vice versa is negligible
- *Rotating Wave Approximation (RWA)*: The interactions that don't preserve the number of photons, and thus the energy of the system, are negligible. This approximation is valid under the assumption:

$$g, |\omega_r - \omega_q| \ll |\omega_r + \omega_q| \quad (2.3)$$

- The resonator is a single-mode resonator, which means that only the fundamental one is relevant in the system dynamics

Depending on the ratio between the coupling strength g , and the detuning between the resonator and qubit frequencies $\Delta = \omega_q - \omega_r$ several regimes can be observed. The most interesting for the readout superconducting qubits is the *Dispersive regime* occurring when $|g/\Delta| \ll 1$. In this case, the effect of the interaction term is to shift the resonances ω_r and ω_q by an amount dependent on the number of excitations. This can be seen by applying the Schrieffer-Wolff [40, 89–91] transformation to Eq. 2.1 up to the second order of perturbation in g , which gives:

$$\hat{H} = \hbar \left(\omega_r + \chi \hat{\sigma}_z \right) \hat{a}^\dagger \hat{a} + \frac{1}{2} \left(\omega_q + \chi \right) \hat{\sigma}_z \quad (2.4)$$

where we have introduced

$$\chi = \frac{g^2}{\Delta}. \quad (2.5)$$

The last relation can be opportunely modified to include the effects that higher energy levels have in the resonator-qubit dynamics [40, 89]:

$$\chi \rightarrow \chi_{01} - \frac{1}{2} \chi_{12} = \frac{\chi}{1 - \Delta/\alpha} \quad (2.6)$$

where $\alpha = \omega_{12} - \omega_{01}$ is the anharmonicity.

Equation 2.4 shows that the resonator field experiences a frequency shift of magnitude χ depending on the qubit state. This shift can be exploited to perform a QND measurement of superconducting qubits by probing the transmission of the resonator.

2.3 Heterodyne detection

The dispersive regime reveals a method for indirectly measuring the qubit state by measuring the χ -shift imparted on the resonator. This is done typically in

2.3. HETERODYNE DETECTION

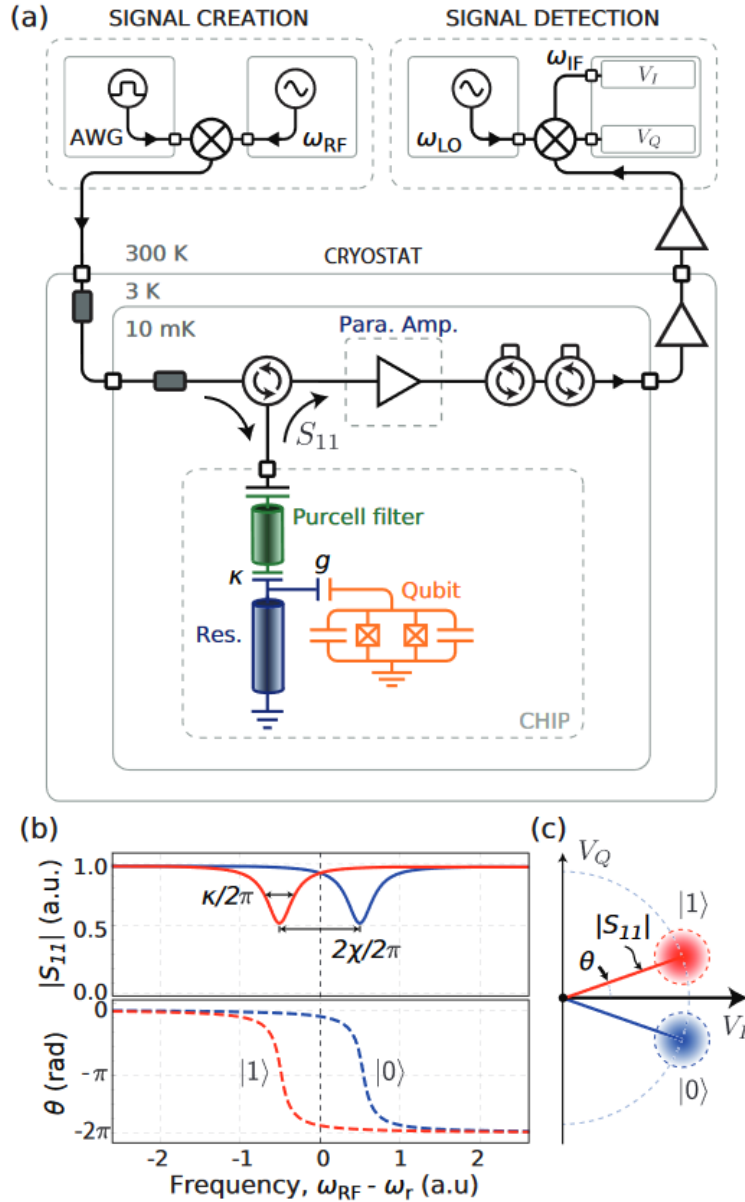


Figure 2.1: Adapted from Ref.[69]: Simplified schematic of a representative experimental setup used for dispersive qubit readout. The resonator probe tone is generated, shaped and timed using an arbitrary waveform generator (AWG), and sent down into the cryostat. The reflected signal S_{11} is amplified, first by a parametric amplifier and then by a low-noise HEMT amplifier, before it is downconverted using heterodyne mixing and finally sampled in a digitizer. (b) Reflected magnitude $|S_{11}|$ and phase θ response of the resonator with linewidth k , when the qubit is in its ground state $|0\rangle$ (blue) and excited state $|1\rangle$ (red), separated with a frequency $2\chi/2\pi$. (c) Corresponding complex plane representation, where each point is composed of the in-plane $Re[S_{11}]$ and quadrature $Im[S_{11}]$ components. The highest state discrimination is obtained when probing the resonator just in between the two resonances, (dashed line in (b)), thus maximizing the distance between the states.

the framework of the heterodyne detection scheme, as shown in Fig 2.1.

This technique consists in sending as an input to the resonator a signal $s_{in}(t)$ with a certain amplitude $a_{in}(t)$ and frequency ω_s and evaluating the change in amplitude and phase of the output signal $s_{out}(t)$ that depends on the qubit state, as shown in Fig. 2.2. More precisely, given an input tone sent through the superconducting cavity:

$$s_{in} = a_{in}(t)\cos(\omega_s t) \quad (2.7)$$

the information on the qubit state is stored in the amplitude a_{out} and phase θ of the output signal:

$$s_{out} = a_{out}(t)\cos(\omega_s t + \theta) \quad (2.8)$$

Typical superconducting resonators operate in a range of frequencies between 4 GHz and 8 GHz. However, it is difficult to generate high-fidelity pulses within this range of values. Instruments capable of directly producing shaped pulses at frequencies of gigahertz exist, but they are prohibitively expensive. To overcome this limitation, “IQ mixing” is generally employed. This process involves mixing two signals that are at different frequencies; typically one signal is at a fixed frequency (the local oscillator or LO) and the other is at a varying frequency (the radio frequency or RF). The mixing process creates new tones that are the sum and difference of the original frequencies. IQ mixing is performed by a mixer, which is essentially a 4 port device. This device requires two signals with the same intermediate frequency and $+90^\circ$ of dephasing [69]:

$$\begin{aligned} I(t) &= a(t)\cos(\omega_{RF}t + \theta) \\ Q(t) &= -a(t)\sin(\omega_{RF}t + \theta) \end{aligned} \quad (2.9)$$

and a “local oscillator” or “carrier signal”:

$$L(t) = \cos(\omega_{LO}t). \quad (2.10)$$

The $I(t)$ and $Q(t)$ signals are called respectively the “In phase” and “Quadrature” components of a signal with ω_{RF} frequency, and represent its real and imaginary part in the complex plane.

From these three inputs, the IQ mixer can perform the operation:

$$\begin{aligned} s(t) &= a(t)\cos(\omega_{RF}t)\cos(\omega_{LO}t) - a(t)\sin(\omega_{RF}t)\sin(\omega_{LO}t) = \\ &= a(t)\cos[(\omega_{LO} + \omega_{RF})t] + a(t)\cos[(\omega_{LO} - \omega_{RF})t]. \end{aligned} \quad (2.11)$$

As a practical example for superconducting qubit readout, one can produce specific pulse sequences in the GHz regime by mixing together a GHz tone generated by a LO and the same sequence reproduced in the MHz regime by an AWG. The mixed signal is then delivered to the chip inside the fridge and probes the state of the cavity.

For the same reason, the output signal coming out of the cryostat must be down-converted to make it readable for standard electronic devices. Using the same logic it’s possible to perform this step using another IQ mixer and the same LO reference. Mathematically, let’s consider a high-frequency signal:

$$s(t) = a(t)\cos[(\omega_{LO} + \omega_{RF})t + \theta] \quad (2.12)$$

2.3. HETERODYNE DETECTION

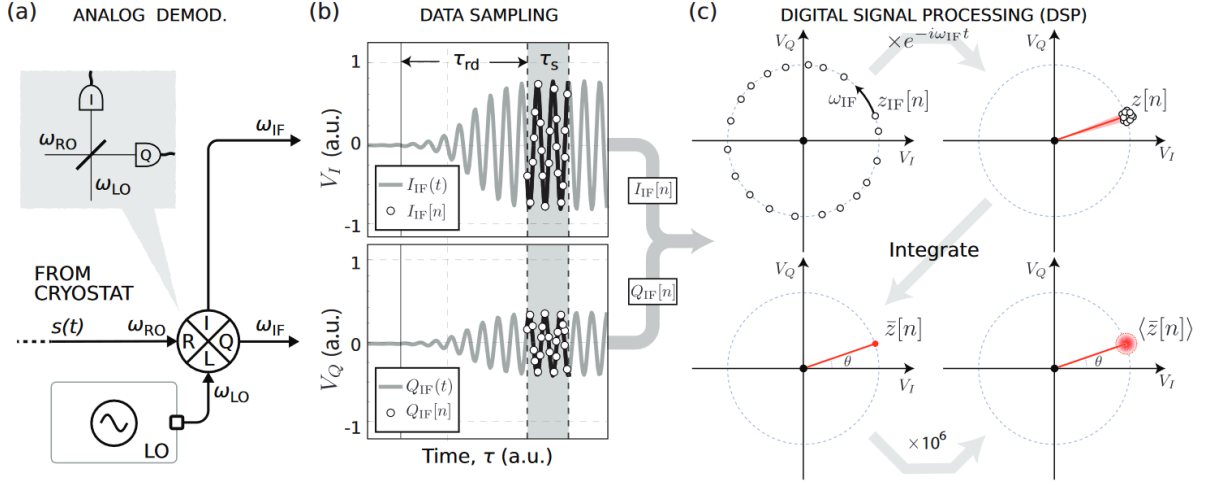


Figure 2.2: Adapted from Ref. [69]: Schematic of the heterodyne detection technique. (a) The signal with frequency ω_{RF} from the cryostat is mixed with a carrier tone with frequency ω_{LO} , yielding two quadratures at a down-converted intermediate frequency $\omega_{IF} = |\omega_{RO} - \omega_{LO}|$, and 90° out-of-phase with each other. (b) The two signals are passed into two different analog-to-digital converters (ADC) channels. To avoid sampling the resonator transient, some readout delay (τ_{rd}) corresponding to the resonator linewidth may be added, and the two signals are sampled for a time τ_s . In this case, the white dots represent the sampled points. (c) The sampled traces are post-processed and after some algebra, the sampled data points are averaged into a single point in the (I, Q)-plane. To extract statistics of the readout performance, i.e. single-shot readout fidelity, a large number of (I, Q)-records are acquired, yielding a 2D-histogram, with a Gaussian distributed spread given by the noise acting on the signal.

which is fed into the RF port of an IQ mixer together with a tone at ω_{LO} in the local oscillator (LO) port. The mixing process, followed by low pass filtering, produces at port I:

$$\begin{aligned}
 I(t) &= a(t) \cos[(\omega_{LO} + \omega_{RF})t + \theta] \cos(\omega_{LO}t) = \\
 &= \frac{a}{2} \cos[(2\omega_{LO} + \omega_{RF})t + \theta] + \frac{a}{2} \cos[\omega_{RF}t + \theta] \\
 &\xrightarrow{\text{low pass filter}} \frac{a(t)}{2} \cos[\omega_{RF}t + \theta]
 \end{aligned} \tag{2.13}$$

In a similar way, at port Q we obtain:

$$\begin{aligned}
 Q(t) &= a(t) \cos[(\omega_{LO} + \omega_{RF})t + \theta] \sin(\omega_{LO}t) = \\
 &= \frac{a}{2} \sin[(2\omega_{LO} + \omega_{RF})t + \theta] + \frac{a}{2} \cos[(\omega_{RF})t + \theta] \\
 &\xrightarrow{\text{low pass filter}} \frac{a(t)}{2} \sin[\omega_{RF}t + \theta]
 \end{aligned} \tag{2.14}$$

It's clear that, since ω_{RF} is typically in the range of MHz , this technique brings the $s(t)$ to be readable in the range of available analog-to-digital converters

(ADCs), that typically have 500 MSa/s sampling rate.

The resulting digital signals are now written as $I_{digital}[n]$ and $Q_{digital}[n]$:

$$\begin{aligned} I_{digital}[n] &= \sum_n \frac{a}{2} \cos(\omega_{RF} n\Delta t + \theta) \\ Q_{digital}[n] &= \sum_n \frac{a}{2} \sin(\omega_{RF} n\Delta t + \theta) \end{aligned} \quad (2.15)$$

where Δt is the sampling period (typically around 2 ns considering an ADC with 500 MSa/s of sampling rate) and n indexes the sample number of the continuous-time signals $I(t)$ and $Q(t)$.

Typically, during the digitalization one acquires a delayed window of samples $[n1 : n2]$ to avoid the first few samples that may decrease the overall signal-to-noise ratio. From the digitalized raw trace, it's possible to extract information on the $a(t)$ and θ by multiplying the series of points in Eq. 2.15 by $\cos(\omega_{RF})$ and $\sin(\omega_{RF})$ and averaging in time the results. In this way it is possible to obtain the quantities of our interest:

$$\begin{aligned} I_{digital}[n] &= \frac{a}{2} \cos(\theta) \\ Q_{digital}[n] &= \frac{a}{2} \sin(\theta) \end{aligned} \quad (2.16)$$

which carry the information on the qubit state.

2.3.1 Scalability in heterodyne detection technique

The practical implementation of the heterodyne technique to detect the qubit state requires many other physical elements between the room-temperature mixers and the read-out resonator. The room temperature signal must be attenuated by many orders of magnitude in order to bring the signal to the single photon limit. Attenuators are also used to reduce the thermal noise generated at the different temperature stages inside the cryostat [69, 92], which are at temperatures higher than $T_{sample} = 10 mK$. On the contrary, while the input signal must be reduced to preserve the coherence of the quantum chip, the readout signal needs a significant amount of amplification to be delivered to room temperature. Typically, a High Electron Mobility Transistor amplifier (HEMT) is used as the main cryogenic amplifier. These devices are active elements that generate thermal noise. In the specific case of the commercial HEMT, the noise characteristic temperature T_n is 1.5K. For this reason, the device is placed at the 4 K stage, which is the first plate at a temperature higher than T_n [69]. Several isolators or circulators are required between the sample and the amplifier to protect the quantum circuit from the generated noise. These components are non-reciprocal elements based on magnetic materials which provide directionality and prevent noise transmission [9, 10, 93]. These elements typically have a magnetic core in ferrite, which can generate unwanted effects in superconducting elements, and necessitate being opportunely shielded. For this reason, isolators and circulators

are bulky in size and difficult to be thermalized, which makes their use expensive and not easily scalable [9, 10, 93].

In the context of the surface code, error detection demands fast, high-fidelity measurement of multiqubit parity operators [5, 10]. Single-shot readout fidelity in the dispersive regime is not achievable with only a HEMT amplifier and an additional quantum-limited amplifier is needed. This device adds ideally only noise at the quantum limit (a half photon) while providing modest gain (usually 10-15 dB) [93].

A variety of ultralow-noise Josephson amplifiers have been exploited to achieve high-fidelity measurement of superconducting qubits [94–97]; however the small bandwidth or the requirement of a strong pump tone of some sort limits this approach to the quantum processor with a small number of elements.

A possible solution to these obstacles involves the use of a Josephson Photon Multiplier (JPM) proposed in the works [9, 10, 79, 80, 93, 98].

2.4 The Josephson Photon Multiplier (JPM)

The JPM is essentially a single Josephson junction in an rf superconducting quantum interference device (SQUID) loop, biased close to the critical flux where a phase slip occurs [79, 80]. The Hamiltonian of the device is similar to the phase qubit one and is given by:

$$\hat{H}(\hat{Q}, \hat{\varphi}) = \frac{\hat{Q}^2}{2C_s} + \frac{1}{2L_s} \left(\frac{\Phi_0}{2\pi} \right)^2 \left(\varphi - \frac{2\pi\Phi_{ext}}{\Phi_0} \right)^2 \quad (2.17)$$

where C_s and L_s are the shunting capacitor and inductor respectively of the JPM and φ is the phase across the junction.

An important parameter is β_L defined as $\beta_L = L_s/L_J$. β_L is simply a ratio of inductances that determine whether the potential is mostly a parabola (arising if the linear shunt inductor dominates) or a cosine (arising from the nonlinear Josephson junction). Since the JPM is intended to be a single-bit detection circuit (0 or 1), the circuit parameters are chosen to yield a potential energy landscape with one or two local minima, depending on the applied flux bias Φ_{ext} .

The protocol for performing qubit measurement with the JPM is shown in Fig. 2.3 [93]. The JPM is initially tuned to its maximum frequency, in order to decouple it from the other components on chip. This configuration corresponds to a single deep well which resets the system wavefunction to its potential minimum. As plotted in the panel “deplete” of Fig. 2.3, the JPM is successively tuned to a frequency on resonance with the capture cavity. This depletes any photons left over in the cavity from the last experiment by coupling the photons through the lossy dielectric of the JPM shunt capacitor. When it is time to measure the qubit (“capture” panel in Fig. 2.3), the pointer-states are prepared and the JPM is tuned to be in resonance with the dressed cavity and the readout resonator.

The readout resonator is driven with a tone at $\omega_{|1\rangle}$, corresponding to the resonance frequency of the resonator when the qubit is in the state $|1\rangle$. In this case,

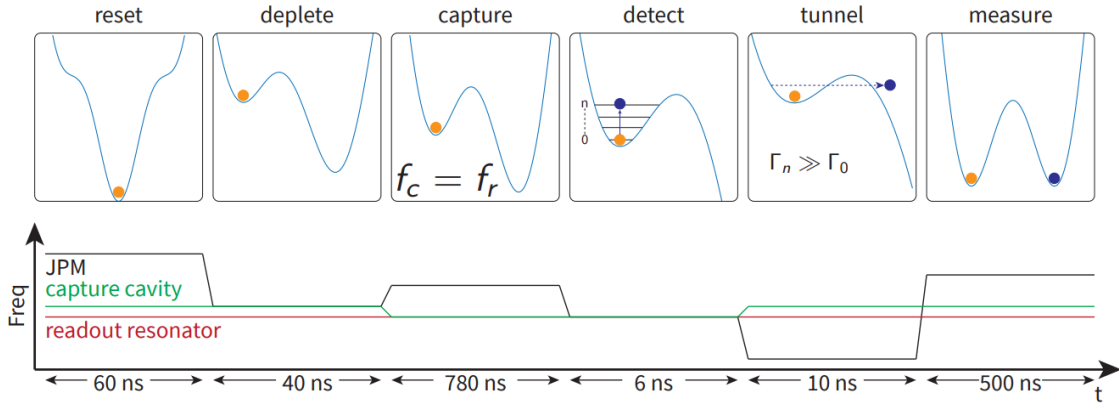


Figure 2.3: JPM protocol from [93]: (a - reset) JPM is reset into a single well configuration, which is maximally detuned from the rest of the system. (b - deplete) The JPM potential energy is adequately tilted in order to trap the phase particle in the metastable minima. Simultaneously the JPM is tuned on resonance with the capture cavity to deplete any photons left over from the last detection. (c - capture) The capture cavity is tuned on resonance with the readout resonator, as the pointer states are prepared. (d - detect). JPM is tuned on resonance with the capture cavity. If the qubit is in the excited state, the photons entering the cavity induce excitations to higher states in the initial well. (e - tunnel) JPM is then tuned to a shallow bias point so that higher energy states tunnel into the adjacent well. (f - measure) Finally, the JPM is brought to a point where the two wells are maximally separated in frequency, allowing for microwave detection

if the qubit is in the state $|1\rangle$, a lot of photons populate the cavity and can be absorbed by the JPM. These photons can promote excitations to higher energy levels, leading to a large probability of tunnelling in the right well. Instead, if the qubits are in the state $|0\rangle$, the wavefunction remains bounded in the minimum of the left well, since no photons fill the resonator. The transition probability to the right well is further increased in the “tunnel” step when the JPM is then tuned to a shallow bias point.

Finally, the detection is completed with JPM measurement. The authors in Refs. [79, 80, 93] performed the JPM readout using the same heterodyne technique described in the previous Section, to simply validate the proposed detection technique. However, one can distinguish the two JPM states by measuring the current’s sign that flows in the detector as in a standard phase qubit [99]. This constitutes one of the main advantages of the JPM technique: the quantum information is digitalized at the mK stage of a cryogenic fridge and it’s directly available without any further operation, contrary to the case of the heterodyne detection where demodulation is required. Furthermore, as proposed in Refs. [9, 10], the classical bit of information stored in the JPM can be processed by a proximal SFQ co-processor located inside the fridge. This approach permits the reduction of the latency associated with the signal delivery, and at the same time, it brings benefits to the system scale-down.

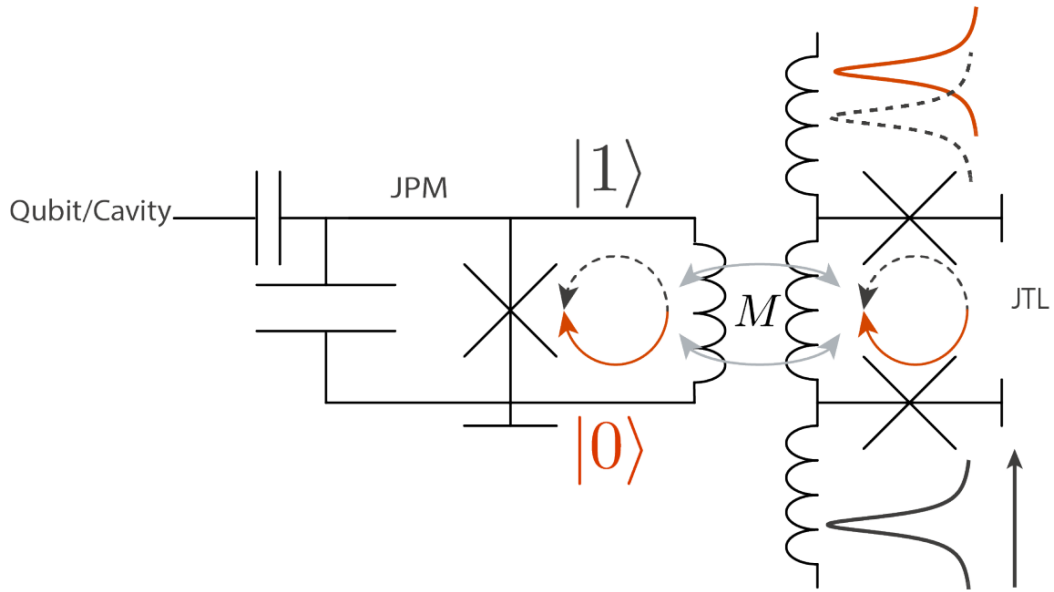


Figure 2.4: Adapted from Ref. [81]: JPM coupled to ballistic JTL. The opposing arrows in the rf-SQUID loop represent the two circulating current states of the JPM. The ballistic JTL is shown on the right-hand side and one cell is coupled to the JPM inductor through a mutual M . Fluxons travelling through the JTL are forward or reverse-biased and pick up a conditional time delay based on the state of the JPM

2.4.1 SFQ architectures to detect the JPM state

In the direction of performing the JPM readout with an SFQ architecture, the authors in Refs. [81, 93] proposed two different approaches. The first involves propagating fluxons as a direct probe of the JPM state. This technique was first investigated theoretically in Ref. [100] where a ballistic Josephson Transmission Line (JTL) is coupled directly to a superconducting flux qubit, whose states correspond to different circulating currents [101]. The flux from the qubit induced a small current in the ballistic JTL, effectively forward or reverse biasing the fluxon as it travelled through the line. This maps the state of the qubit onto the time delay of the fluxon.

A full circuit for this approach was proposed in Ref. [102] and improved in Ref. [103], including additional components to detect the induced delay. Recently, this method for measuring flux qubits has been investigated in Refs. [104–107]. In addition to these theoretical studies of JTL-based flux qubit readout, an experimental implementation of flux qubit readout using travelling fluxons in an annular Josephson junction was demonstrated in Ref. [108].

The approach discussed above can be adopted to detect the circulating current states in the JPM [81, 93]. The circulating current being detected in the JPM is one or two orders larger than in typical applications with flux qubits since the JPM measurement is purely classical and does not need to be QND [93]. Furthermore, the authors in Refs. [81, 93] estimate a negligible backaction due

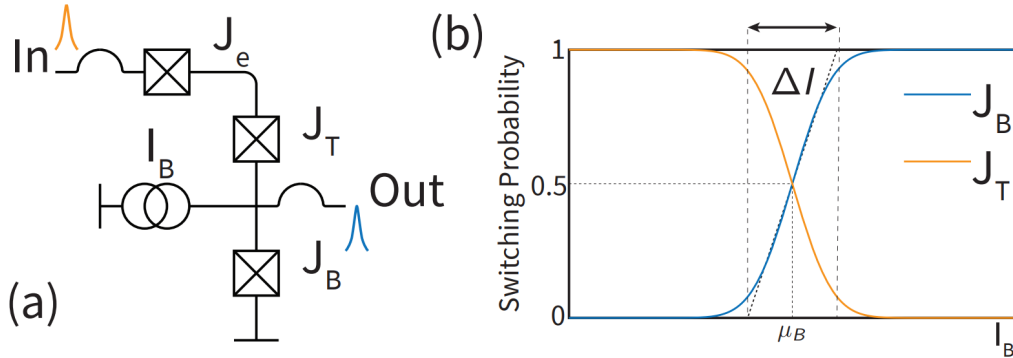


Figure 2.5: SFQ Comparator in Ref. [93]: (a) The comparator consists of two junctions with equal critical current, J_T and J_B in series. The current being compared I_B is injected in between the two junctions. When an SFQ pulse arrives at J_T , the sign of I_B determines which of the two junctions is closer to its critical current. If J_B switches, an SFQ pulse is sent out of the comparator. If J_T switches, the output is held low, and the escape junction J_e switches in tandem to cancel out the voltage and prevent a pulse from being emitted backaction (b) Switching probabilities for both comparator junctions as a function of I_b . ΔI is the grey zone of the comparator

to dissipation or noise generated in the SFQ circuitry, because the JPM readout is performed when it's not in resonance with the qubit cavity system.

The second approach proposed in Ref. [81] involves an SFQ comparator. The use of this circuitry to measure phase and flux qubits was proposed in the early 2000s [109] and has been investigated further over the next 5 years [110–112].

The comparator is a standard SFQ circuit element used mainly in SFQ analog-to-digital converters [112–114]. It consists of two identical junctions that operate as a decision-making pair [81]. Both junctions are biased close to their critical currents, and the signal to be compared I_B is injected between them. As shown in Fig. 2.5 when an SFQ pulse arrives at J_T , the sign of I_B determines which of the two junctions is closer to its critical current. If J_B switches, an SFQ pulse is produced at the out of the comparator; otherwise, if J_T switches, the output is held low and the SFQ pulse is shorted to ground through the bottom junction. J_e switches in tandem to J_T to prevent backaction into the previous circuitry. In the JPM approach, I_b is the current originating from the flux transformation of the circulating current in the detector.

This technique provides the same advantages as the one discussed above, which exploits propagating fluxons in a JTTL, with a simpler circuitry for the SFQ part [114].

JPM detection is a very powerful and attractive technique. Within this approach, it's possible to achieve raw single-shot measurement high fidelity in excess of 98% in total measurement times under 500 ns [79, 80], already compares favourably with the current state of the art [6]. The JPM provides access to the binary result of projective quantum measurement at the millikelvin stage of a

dilution refrigerator; furthermore, it eliminates the need for nonreciprocal circuit components between the qubit and the measurement apparatus [79, 80]. This detector can work together with a current or flux detector, such as SFQ comparators, to reduce the physical overhead associated with the superconducting qubit readout while allowing, in principle, low-latency operations conditioned on the qubit state.

However, the JPM approach has some drawback which limits its applicability in large-scale systems. First of all, the JPM is required to be in resonance with the cavity in order to be promoted in the right well when the qubit is state $|1\rangle$. This requests a precise fine-tuning of the device to maximize the probability to observe energy level transitions. Furthermore, being in resonance with the qubit, the JPM dynamics could produce backaction, interfering with the fragile coherence of the quantum chip. This happens especially when the JPM wavefunction tunnels in the right well, when an estimated energy of 100 photons is produced with a wide range of spectral components also at the frequencies of the readout resonator and the qubit [79, 80]. The measurement sequence involves some steps to deplete the resonator from photons generated in the previous measurements. The main effect is a larger complexity, which brings, consequently, an increase in measurement time duration.

The JPM physical footprint is comparable to the dimensions of the qubit [79, 80] so that it would be straightforward to integrate a single JPM element with every qubit in a large-scale multiqubit processor. However, even if the JPM requires only one additional flux bias line to be controlled, the final physical footprint could be larger considering the additional devices or lines needed for the JPM readout.

A new readout technique, proposed in this work and based on a flux-switchable superconducting circuit, is capable of discriminating between two phase values of a coherent input tone at GHz frequency and is able to circumvent most of the problems outlined above. For instance, such tone can be a readout pulse whose phase encodes the outcome of a qubit measurement. We name our device Josephson Digital Phase Detector (JDPD), as the result of the detection is naturally digitalized in the occupation of a phase particle in either the two wells, in the same fashion as the JPM, when the JDPD's potential is opportunely configured. The device operation is compatible with SFQ circuits, which could be employed to perform the detection in a full-digital fashion, thus bringing benefits to the system scalability as discussed above. As demonstrated in the next Sections, the JDPD is not required to be in resonance with the GHz tone that we want to digitalize. Contrary to the JPM, the phase particle dynamics will not affect the qubit state and thus, no intricate preparations of the detector are required. The JDPD's physical footprint is similar to the JPM; however, we estimate a single JDPD can be exploited to measure multiple qubits with a single bus connection, which is relevant for the multiplexing of a superconducting quantum processor.

Chapter 3

The Josephson Digital Phase detection (JDPD)

The JDPD is composed of a nominally symmetric Quantum Flux Parametron [115] which is an SFQ superconducting device [116, 117]. The QFP can switch between different states with a speed up to 100 GHz and a nW-order dissipation. Thanks to these characteristics, this device has been considered for a wide range of possible applications [118].

Originally, the QFP has been proposed as a possible candidate for the components of ultra-high speed computers based on Josephson junctions [119–123]. With the advent of the superconducting quantum circuits era [1], a device with similar characteristics to the QFP, named double SQUID, has been studied as a tunable superconducting flux qubit [124–127]. By controlling its energy potential with a nanosecond-long (non-adiabatic) pulse of magnetic flux, the double SQUID can enable quantum gates to be generated in less than 100 ps, a timescale faster than that of existing superconducting qubits [124–127]. The gate operations can be efficiently performed by using classical logic signals to control the qubit, which is advantageous for the large-scale implementation of quantum circuits. The double SQUID also shows immunity to both thermal and magnetic field fluctuations having the possibility to be controlled with two independent magnetic fluxes [124–127].

In 1991, the QFP has been proposed as a signal discriminator between two different signals [128–130] with possible applications to qubit readout [131]. As shown in Fig. 3.1, this technique consists in comparing a tone at frequency ω to a reference signal at a certain frequency ω_x . When the two frequencies are equal, i.e $\omega = \omega_x$, the output from the Adiabatic-QFP (AQFP) gate is 1 for every clock cycle. When $\omega \neq \omega_x$, the output signal manifests both “1” and “0” as shown in Fig. 3.1. Thus, the AQFP acts as a narrow linewidth amplifier [131]. By averaging the output signals from the AQFP with an analog or digital integrator, its sensitivity is expected to be considerably improved. In the work of Ref. [129] the AQFP gate has a sensitivity of a few μA in the GHz operation frequency range at 4.2 K but it’s expected to be enhanced at lower temperatures [131].

The low power consumption of this device makes possible the integration in the

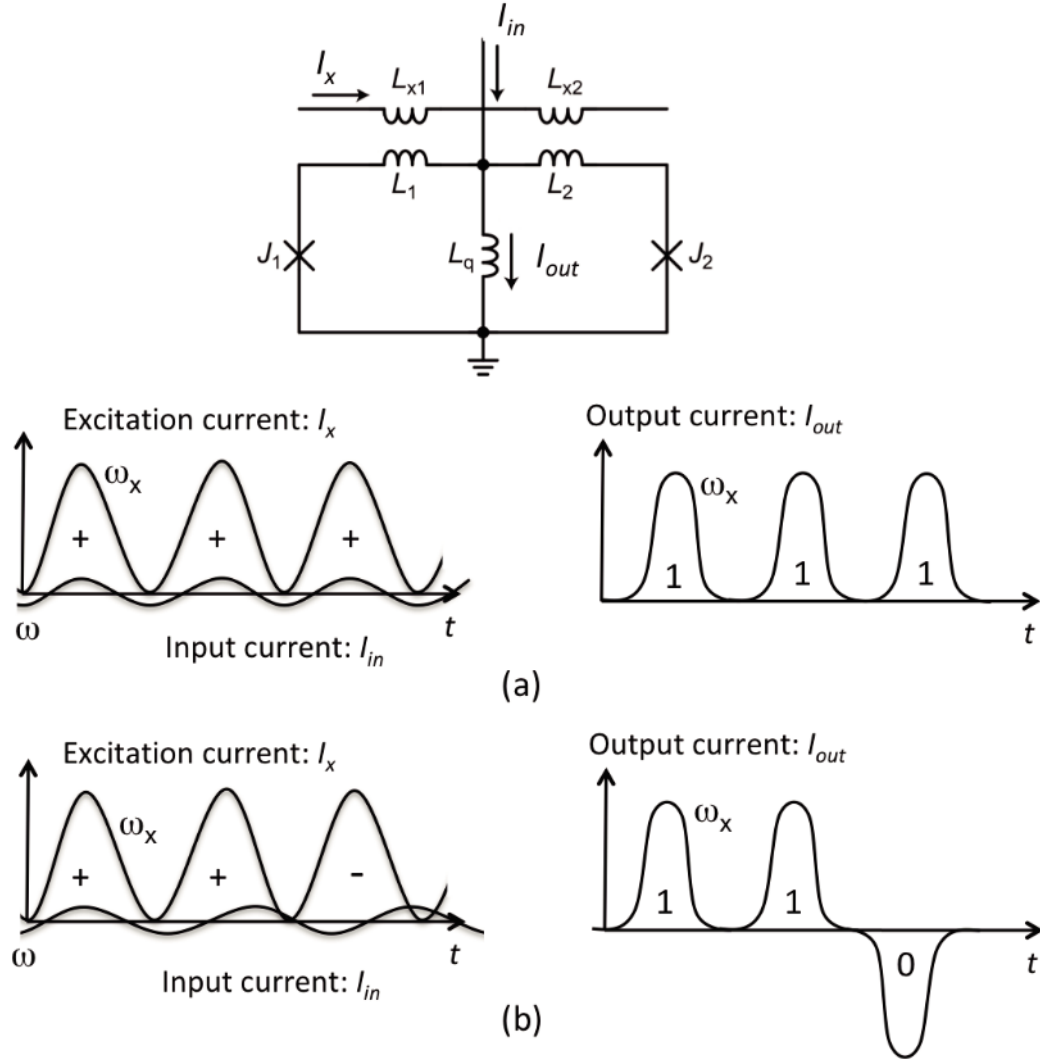


Figure 3.1: Adapted from Ref. [131]: conceptual diagram of highly sensitive adiabatic-QFP (AQFP) microwave detector. I_{in} is a small signal from a qubit with a frequency of ω while I_x is an excitation current with a frequency of ω_x applied to the AQFP gate. (a) When $\omega = \omega_x$, the output from the AQFP gate becomes “1” for every clock cycle. (b) When $\omega \neq \omega_x$, the output signal exhibits both “1” and “0”.

same qubit’s temperature stage, ensuring the necessary scalability of the quantum computing system [132–134]. However, as a drawback, the QFP is operated adiabatically and requires multiple signal periods to produce a reliable bit stream sequence limiting the readout speed.

In this Chapter, an innovative approach to signal detection based on flux-biased QFP, the Josephson Digital Phase Detector (JDPD), will be presented. The protocol exploits the possibility for the JDPD to change from a harmonic to a double-well potential configuration by applying diabatic magnetic fluxes, which can be generated by a co-located SFQ circuit. Therefore, this approach allows

fast single-shot measurements to overcome the limitations of the previous detection technique based on QFP.

3.1 Device model

The fundamental block of the JDPD is shown in Fig. 3.2 A. The JDPD is based on two rf-SQUIDS with critical currents I_{c1} and I_{c2} that share an inductive load L in the centre node. The Junctions are connected to L through the inductances L_1 and L_2 . The presence of two loops makes this device tunable with two independent fluxes ϕ_1 and ϕ_2 :

$$\phi_{1,2} = 2\pi \frac{\Phi_{1,2}}{\Phi_0} \quad (3.1)$$

that can be provided by two different lines mutually coupled to L_1 and L_2 . To describe the system evolution, it's fundamental to define the phase drops across the junctions, i.e $\varphi_{1,2}$, and across the central inductor L , φ . Under the assumption $L_{1,2} < L_J$, i.e the phases drop across the inductors $L_{1,2}$ are negligible, φ and $\varphi_{1,2}$ are linked by the equations:

$$\varphi_{1,2} = \varphi \pm \phi_{1,2}. \quad (3.2)$$

Thus, the potential energy can be written as:

$$U(\varphi, \phi_1, \phi_2) = \left(\frac{\Phi_0}{2\pi}\right)^2 \frac{\varphi^2}{2L} - \frac{I_{c1}\Phi_0}{2\pi} \cos(\varphi + \phi_1) - \frac{I_{c2}\Phi_0}{2\pi} \cos(-\varphi + \phi_2) = E_L \left[\frac{\varphi^2}{2} - \beta_1 \cos(\varphi + \phi_1) - \beta_2 \cos(-\varphi + \phi_2) \right] \quad (3.3)$$

where $\beta_{1,2} = 2\pi I_{c1,2}L/\Phi_0$ and E_L is the inductive energy from the definition in Eq.1.10. To describe the flux-tuning properties of the device in a compact form, it is useful to introduce the common and differential fluxes ϕ_+ and ϕ_- , defined as

$$\begin{aligned} \phi_+ &= \frac{\phi_1 + \phi_2}{2} = \frac{\varphi_1 - \varphi_2}{2} \\ \phi_- &= \frac{\phi_1 - \phi_2}{2} = -\varphi. \end{aligned} \quad (3.4)$$

These can be independently generated by properly designed flux lines, as explained in the Chapter ‘‘Layout’’ of this manuscript. In the symmetrical case where $I_{c1} = I_{c2} = I_c$, the potential energy function of the device is given by:

$$\frac{U(\varphi)}{E_L} = \frac{\varphi^2}{2} - 2\beta_+ \cos(\phi_+) \cos(\varphi + \phi_-) \quad (3.5)$$

where $\beta_+ = 2\pi I_c L/\Phi_0$. If $2\beta_+ \leq 1$ the potential has only one absolute minimum for any combination of ϕ_{\pm} . Instead, if $2\beta_+ > 1$, the bias fluxes can be tuned

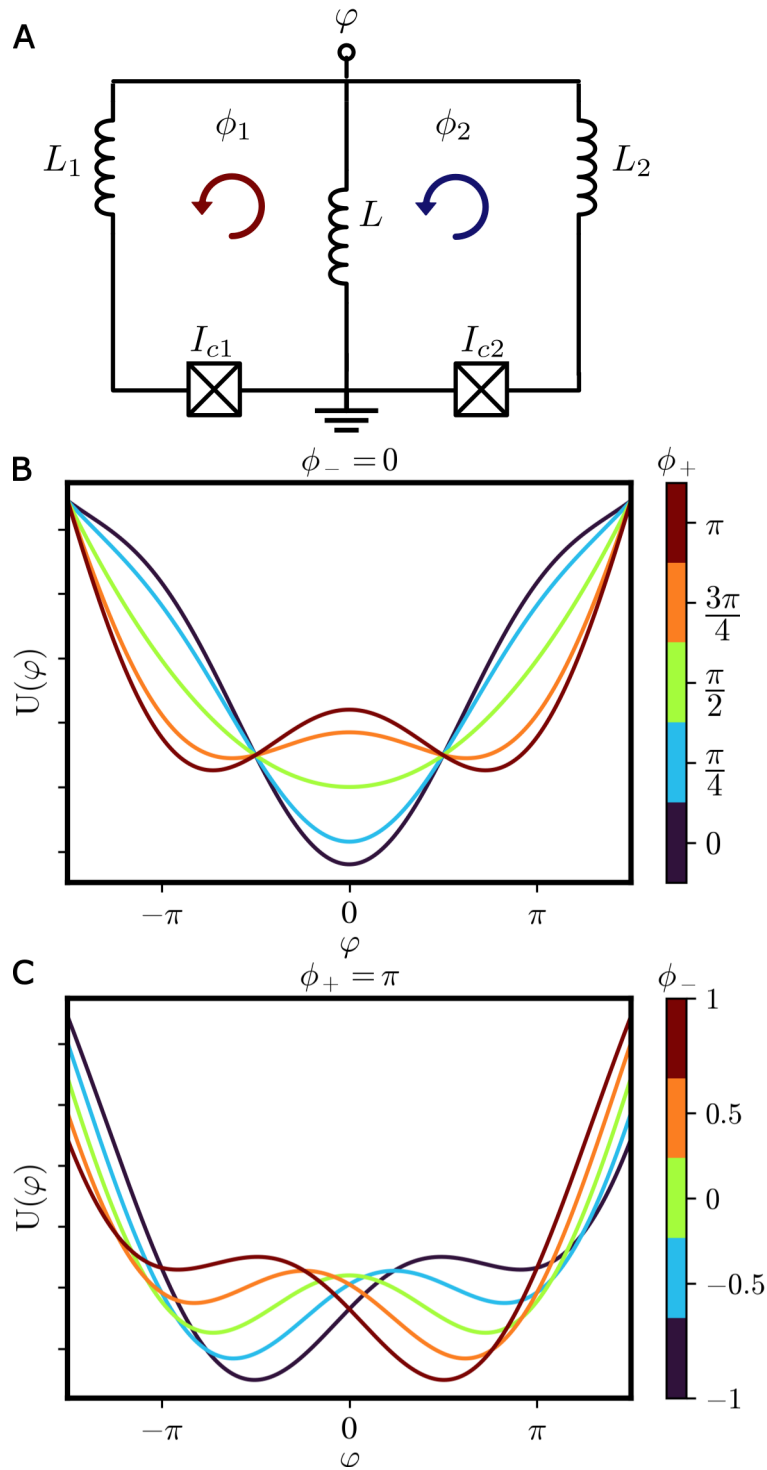


Figure 3.2: Schematic of the Josephson Digital Phase Detector (JDPD) (A). The JDPD is composed of a nominally symmetric Quantum Flux Parametron (QFP), whose left and right loops are phase-biased by independent fluxes $\phi_{1(2)}$. (B). Potential energy landscapes of the JDPD for different values of common flux $\phi_+ = (\phi_1 + \phi_2)/2$ and for $\phi_- = (\phi_1 - \phi_2)/2 = 0$. The potential energy can present one absolute minimum (blue curve), harmonic potential landscape (green curve) or two absolute minima (red curve), depending on the external magnetic flux. (C). Potential energy landscapes of the JDPD for different values of ϕ_- and $\phi_+ = \pi$. ϕ_- governs the asymmetries of the system.

to generate potential shapes with multiple minima. For instance, in Fig. 3.2 B, for a device with $2\beta_+ = 3$ and for $\phi_- = 0$, the potential energy can host a single absolute minimum for $\phi_+ = 0$ or two degenerate minima for $\phi_+ = \pi$. The device can also be flux-biased to a harmonic configuration for $\phi_+ = \pi/2$, where the nonlinear term in equation (3.5) is suppressed. The flux ϕ_- controls the asymmetries of the system and it's very useful to calibrate the detector as discussed in more detail in the next Sections. The kinetic energy is given by capacitive contributions of the Josephson junctions inside the rf loops, i.e:

$$T = \frac{C}{2} \left(\dot{\varphi}_1^2 + \dot{\varphi}_2^2 \right) = \frac{C}{2} \left[(\dot{\varphi} + \dot{\phi}_1)^2 + (-\dot{\varphi} + \dot{\phi}_2)^2 \right] = C \left[(\dot{\varphi} - \dot{\phi}_-)^2 \right] + C\dot{\phi}_+ \quad (3.6)$$

where $C_1 = C_2 = C$ is assumed for both junction capacitances. From the Lagrangian:

$$\mathcal{L} = T - U \quad (3.7)$$

it's possible to define the momenta conjugate to the node flux φ , using the relation [41, 42]:

$$q = \frac{\partial \mathcal{L}}{\partial \dot{\varphi}} = 2C(\dot{\varphi} - \dot{\phi}_-). \quad (3.8)$$

The Hamiltonian can now be expressed as the sum of the kinetic energy, which is to be expressed in terms of the $q = 2en$ variable, and the potential energy expressed, as before, in terms of φ :

$$H = 2E_c n^2 + E_L \left[\frac{\varphi^2}{2} - 2\beta \cos \phi_+ \cos (\varphi + \phi_-) \right] + C\dot{\phi}_+ \quad (3.9)$$

and n is the number operator and $E_c = e^2/2C$.

3.2 Principle of operations

The readout technique exploits the JDPD's potential energy tunability to perform phase detection. The timing diagram of the protocol is shown in Fig. 3.3. The detection is composed of four separate steps. The JDPD is first configured in a harmonic shape, by tuning $\phi_+ = \pi/2$. This sets the JDPD in the "Ready" state, as shown in the first panel of Fig. 3.3. The Hamiltonian (3.9) then describes an LC oscillator:

$$H_{\text{ho}} = 2E_C n^2 + E_L \varphi^2 \quad (3.10)$$

where $\omega_0 = \sqrt{4 E_C E_L}/\hbar$ is the natural frequency of the equivalent harmonic oscillator. Assuming the JDPD starts from its ground state, a signal is applied to its input node as an external current $I(t)$. Consequently, the system evolves according to the Hamiltonian of a driven LC oscillator:

$$H_{\text{tot}} = H_{\text{ho}} - \frac{\Phi_0 I(t)}{2\pi} \varphi, \quad (3.11)$$

3.2. PRINCIPLE OF OPERATIONS

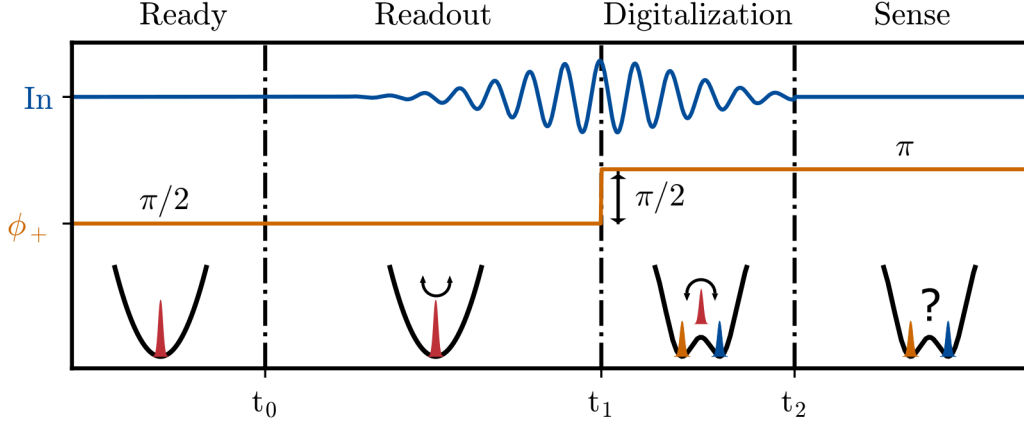


Figure 3.3: Timing diagram of the phase detection performed with the JDPD. Initially, no external flux is applied. To get the harmonic shape, a $\pi/2$ magnetic flux is applied. At this point, the JDPD interacts with the microwave tone to be detected, which generates a harmonic motion of the JDPD’s wavefunction. The potential energy is then diabatically biased (flux-switched) to a double-well configuration, such that the wavefunction will collapse in the left or right well depending on the initial phase displacement of the microwave tone.

which gives the start to the “Readout” step of the detection protocol, represented in the second panel of Fig. 3.3. For simplicity, we consider the case in which

$$I(t) = I_0 \sin(\omega_r t + \theta_r) \quad (3.12)$$

where I_0, ω_r and θ_r are respectively the amplitude, the angular frequency and the displacement of the input tone. Under this current drive, the system follows the time evolution of $I(t)$ with an amplitude φ_0 and phase θ_0

$$\varphi(t) = \varphi_0 \sin(\omega_r t + \theta_0) \quad (3.13)$$

where, in general, φ_0 and θ_0 are functions of the external tone frequency ω_r , according to the current-phase transfer function of the resonator. If the frequency of the external perturbation ω_r is much smaller than the natural frequency of the harmonic oscillator ω_0 , then

$$\varphi_0 \approx 2\pi \frac{LI_0}{\Phi_0} \quad (3.14)$$

$$\theta_0 \approx \theta_r. \quad (3.15)$$

Consequently, the variable φ acquires the same phase of the input current $I(t)$, which we want to sense. At this point, the JDPD is rapidly flux-switched to a bistable configuration, by increasing the common flux ϕ_+ by $\pi/2$, reaching a total value of $\phi_+ = \pi$. According to the sign of φ at the flux-switch time t_1 , the wavefunction of the system will primarily be confined in either of the two wells, depending on the initial phase θ_r imposed to the coherent state by the input

current $I(t)$. Right after, $I(t)$ is turned off to prevent further dynamics of the wavefunction after the “Digitalization” is completed.

The position of the phase particle can now be “Sensed” as the two possible outcomes of φ operator will have opposite values, which corresponds to opposite signs for the current flowing through the central inductor L , since:

$$I = \frac{\Phi_0}{2\pi L}\varphi. \quad (3.16)$$

So far, we have explained how to map the initial phase θ_r of the input current $I(t)$ to the occupation probability of the wavefunction of the JDPD in the bistable configuration. It is thus important to describe some details of the dynamics during the flux-switch, which unveils the advantages of our detection technique. The JDPD is not required to be in resonance with the input tone which we want to sense. This has the tremendous advantage that, for our device, the emission spectrum in the bistable configuration can be designed to be far from the absorption spectrum of any nearby quantum circuit. Therefore, the emitted photons generated during the relaxation of the system during the “Digitalization” step [79, 135, 136] will likely not harm the coherence of the surrounding circuitry. Moreover, the symmetric topology [137, 138] of our circuit suppresses the flux-induced backaction at the active node. As any real device is going to have asymmetries because of fabrication uncertainties, we can circumvent possible problems related to such imperfections by properly adjusting the differential flux ϕ_- before the protocol starts.

From these observations, we conclude that the JDPD could be efficiently integrated close to one or multiple superconducting qubits to implement a digital readout protocol, similar to the JPM one, but with less stringent requirements in terms of design and flux-control to ensure high-fidelity operations.

3.3 Study of the detection protocol in classical regime

The timing diagram, shown in Fig. 3.3 has been simulated numerically using the superconducting circuit simulator PSCAN2 [17] and the Lindblad master equation solver *mesolve* implemented in QuTip [18]. Both frameworks permit us to extract fundamental features of the JDPD’s phase detection technique, which allows us to determine the pros and cons of our approach. In this Section, I will present the numerical analysis performed with PSCAN2.

Simulations have been carried out inspired by the design of the real device. In particular, the central inductor has been chosen to be $L = 200 \text{ pH}$ and junctions with a critical current $I_c = 5 \text{ }\mu\text{A}$. According to Eq. 3.5, these parameters lead to a $2\beta_L = 7$ which is large enough to ensure the formation of a double well potential when a flux-switch is applied. To simulate adequately the device, and in particular to study properly the JJs behaviour, we have adopted the Tunnel Junction Microscopic (TJM) model implemented in PSCAN2. This mathematical model,

3.3. STUDY OF THE DETECTION PROTOCOL IN CLASSICAL REGIME

based on the Werthamer equations [50, 139], is the most sophisticated description of a Josephson Junction. TJM simulations require some input parameters [140, 141]:

- *Dirichlet coefficients*: These coefficients come from the Fourier series approximation of the tunnel current density of the junction [47, 140] and are derived from the Bardeen–Cooper–Schrieffer (BCS) theory by Larkin and Ovchinnikov [142], starting from the energy gaps Δ_1, Δ_2 of the two superconducting electrodes, the temperature T and the broadening of subharmonic-gap singularities (Riedel peaks)[143].
- β_C : McCumber parameters, a dimensionless capacitance of a JJ [46–48]
- V_g : Superconducting gap voltage
- $I_c R_n / V_g$: ratio between the the critical current I_c and the normal resistance of the junction R_n to the superconducting gap V_g related to the suppression of the critical current [50]
- R_n / R_{sg} normal-to-subgap resistance ratio

In the case of our simulations, the parameters have been estimated starting from the characteristics of the JJs produced by the industrial process SEEQC. They are reported in table 3.4: To simulate the phase detection, a current source is attached to the JDPD 's input node as shown in Fig. 3.2. Simulations have been carried out by considering a sinusoidal waveform with amplitude $I_0 = 1 \mu A$ and frequency of $7 GHz$ modulated by a gaussian envelope with a standard deviation of $200 ps$. As shown later in this thesis, this amplitude is in the range of the JDPD sensitivity since the junction critical current is around $5 \mu A$. However, this value does not limit the applicability of the JDPD in the field of signal detection. It's possible to demonstrate that the sensitivity of our detector can be properly adjusted by changing opportunely the values of its central inductor L and the critical current of the two junctions I_c . The input tone frequency has been chosen to be in the microwave regime, near the typical frequency of superconducting resonators used to readout the state of the superconducting qubits [144].

Our technique exploits the JDPD's flux tunability to perform phase detection. In the case of our simulations, the JDPD's flux state is tuned by two-phase generators [17] inserted in series to the two JJs in the two superconducting loops. We assume the duration of the flux switch t_{flip} is equal to $50 ps$ corresponding to a $20 GHz$ tone in the frequency domain. This is a realistic estimation since our goal is to provide the flux-switch signal with an integrated SFQ circuit, thus $20 GHz$ clock has been proposed to be optimal in this type of superconducting devices integrated into a superconducting quantum processor[9, 10]. However, the JDPD is expected to work with other values of the flux switch duration t_{flip} . The results of our numerical analysis in PSCAN2 are shown in Fig. 3.5, where the time evolution of the sinusoidal input tone I_n , the common flux ϕ_+ , φ, φ_1 and

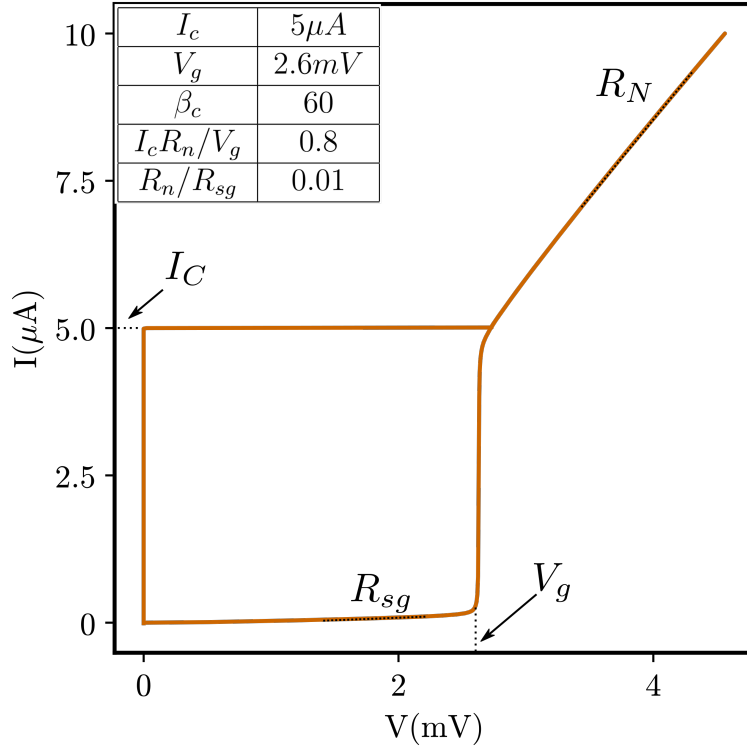


Figure 3.4: Simulated IV characteristic of the junctions employed for the JDPD’s realization. The JJs are realized with a stack of $Nb/AlO_x/Nb$. TJM simulations have been carried out with $V_g = 2.6 mV$, $I_c = 5 \mu A$ and $\beta_c = 60$, as reported in the inset.

φ_2 are reported. The system is initialized in the harmonic state corresponding to $\phi_+ = \pi/2$ which sets the device in the step “Ready” shown in Fig. 3.5. Around $t = 0.2 ns$, the input signal is switched on and it starts to drive the phase φ around the minimum of potential energy, according to the equation:

$$\varphi(t) = \varphi_0 \sin(\omega t + \theta_r) \quad (3.17)$$

where $\omega/2\pi = 7 GHz$ and θ_r are respectively the frequency and the displacement of the sinusoidal input signal and $\varphi_0 = 2\pi L I_0 / \Phi_0$ is the maximum elongation during the motion.

Discrimination between the two states is made at $t = 0.54 ns$ when the flux switch is applied, which means $\phi_+ = \pi/2 \rightarrow \pi$ in a time duration of $50 ps$. In our simulations, this specific time is chosen to be symmetrical with respect to the beginning and the end of the input tone. As a consequence, the potential energy takes the double well configuration and the wavefunction collapses in either the left or right well depending on its initial displacement θ_r . In the case of Fig. 3.5, simulations have been carried out in the case of $\theta_r = 0$ (blue line) and $\theta_r = \pi$ (red line).

At $t = t_2$ the measurement sequence is completed and it’s possible to detect the JDPD’s status. As shown in Fig. 3.5, φ assumes opposite values depending on the value of θ_r . From a physical point of view, these phase states correspond to

3.3. STUDY OF THE DETECTION PROTOCOL IN CLASSICAL REGIME

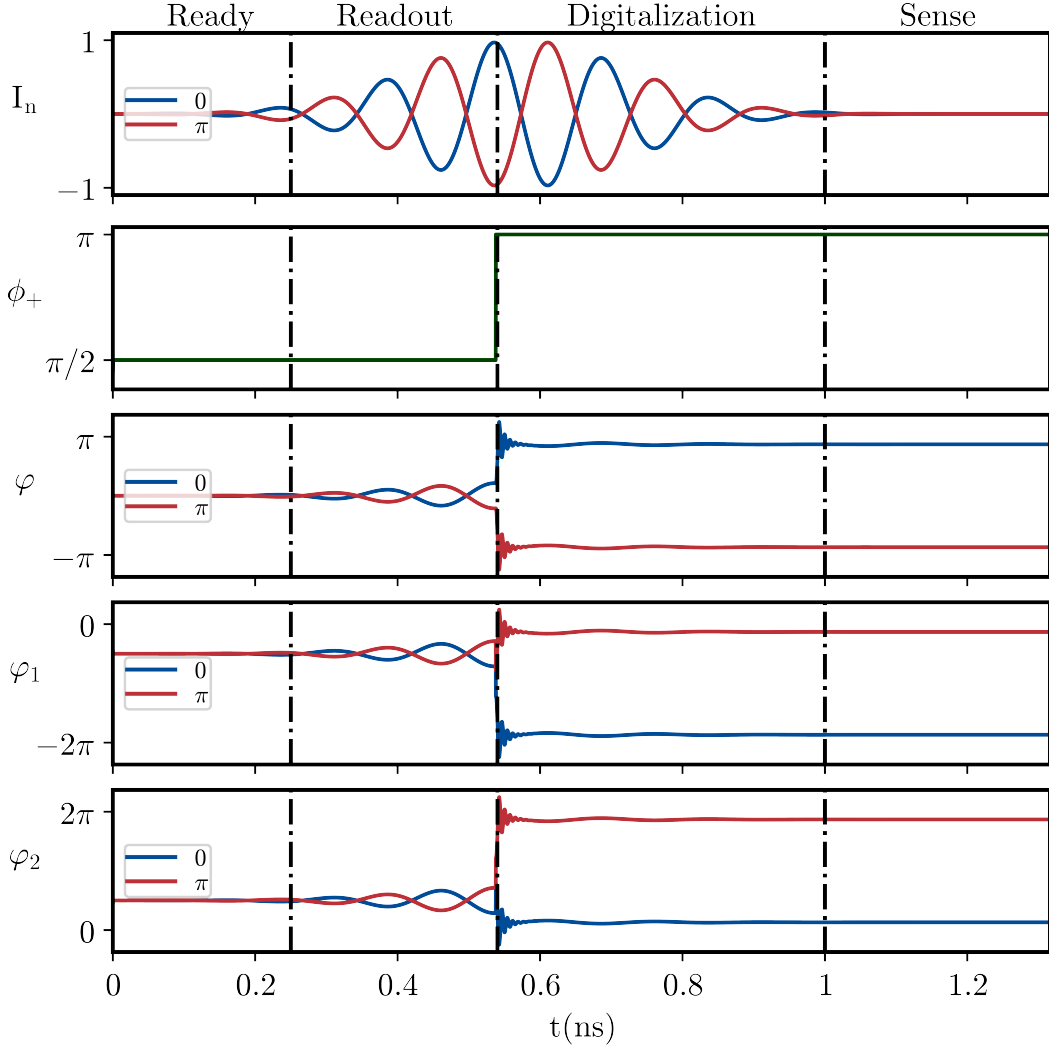


Figure 3.5: Simulations of the phase detection performed in PSCAN2 [17] for $\theta_r = 0$ (blue line) and $\theta_r = \pi$ (red line). I_n is the input tone that interacts with the detector. Simulations have been carried out by considering a sinusoidal waveform with amplitude $I_0 = 1 \mu A$ and frequency of $7 GHz$ modulated by a Gaussian envelope with a standard deviation of $200 ps$.

ϕ_+ is the common flux to change the detector's state. φ, φ_1 and φ_2 are the phase drop across the central inductor, the junctions J1 and J2 respectively. The dashed lines separate the 4 detection steps.

opposite currents flowing in the inductor L since:

$$I_{\text{flowing through } L} = \frac{\Phi_0}{2\pi} \frac{\varphi}{L} \quad (3.18)$$

which are equal to $I_{\text{flowing}} = \pm 4\mu A$ taking in consideration the parameters selected for this simulation.

3.4 Study of the detection protocol in quantum regime

PSCAN2 [17] is a very powerful tool which allows us to extrapolate fundamental features of the detection technique. However, since it is a classical superconducting circuit simulator, it's not straightforward to calculate some quantities such as the detection fidelities. This is the reason behind the use of QuTip, which has been employed to extrapolate some key characteristics of the JDPD phase detection.

To perform simulations with QuTip we need to pass from the classical to the quantum description of an electrical circuit. This can be done in the framework of the Hamiltonian Eq. 3.9. by replacing the classical variables with operators [41, 42]:

$$\begin{aligned} \varphi &\rightarrow \hat{\varphi} \\ n &\rightarrow \hat{n} \\ H &\rightarrow \hat{H} \end{aligned} \quad (3.19)$$

In this way, the Hamiltonian in Eq. 3.9 takes the form:

$$\hat{H} = 2E_c \hat{n}^2 + E_L \left[\frac{\hat{\varphi}^2}{2} - 2\beta \cos \phi_+ \cos (\hat{\varphi} + \phi_-) \right] + C \dot{\phi}_+ \quad (3.20)$$

The energy values E_L , E_J and E_C are derived from the formulas 1.11, 1.10 and 1.12 by replacing the same parameters and conditions adopted in PSCAN2 simulations. These quantities come from the JDPD layout realization as discussed in Chapter 4. By considering a central inductor of $L = 200 \text{ pH}$ and $I_c = 5 \mu A$ for the two junctions, we have estimated $E_L = 827 \text{ GHz}$ and $E_J = \beta E_L = 2483 \text{ GHz}$. To calculate E_C , we started from the foundry specification for junctions fabrication [145]. We get a contribution for each junction equal to $C = 35 \text{ fF}$ and a total contribution to $2 E_C = 0.24 \text{ GHz}$.

Therefore, the system's energy is dominated by the Josephson and inductive contribution and these parameters lead to a frequency of $\omega_0/2\pi = 40 \text{ GHz}$ when the potential is in the harmonic shape and $\omega/2\pi = 106 \text{ GHz}$ in the double well configuration, calculated approximating the potential by a quadratic function around one of its two minima.

For the input tone, simulations have been carried out by considering a sinusoidal waveform with amplitude $I_{in} = 1 \mu A$ and frequency 7 GHz modulated by a

gaussian envelope with a standard deviation of 200 *ps*, as in the case of the classical simulations in PSCAN2. We assume the duration of the flux switch t_{flip} is equal to 50 *ps* corresponding to a 20 *GHz* tone in the frequency domain. Simulations have been done adopting the Lindblad master equation solver *mesolve* [18] implemented in the QuTip function *mesolve*, which describes the time evolution of the density matrix of a quantum system that is coupled to the environment [146, 147]. It is used to describe the dynamics of open quantum systems, where the system is coupled to an environment that can cause decoherence and dissipation.

The general form of the Lindblad master equation is given by:

$$\frac{d\hat{\rho}}{dt} = -i \left[\hat{H}, \hat{\rho} \right] + \sum_k \left(\hat{L}_k \hat{\rho} \hat{L}_k^\dagger - \frac{1}{2} \left\{ \hat{L}_k^\dagger \hat{L}_k, \hat{\rho} \right\} \right) \quad (3.21)$$

where $\hat{\rho}$ is the density matrix of the system, \hat{H} is the Hamiltonian operator, and the \hat{L}_k are the Lindblad operators. The first term on the right-hand side of the equation represents the unitary evolution of the system, which is governed by the Hamiltonian. The second term represents the non-unitary evolution of the system, which is caused by the coupling to the environment. The Lindblad operators describe the interactions between the system and the environment, and the terms $\hat{L}_k \hat{\rho} \hat{L}_k^\dagger$ and $\{\hat{L}_k^\dagger \hat{L}_k, \hat{\rho}\}$ describe the decoherence and dissipation of the system, respectively [148, 149].

It's important to note that the Lindblad Master equation is only a phenomenological model, it can capture the essence of a wide variety of physical processes in different systems, but a correct physical derivation might require specific models for the environment and its interaction with the system [146, 147, 149].

To describe the time evolution of the JDPD's wavefunction, we have truncated the series in Eq. 3.21 at the first order and considered as Lindblad operator L_1 the quantity:

$$\hat{L}_1 = \sqrt{\gamma} \hat{a} \quad (3.22)$$

where γ is the dissipation rate and \hat{a} is the annihilation operator, through which the environment couples to the system, which are defined by the system of equations:

$$\begin{cases} \hat{\varphi} = \left(\frac{2E_C}{E_L} \right)^{\frac{1}{4}} (\hat{a} + \hat{a}^\dagger) \\ \hat{n} = \left(\frac{E_L}{32E_C} \right)^{\frac{1}{4}} i (\hat{a} - \hat{a}^\dagger) \end{cases} \quad (3.23)$$

This model corresponds to a relaxation map [146–148], which describes the JDPD's energy loss after the excitation provided by the fluxes and the input tone, assuming the temperature of the system equal to zero [150]. The relaxation rate γ has been extracted fitting the PSCAN2 curves simulations, reported in the previous Section. In our understanding, this technique is the most accurate estimation of the dissipation since the TJM model provides a solid description of the junctions during the phase detection protocol. We have estimated $1/\gamma \simeq 0.02$ *ns*

The JDPD's wavefunction evolution is shown in Fig. 3.6 A. The system is initialized in the harmonic state and the wavefunction collapses in the ground state of the harmonic potential. This corresponds to the "Ready" state reported in the first panel of Fig. 3.3. At $t = t_0$, the input signal starts to drive the wavefunction around the minimum. In our simulations, the sinusoidal waveform has a duration of 5 periods, which corresponds to 715 ps for a frequency of 7 GHz. Under this current drive, the JDPD's wavefunction is described by a Gaussian wavepacket centred at the classical value of position $\langle \hat{\varphi}(t) \rangle$:

$$\langle \hat{\varphi} \rangle = \varphi_0 \sin(\omega t + \theta_0) \quad (3.24)$$

where $\omega/2\pi = 7 \text{ GHz}$ and θ_0 are respectively the frequency and the displacement of the sinusoidal input signal and $\varphi_0 = 2\pi L I_0 / \Phi_0$ is maximum elongation during the motion. During this step, the wavefunction is described by a Gaussian wavepacket with a constant standard deviation constant given by [151]:

$$\sigma = 2e \sqrt{\frac{2Z_0}{\hbar}} = 0.31 \quad (3.25)$$

where $Z_0 = \sqrt{L/C}$.

We would like to point out that σ is an important parameter in our detection protocol. As explained in more detail later in the text, σ can help us to quantify the amplitude of the input tone to achieve the maximum probability. Since it's related to the physical parameters of the system as L and C , we can play with these parameters to change the JDPD's sensitivity.

At $t = t_1$, the JDPD is rapidly flux-switched to a bistable configuration, by increasing the common flux ϕ_+ by $\pi/2$, which reaches a total value of $\phi_+ = \pi$. In our simulations, t_1 is chosen to centre the flux switch with respect to the beginning and the end of the input tone. As in the classical case, the wavefunction of the system will primarily be confined in either of the two wells, depending on the initial phase θ_r imposed to the coherent state by the input current $I(t)$.

For instance, in the left panel of Fig. 3.6 an initial displacement $\theta_r = 0$ has been considered for the sinusoidal input tone. As a consequence, the wavefunction collapses in the left well after the flux-switch tone. The same sequence has been simulated in the right panel of Fig. 3.6 but with an initial displacement $\theta_r = \pi$. In this case, the wavefunction falls in the right well. The central panel refers to the case in which the input tone is not applied. When at $t = t_1$ the potential is flipped in its double-well configuration, the wavefunction is split in half and we have an equal probability of measuring it in the left and right well.

While collapsing in the well, one may ask which is the induced backaction on the input signal's source. In this transient, the JDPD can be modelled as an effective voltage source V_j that generates backaction [79]. According to the ac Josephson relation [46, 47], the produced backaction signal is proportional to the time derivative of $\dot{\varphi}(t)$; therefore it will have the same frequency as the phase particle relaxing in the trapped well. As shown in Fig. 3.6, after the flux-switch the JDPD's waveform performs a damped non-harmonic motion, where

the oscillations frequency gradually increase [135, 136]. However, the phase detection protocol does not require the JDPD to be in resonance with the input signal source, and consequently, one can design the detector in such a manner that these oscillations are outside the source’s absorbing spectrum preventing inducing backaction on the system. For instance, in the implemented device, the selected parameters lead to oscillations in the range of 106 GHz , as shown in Fig. 3.6 B, which is around the frequency of one of the two wells in the potential flipped configuration (i.e $\phi_+ = \pi$) and in general much higher with respect to the input signal frequency set to 7 GHz .

The sequence can be completed at $t = t_2$ when the position of the phase particle can be “Sensed” as the two possible outcomes of a measurement of $\hat{\varphi}$ operator will have opposite values, which correspond to opposite signs for the current flowing through the central inductor L , since $\langle I \rangle = \frac{\Phi_0}{2\pi L} \langle \varphi \rangle$. Fig. 3.7 A exhibits the wavefunction’s probability density $|\Psi|^2$ at $t = t_2$ for several values of the input tone’s displacement θ_r . According to these simulations, a fidelity close to 1 is in principle achievable. In particular, the plot shows that the digitization works not only for $\theta_r = 0$ or $\theta_r = \pi$ but in a broader range of θ_r . Given the selected parameters for the simulation, the wavefunction collapses in the left well when $\theta_r \in [1.9, 4.2]$ and in the right well when $\theta_r \in [0, 1] \cup [5, 2\pi]$. This evidence makes the JDPD readout approach suitable even if the input signal does not have a pure $0 \rightarrow \pi$ separation in phase. However, the fidelity is affected by several conditions/ parameters and the detection should be optimised to achieve the best detector’s performance. One of these regards the input signal’s amplitude that sets the wavefunction maximum elongation φ_0 . A convenient way to exhibit the effect of the input signal on fidelity is to express the wavefunction’s maximum elongation φ_0 in a unit of the wavefunction’s root mean square (RMS) σ :

$$\varphi_0 \equiv n\sigma \quad (3.26)$$

As displayed in Fig. 3.7 B., the fidelity is maximized for n in the range $[1, 6]$. Values below this range correspond to small oscillations around $\varphi = 0$. Therefore, when a flux-switch is supplied, the wavefunction is split between the two wells leading to a fidelity reduction. Instead, when $n > 6$, the barrier height is not large enough to confine the wavefunction. Once trapped in one of the two wells, the wavefunction oscillates so much that the probability is redistributed between the two states.

Another factor that affects the fidelity is the flux switch duration t_{flip} . According to simulations reported in Fig. 3.7 C, a fidelity close to 1 is achievable when the $t_{flip} < 10 T$, where $T = 2\pi/\omega$ and $\omega/2\pi = 7\text{ GHz}$ is the simulated frequency for the input tone. A slow rise time for the barrier height induces a redistribution of probability between the two wells at each input tone’s period. Considering the typical frequencies for superconducting resonators, optimal values for t_{flip} are in the order of hundreds of ps . It’s important to point out that the possibility to manipulate diabatically the potential shape has been already exploited both experimentally and theoretically in Ref. [124–126]. These papers demonstrated coherent oscillations of a tunable superconducting flux qubit by manipulating

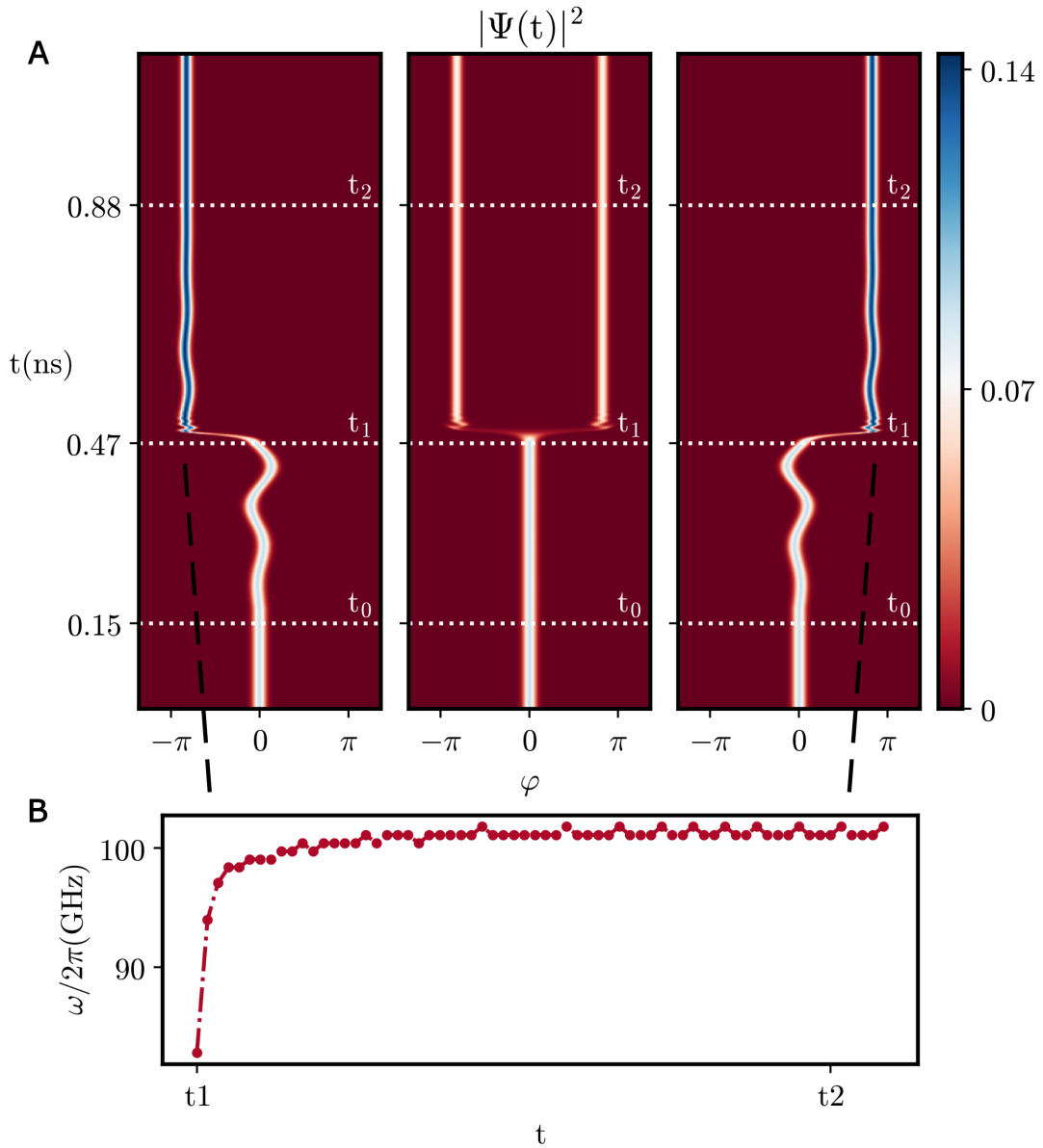


Figure 3.6: Simulations of JDPD with QuTip [18].(A) The JDPD wavefunction has been simulated according to the timing diagram reported in Fig. 3.3. In the left panel, an initial displacement $\theta_r = 0$ has been considered for the sinusoidal input tone. As a consequence, the wavefunction collapses in the left well after the flux-switch tone. The same sequence has been simulated in the right panel but with an initial displacement $\theta_r = \pi$ of the input tone. In this case, the wavefunction falls in the right well. The central panel refers to the case in which the input tone is not applied. When at $t = t_1$ the potential is flipped in its double-well configuration, the wavefunction is split in half and we have an equal probability of measuring it in the left and right well. (B) While falling in the well, the JDPD's wavefunction performs damped non-harmonic oscillations which leads to a gradual increase of the frequency

3.4. STUDY OF THE DETECTION PROTOCOL IN QUANTUM REGIME

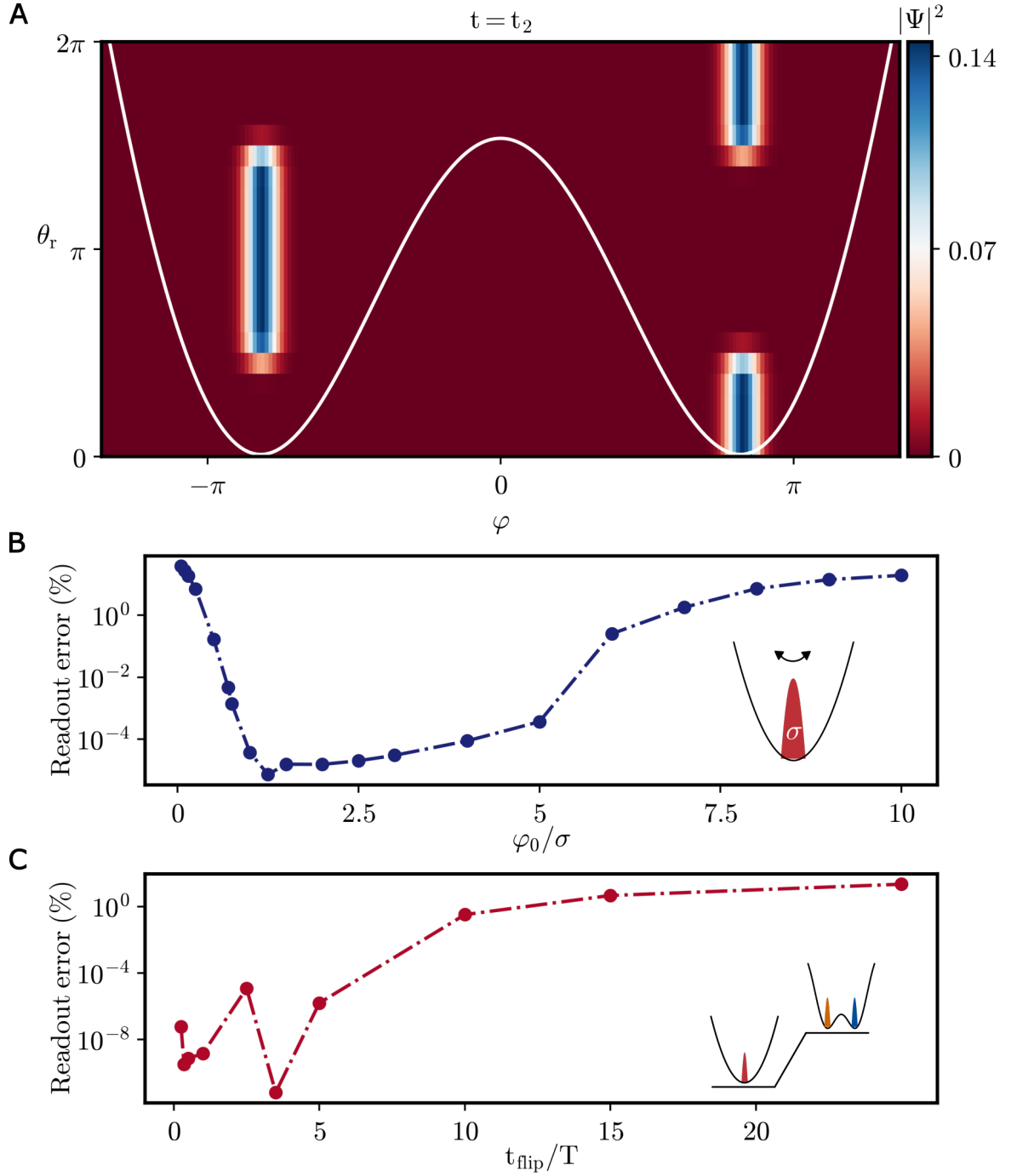


Figure 3.7: (A) JDPD's probability distribution $|\Psi(t)|^2$ at $t = t_2$ as a function of the initial displacement θ_r of the input tone.

(B) Readout error as a function of the wavefunction's maximum elongation φ_0 during the driven harmonic motion. φ_0 is expressed in unit of the wavefunction's RMS σ .

(C) Readout error as a function of flux switch rise time t_{flip} normalized in terms of input signal's period T .

its energy potential with nanosecond-long pulses of magnetic flux. Given the resemblance between the JDPD and the device reported in their paper, we can argue that fast potential manipulation can be performed also in the case of our detector.

A possible approach to generate pulses with hundreds of *ps* rise time involves the use of a dedicated SFQ flux generator which can operate with a clock of tens of GHz [9, 10, 78]. A more detailed discussion about the integration of the JDPD with an SFQ-based platform can be found in the Section.

3.5 Asymmetries correction

A perfectly symmetrical JDPD is a fundamental requirement to obtain state-independent fidelity and guarantee the working condition of the detector. In a real device, the JDPD will likely deviate from being perfectly symmetric due to various factors but mainly by parameter spread in the junctions due to the fabrication process and different flux trapped in the two JDPD branches.

In the case of an asymmetrical device, the potential energy 3.5 becomes:

$$U(\varphi) = \frac{1}{2L} \left[\left(\frac{\Phi_0}{2\pi} \right)^2 \varphi^2 - \frac{\Phi_0}{2\pi} \left(I_{c+} \cos(\phi_+) \cos(\varphi + \phi_-) - I_{c-} \sin(\phi_+) \sin(\varphi + \phi_-) \right) \right] \quad (3.27)$$

where the variables I_{c+} and I_{c-} have been introduced:

$$\begin{cases} I_{c+} = I_{c1} + I_{c2} \\ I_{c-} = I_{c1} - I_{c2} \end{cases}$$

Note that when the Josephson critical currents I_{c1} and I_{c2} are equal, $I_{c-} = 0$ and the equation 3.5 is retrieved. The Fig. 3.8 A shows the potential shape for $\phi_+ = \pi/2$, $\phi_- = 0$ and several values of $I_{c-} \in [-1, 1] \mu A$. The presence of $I_{c-} \neq 0$ leads to a shift in the potential minimum and consequently, the wavefunction acquires an offset with respect to $\varphi = 0$. If a flux switch is applied in absence of the external input tone, the wavefunction is distributed mostly in the deeper well, since the asymmetry generates an unbalance between the left and right states. This makes the fidelity state-dependent and worsens the detector performance.

The sequence described above has been simulated with QuTip [18] in Fig. 3.8 B (1) and (2). In the absence of any input tone, the numerical analysis has been performed considering $I_{c+} = 9 \mu A$ and $I_{c+}/I_{c-} = \pm 11\%$, corresponding to a variation of 20% in the critical current value, which is generally larger than the typical fabrication spread. In both simulations, the potential is flipped at $t = t_1$ and the wavefunction collapses always in the same well with a probability of 99.999%.

By adjusting opportunely the value of ϕ_- , state-independent fidelity can be recovered. This is shown in Fig. 3.8 B, where, in the same conditions of simulations

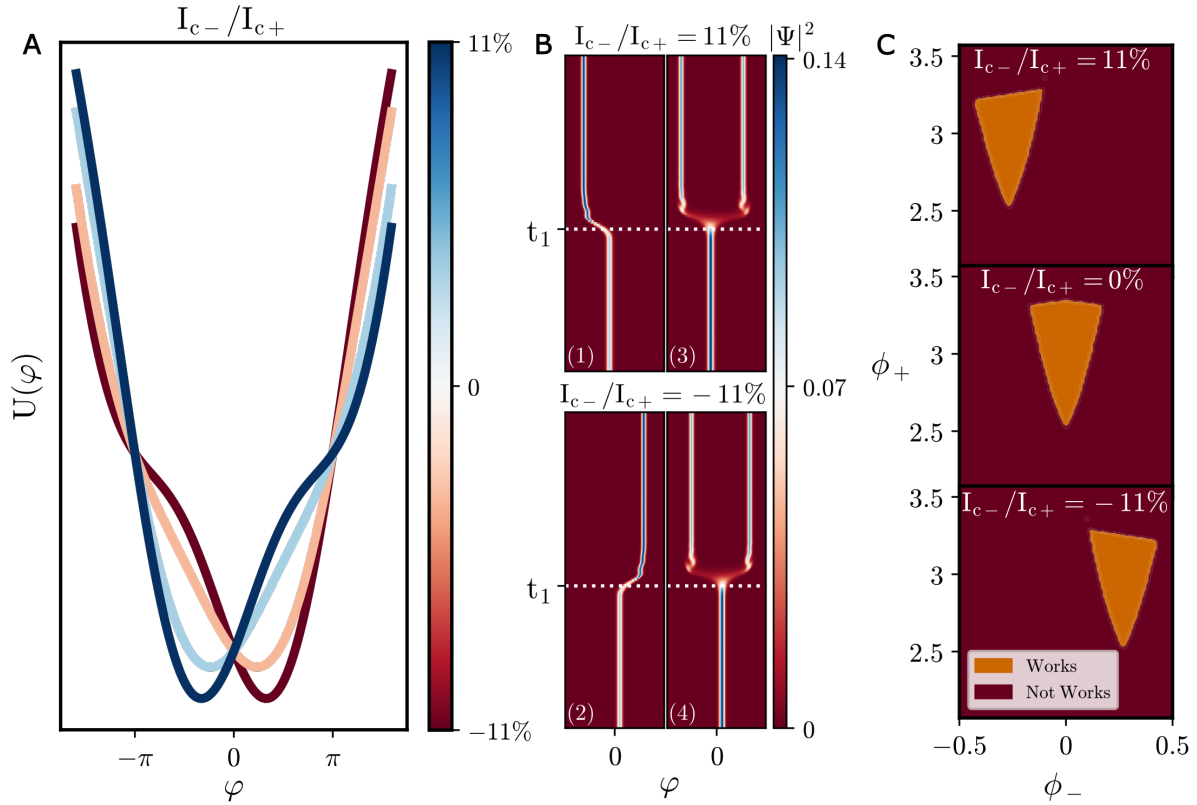


Figure 3.8: (A) JDPD's potential shape when $\phi_+ = \pi/2$ and $\phi_- = 0$ for several values of the ratio I_{c-}/I_{c+} . The presence of asymmetries leads to a shift in the potential minimum and, consequently, the wavefunction acquires an offset with respect to $\varphi = 0$. (B) (1-2) In the absence of external input, an applied flux-switch makes the wavefunction collapse in the two wells with a different probability. In these QuTip simulations, performed with $I_{c+} = 9\mu A$ and $I_{c-}/I_{c+} = \pm 11\%$, we get 99.999% of probability to reach the left (1) and right well (2). (3-4) However, state-independent fidelity can be achieved by adjusting the value of ϕ_- to $\phi_- \simeq 0.46$. (C) The numerical analysis performed with QuTip is supported by classical simulations made in PSCAN2. Sweeping on ϕ_+ and ϕ_- , we have specific regions in which the JDPD is capable of performing correctly phase detection. Simulations have been carried out considering the same parameters adopted for the QuTip's ones, i.e $I_{c+} = 9\mu A$ and $I_{c+}/I_{c-} = \pm 11\%$. In particular, the top panel refers to the case in which $I_{c-}/I_{c+} = 11\%$, the central one corresponds to perfect symmetrical JDPD and the one in the bottom panel shows the condition when $I_{c-}/I_{c+} = -11\%$.

reported in Fig. 3.8 B (1) and (2), the state-independent probability has been restored by applying a $\phi_m \simeq \pm 0.46$.

The numerical analysis performed with QuTip is confirmed by classical simulations made in PSCAN2 shown in Fig. 3.8 C. Sweeping on ϕ_+ and ϕ_- , we have determined regions in which the JDPD is capable of performing correctly phase detection, as expected in the symmetrical case.

Simulations have been carried out considering the same parameters adopted for the QuTip's ones, i.e $I_{c+} = 9\mu A$ and $I_{c+}/I_{c-} = \pm 11\%$. In particular, the top figure in Fig. 3.8 C refers to the case in which $I_{c-}/I_{c+} = 11\%$, the central one corresponds to perfect symmetrical JDPD and the bottom one shows the condition when $I_{c-}/I_{c+} = -11\%$. These considerations demonstrate that our detector is robust with respect to asymmetries that can be corrected by properly changing ϕ_+ and ϕ_- .

3.6 JDPD technique applied to superconducting qubit readout

In this Chapter, we have illustrated a phase detection technique based on a Josephson Digital Phase Detector (JDPD). Simulations show that digitalization can reach close-to-1 fidelities in a nanosecond timescale with negligible backaction on the source. Due to its flux tunability, our detector exhibits resilience to asymmetries generated for example from fabrication spread. These characteristics make the JDPD approach particularly suitable for the readout of superconducting qubits. As discussed in Chapter 2, a superconducting Quantum Information Platform (QIP) is built around high Q resonators whose bare resonant frequency ω_r is shifted by a factor χ , depending on the state of dispersively coupled qubits [40, 152]. The readout is then obtained by probing the dressed resonant frequency $\omega_a = \omega_r \pm \chi$ and associating the binary result to a measurement of the Pauli operator σ_z related to the qubit. This task can be performed very efficiently by sending a readout pulse at a frequency ω resonating with either bare resonator ω_r , ground state frequency $\omega_g = \omega_r - \chi$ or excited state $\omega_e = \omega_r + \chi$ [89, 153]. As clear from Fig. 3.9 the readout pulse will be processed in a way that depends on the particular choice of ω .

A similar approach can be pursued in the case of our detection technique. As shown in Fig. 3.9, we can probe the cavity sending a tone at $\omega = \omega_r$ to be maximally sensitive to the phase response of the dressed resonator. After the readout pulse gets dressed, it's sent to an inductively coupled JDPD set to be in the "Ready" state. At this point, the JDPD will behave almost as a purely inductive element at input frequency ω_r , so $\varphi(t)$ will be phase-locked to the current injected by readout tone and consequently directly encoding the collapsed qubit state.

Our detector is well suited to be operated by an SFQ circuitry [154, 155], which can provide both the flux-flip pulse and the readout pulse. Thanks to their very low power dissipation, energy-efficient SFQ circuits could be safely located con-

3.6. JDPD TECHNIQUE APPLIED TO SUPERCONDUCTING QUBIT READOUT

tigiously to the quantum chips and they offer the possibility to operate at very high speeds (tens of gigahertz clock) with small jitter [78]. Therefore, an SFQ circuitry can grant the required phase locking between the input pulse and flip pulse making the detection possible with fidelities close to 1.

The result of the measurement can be stored in classical circulating current in the JDPD inductor. This current can be measured using an SFQ balanced comparator [81, 156] producing SFQ-encoded digital output. Then, these SFQ data can further be digitally processed and memorized. The synchronisation of all the protocol steps by means of locally generated high-speed SFQ pulses promises major reductions in system footprint and latency so that this device can be exploited for implementing low-latency quantum feedback and control conditioned on the result of qubit measurement.

Another benefit of the use of high-speed SFQ circuitry stands in the possibility of performing multiple measurements on the same cycle, thus allowing averaging to reduce noise contribution and improve fidelity. This is shown in Fig. 3.10 where the measurement sequence with multiple flux-flips has been simulated in QuTip.

Consequently, to unlock the JDPD's potential, we are currently designing a complete circuit which includes SFQ pulses generators for both input tone and flux-switch pulse, as discussed in more detail in the next Chapter.

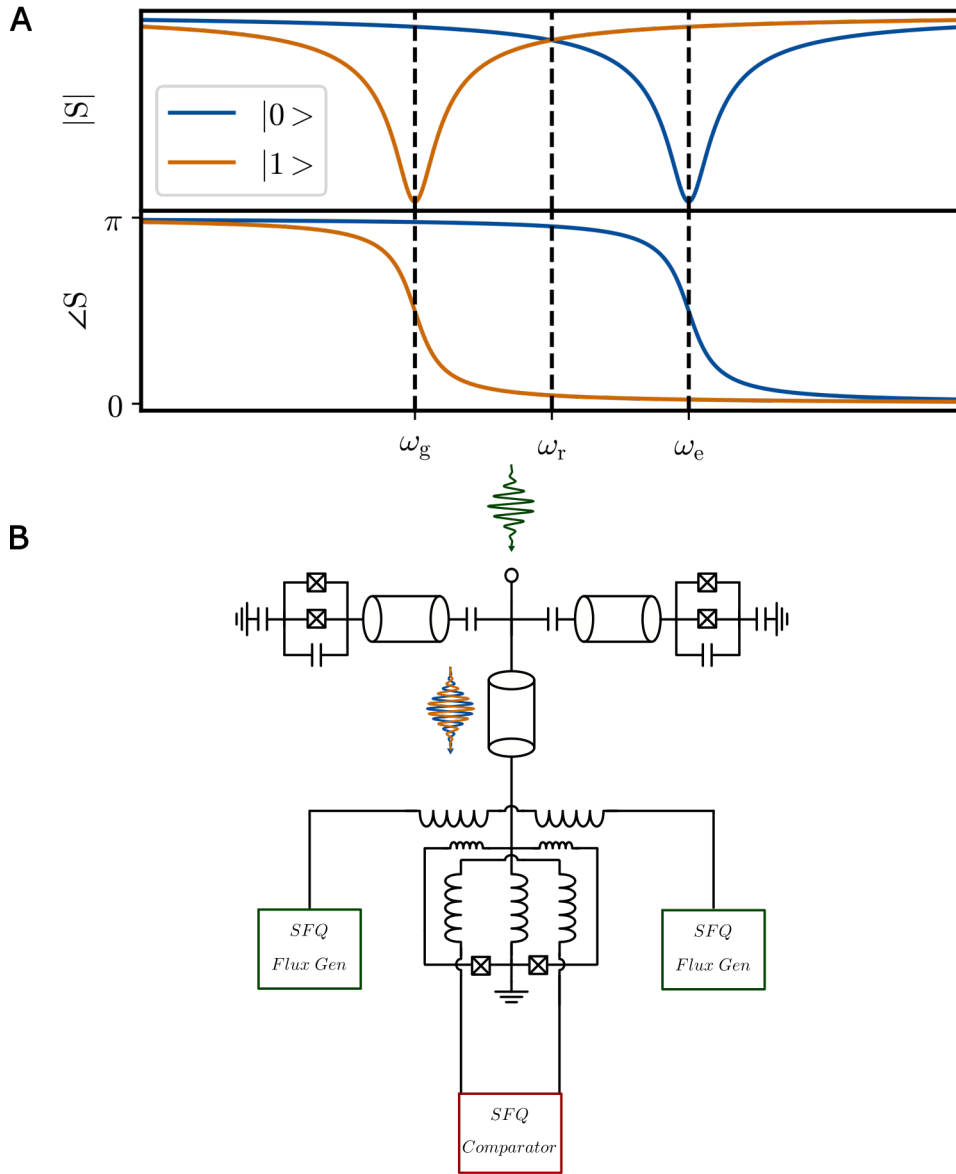


Figure 3.9: (A) Sketch of the measured S parameters in a typical superconducting qubit readout. A shift of the resonance frequency is observed depending on the qubit's state, which is visible both in amplitude $|S|$ and phase $\angle S$ and. To exploit the JDPD detection technique, we need to maximize the separation between the state $|0\rangle$ and $|1\rangle$ in phase. This operation can be done by probing the cavity at the resonator bare frequency, i.e $\omega = \omega_r$.

(B) Possible experimental setup to measure the qubit's state involving the JDPD. In this sketch, two resonator-qubit systems are capacitively coupled to a feedline connected inductively to a JDPD device. The detector's states are tuned by an SFQ flux generator and the measurement output is digitalized by using an SFQ comparator.

3.6. JDPD TECHNIQUE APPLIED TO SUPERCONDUCTING QUBIT READOUT

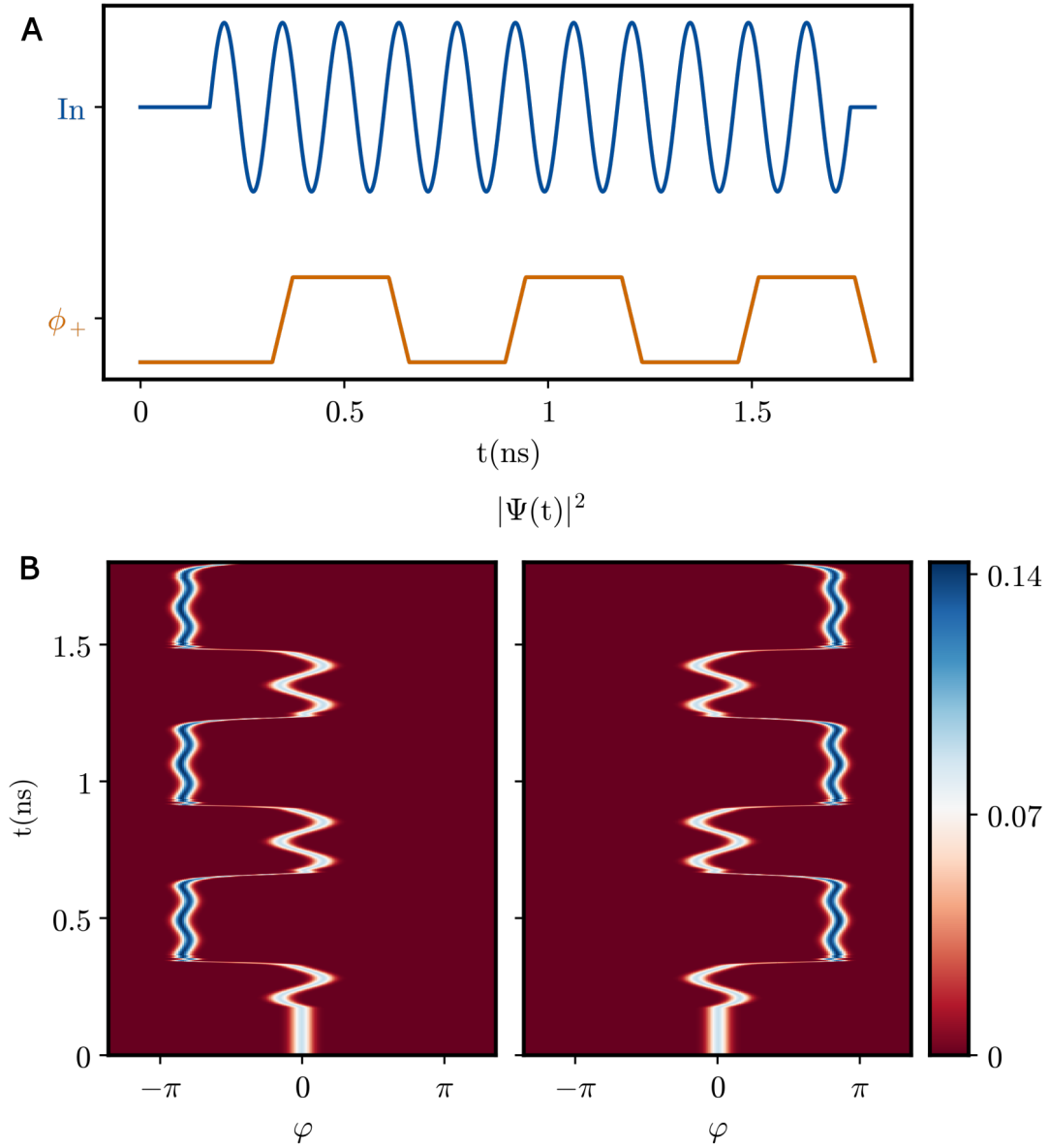


Figure 3.10: Multiple phase detections are performed on the same sinusoidal input tone. (A) Time diagram of the applied signals. The flux-switch curve is orange while the sinusoidal input tone is blue. (B) The time sequence reported in A has been simulated in QuTip and the $|\Psi(t)|^2$ is shown. In particular, in the left panel, the sinusoidal input tone is initialized with displacement $\theta_0 = 0$ while in the right one $\theta_0 = \pi$

Chapter 4

JDPD chip design

In this Chapter, I will discuss the JDPD chip layouts that I have designed during my PhD, with the support of SEEQC researchers. These chip layouts belong to three different generations, namely layout v1, layout v2 and layout v3.

With the first generation of devices, we have preliminarily investigated the main properties of the JDPD approach. In this layout, the JDPD was coupled to a 50Ω coplanar waveguide (CPW) resonator and to different lines opportunely designed to provide the fluxes ϕ_+ and ϕ_- . We have detected the JDPD state measuring the resonance frequency of the system, which shifts depending on the flux state. However, as discussed further in this Chapter, the intrinsic limitation in this first design release does not give us the opportunity to investigate phase detection at frequencies in the microwave regime.

A significant improvement has been obtained with the second generation of devices, in which the CPW resonator has been replaced with a more compact RLC-lumped resonator. In this way, digital phase detection has been validated at a frequency up to 960 MHz , with a remarkable agreement between simulations and experimental outcomes.

The configuration proposed in layout v2 has been employed as a base for layout v3, in which we have coupled the JDPD with an SFQ comparator and an SFQ flux driver with the main goal to demonstrate the compatibility between our detector and the SFQ circuitry.

While devices from release v1 and v2 have been experimentally characterized, circuits from layout v3 will be measured in the next future. The three different generations of devices have been fabricated by the SEEQC [145] foundry in the US. Their process involves a multilayer stack of superconducting wires that it's ideal to fabricate complex structures, as in the case of JDPD. A sketch of the layers used for the realization of the JDPD can be found in Fig. 4.1; more details on the SEEQC fabrication process can be found in Ref. [145].

4.1 JDPD coupled to a CPW resonator

The JDPD micrograph is reported in Fig. 4.2 A together with its electrical diagram. The JDPD is composed of two RF-SQUIDs that share the inductive

| |
|----------------|
| <i>M3</i> |
| <i>I2</i> |
| <i>M2</i> |
| <i>A1</i> |
| <i>J1</i> |
| <i>I1</i> |
| <i>M1</i> |
| <i>I0</i> |
| <i>M0</i> |
| <i>IN1</i> |
| <i>MN1</i> |
| <i>Silicon</i> |

Figure 4.1: Sketch of the multilayer process adopted by SEEQC [145]. The superconducting layers (MN1, M0, etc) are indicated with the initial M. Between each of them there is a dielectric layer in SiO_2 indicated by the letter *I*. Superconducting wires are realized in Nb with the exception of MN1, which is in NbN_x . Junctions are realized with a trilayer structure in $Nb/AlO_x/Nb$ with a critical current density of $1kA/cm^2$.

load L . This inductor has been realized by a $40 \mu m$ long and wide $1.4 \mu m$ wire fabricated using the high-kinetic inductance layer MN1, with a total value of $L = 220 pH$. The rest of the circuit is made with the layers M1 and M2 in Nb , characterized by smaller values of sheet inductance. We have fabricated the JDPD in different configurations with several values of critical currents ranging from $2.4 \mu A$ to $5.4 \mu A$, to explore the effect of the β factor on the device dynamics.

The JDPD has two degrees of freedom, ϕ_+ and ϕ_- , that allow the potential to assume different shapes. Our detection protocol exploits this tunability and so it's fundamental to have precise control of the fluxes that thread the two JDPD loops. Our device is coupled with two dc lines, Dc_1 and Dc_2 , and an *RF line* as shown in Fig. 4.2. The *RF line* is designed in layer M0 and goes below the JDPD loop. Given its geometry, it can be employed to provide ϕ_+ as total flux contribution. Intuitively, the different Sections of this line provide opposite contributions to the current flowing in L , and thus, the total amount of $I_L = 0$.

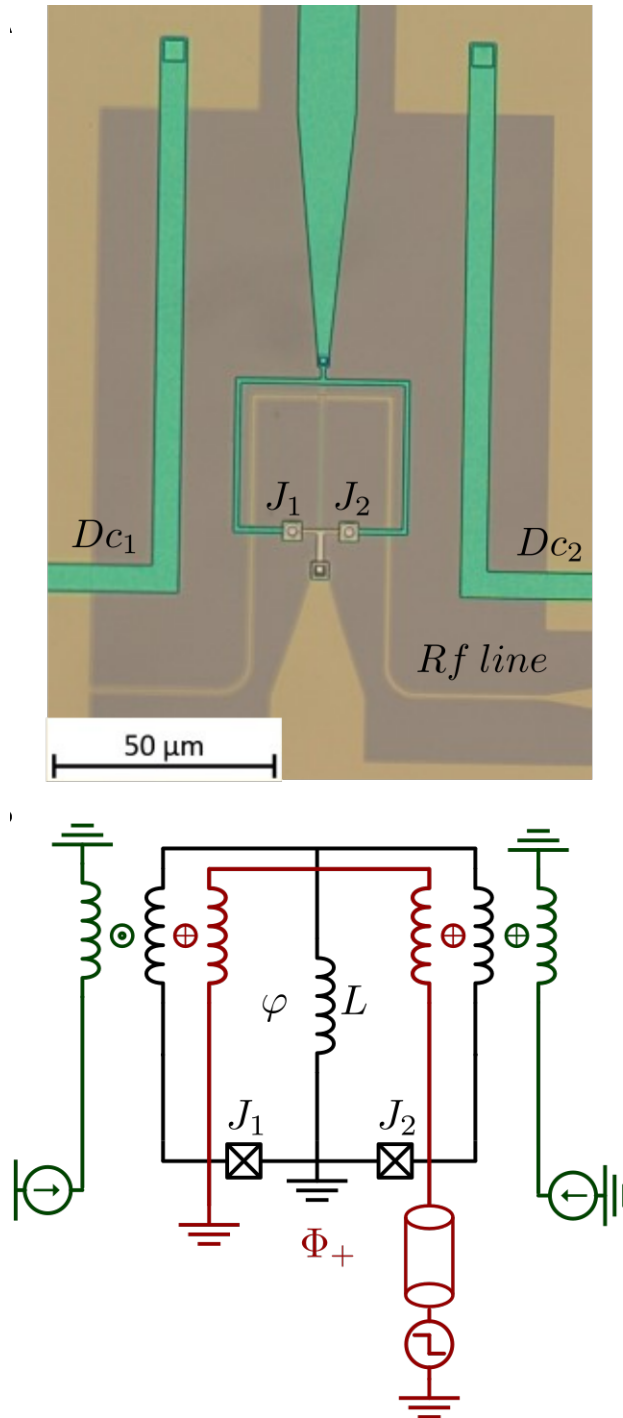


Figure 4.2: (A) JDPD micrograph in layout v1 and (B) it's electrical equivalent schematic. The JDPD is composed of two RF-SQUIDS that share the inductive load L . This inductor has been realized by a $40\mu\text{m}$ long and wide $1.4\mu\text{m}$ wire fabricated using the high-kinetic inductance layer MN1, which allows having $L = 220\text{pH}$ in a small portion of space. The rest of the circuit is made with layers M1 and M2 in Nb, characterized by smaller values of sheet inductance. We have placed different JDPD layouts on the chip with different values of the JJs critical current ranging from $2.4 \mu\text{A}$ to $5.4 \mu\text{A}$. To control the JDPD, two dc lines, Dc_1 and Dc_2 , and an RF line are coupled to our detector to provide ϕ_+ and ϕ_-

Since:

$$\varphi \frac{\Phi_0}{2\pi} = LI_L \quad (4.1)$$

it means that $\varphi = 0$ which leads to $\phi_- = 0$, according to Eqs. 1.11.

Conversely, the application of a current in the RF line generates a current circulating around the L branch and passing through the two junctions, coinciding with the application of an effective flux ϕ_+ . As discussed in the previous Chapter, the flux ϕ_+ allows us to set and reset the JDPD, flipping the potential from a single well configuration to a double well one and vice-versa. This operation should be performed diabatically to obtain high fidelity. For this reason, we connected the *RF line* below the JDPD loop to a conventional 50Ω Coplanar Waveguide (CPW) to preserve as much as possible the shape of the flux-switch. The CPW is made of an $11 \mu m$ width layer in M0 and it has a gap of $7 \mu m$. The mutual coupling to JDPD is estimated to be $M = 25 pH$, according to InductEx simulations.

The two dc lines provide individually a contribution in both the JDPD meshes. To be more clear, defining I_{DC1} and I_{DC2} the currents flowing respectively in the lines $DC1$ and $DC2$, we have:

$$\begin{aligned} \phi_1 \frac{\Phi_0}{2\pi} &= M_{1,1} I_{DC1} + M_{1,2} I_{DC2} \\ \phi_2 \frac{\Phi_0}{2\pi} &= M_{2,1} I_{DC1} + M_{2,2} I_{DC2} \end{aligned} \quad (4.2)$$

where $M_{i,j}$ is the mutual inductance between the dc line j and the mesh i . As shown in Fig. 4.2, the two dc lines are placed on the opposite side with respect to the central inductor L , which indicates that the matrix of coefficients $M_{i,j}$ is symmetric:

$$\begin{aligned} M_{1,1} &= M_{2,2} = M_{dir} \\ M_{1,2} &= M_{2,1} = M_{opp} \end{aligned} \quad (4.3)$$

According to Eqs. 4.3, any combination of ϕ_+ and ϕ_- can be generated by properly biasing the two dc lines. Cases of particular interest occurs when $\phi_+ = 0$, which implies $I_{DC1} = -I_{DC2}$:

$$\begin{aligned} 0 &= \frac{\phi_1 + \phi_2}{2} \frac{\Phi_0}{2\pi} = \frac{M_{dir}}{2} (I_{DC1} + I_{DC2}) + \frac{M_{opp}}{2} (I_{DC1} + I_{DC2}) \\ &\implies I_{DC1} = -I_{DC2} \end{aligned} \quad (4.4)$$

and when $\phi_- = 0$, leading to $I_{DC1} = I_{DC2}$:

$$\begin{aligned} 0 &= \frac{\phi_1 - \phi_2}{2} \frac{\Phi_0}{2\pi} = \frac{M_{dir}}{2} (I_{DC1} - I_{DC2}) + \frac{M_{opp}}{2} (I_{DC1} - I_{DC2}) \\ &\implies I_{DC1} = I_{DC2} \end{aligned} \quad (4.5)$$

The two dc lines are very useful to control the asymmetries of the system and to set the JDPD working point. The dc lines are designed in layer M1 and they

have a mutual inductance $M = 4pH$ with the JDPD.

The JDPD dynamics is investigated through spectroscopy measurements. To shift the resonance frequency in the measurable range $[4GHz, 8GHz]$, we couple the JDPD to a $\lambda/4$ CPW resonator, as reported in Fig. 4.3. In this configuration, the JDPD can be seen as a lumped inductance whose values depend on the applied magnetic fluxes ϕ_+ and ϕ_- . The resonator is then coupled to the external input line by an interdigitated capacitor $C_{coupling} = 10fF$, as shown in Fig. 4.3B. To design opportunely all the components on chip, we have simulated the system in Fig. 4.3 A with Qucs [157] and Ansys HFSS [158]. We have designed the resonator to have a length of $l = 4.25 mm$, that according to our simulations, corresponds to a bare resonance frequency:

$$\omega/2\pi = \frac{c_l}{4l} = 6.8 GHz \quad (4.6)$$

where c_l is the speed of light along the transmission line. This frequency has been chosen to be in a safe range to preserve the measurability of the device even in presence of fabrication spread that could shift the desired resonance frequency. Moreover, the simulations performed in QUCS and HFSS do not allow us to simulate the superconducting nature of the circuit and thus some slight difference may be observed between the numerical prediction and the experimental outcomes. This first release has allowed us to experimentally verify the main feature of the JDPD detection technique. As discussed in Chapter 5, we were able to demonstrate the presence of a tunable potential, which can be opportunely controlled to trap the phase particle when an input tone at MHz is provided throughout the dc lines. However, despite the remarkable agreement between experimental outcomes and simulations, the employment of a CPW resonator in series to the JDPD, which works as a bandpass filter, did not give us the opportunity to send tones through the input line and thus investigate the phase detection at frequencies around 1 GHz, where typical superconducting resonators works.

4.2 JDPD coupled to a lumped RLC resonator

Layout v2 has been elaborated with the main purpose to demonstrate phase detection with signals in the microwave regime. These tones should be delivered through the input line, to mimic the future connection to the qubit resonator, according to the schematic in Fig. 3.9. Therefore, the circuitry components should be carefully evaluated to allow the delivery of the input signals without compromising the possibility to measure the device in reflection.

In layout v2, the CPW resonator has been replaced with a lumped LC resonator, as shown in Fig 4.5. In this way, we have not only simplified the whole circuit but we reduced the physical footprint of the components on chip. As reported in Fig 4.5, the circuit comprises an inductor L_S in series to the JDPD and a parallel plate capacitor $C_{//}$ close to the ground. A coupling capacitor $C_{coupling}$

4.2. JDPD COUPLED TO A LUMPED RLC RESONATOR

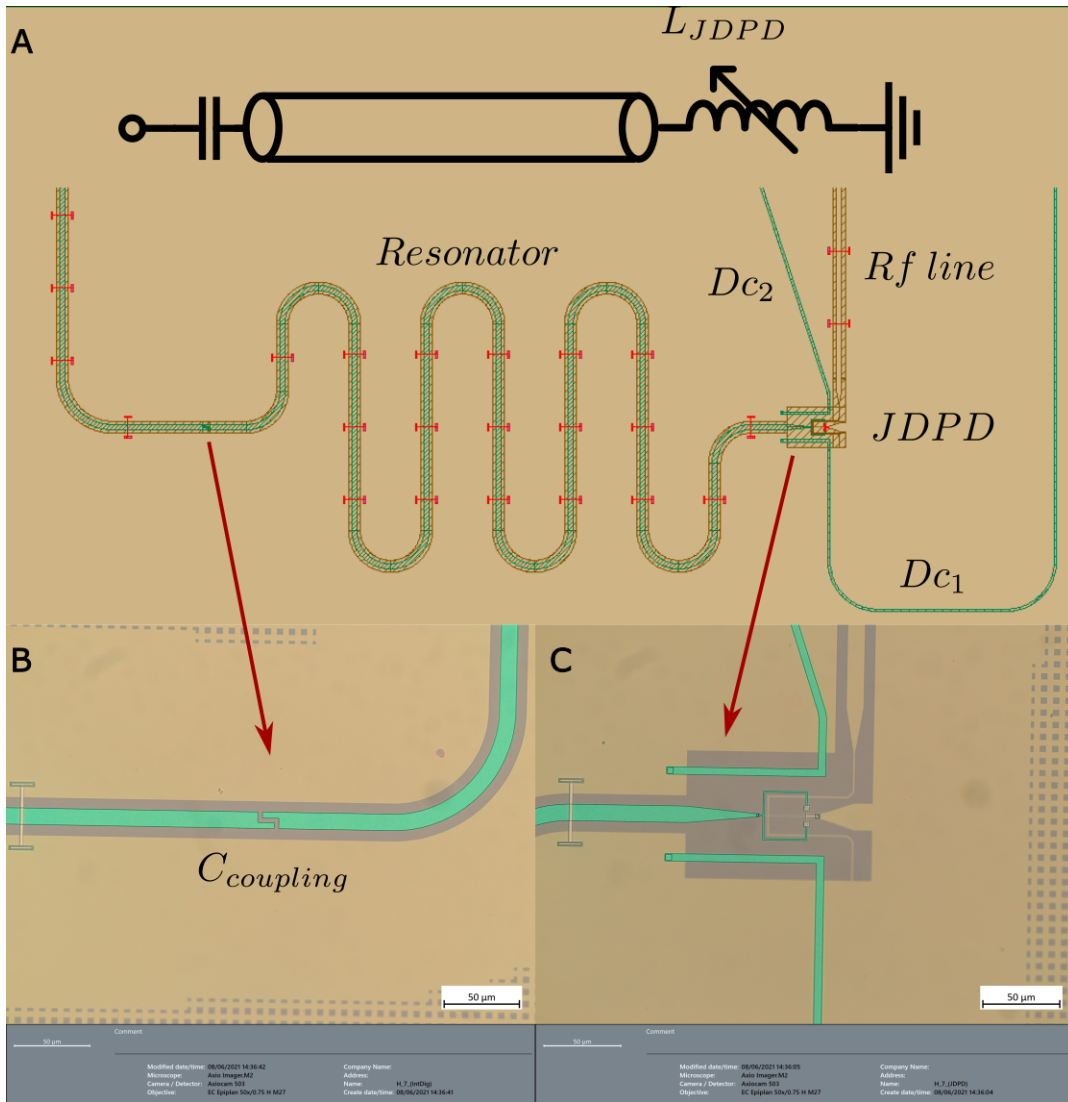


Figure 4.3: (A) JDPD Layout v1. The JDPD is coupled to a $\lambda/4$ resonator that brings its resonance frequency in the measurable range [4GHz, 8GHz]. (B) The resonator is coupled to the external instruments by an interdigitated capacitor $C_{coupling}$. (C) JDPD is placed at the end of the resonator and it behaves like a tunable inductor depending on the fluxes ϕ_+ and ϕ_-

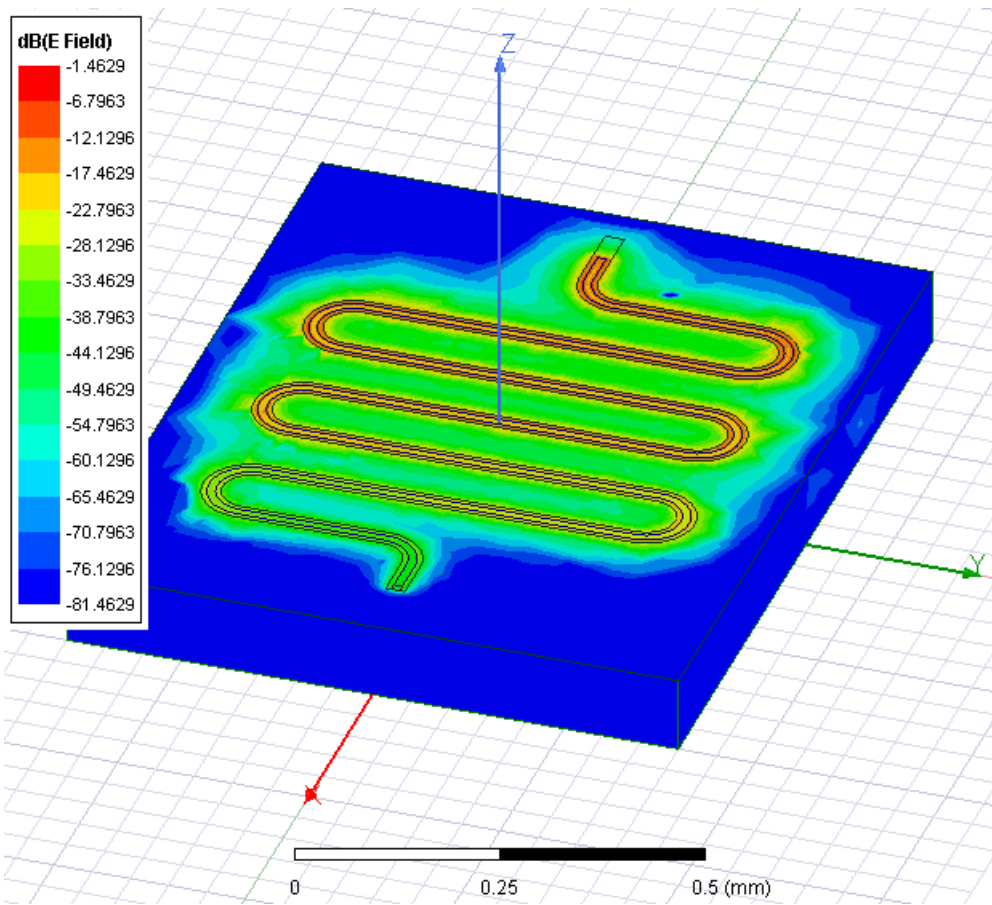


Figure 4.4: HFSS simulation of the circuit in Fig. 4.3 A. The plot shows the magnitude of the electric field along the CPW. The JDPD is represented as a lumped inductor with $L_{JDPD} = L$.

connects this resonator to the external experimental apparatus.

We have carefully determined the values of L_S , $C_{coupling}$ and $C_{//}$ considering some experimental constraints:

- **Resonance visibility:** As in the case of layout v1, the chosen way to analyse the JDPD dynamics is based on spectroscopy measurements. The JDPD works as a tunable inductor that changes the measured resonance frequency depending on the values of ϕ_+ and ϕ_- . L_S , $C_{coupling}$ and $C_{//}$ should be opportunely selected to be in the range of frequencies, $[4GHz, 8GHz]$ that can be measured with our experimental electronics. Moreover, we have to consider possible variations of the desired values that come from the fabrication spread.
- **Possibility to drive the JDPD off resonance:** The main goal of this release is to demonstrate the phase detection with tones around $1 GHz$ delivered through the input line. This scheme is similar to the one that can be adopted in the future when a superconducting qubit will be coupled to the JDPD.

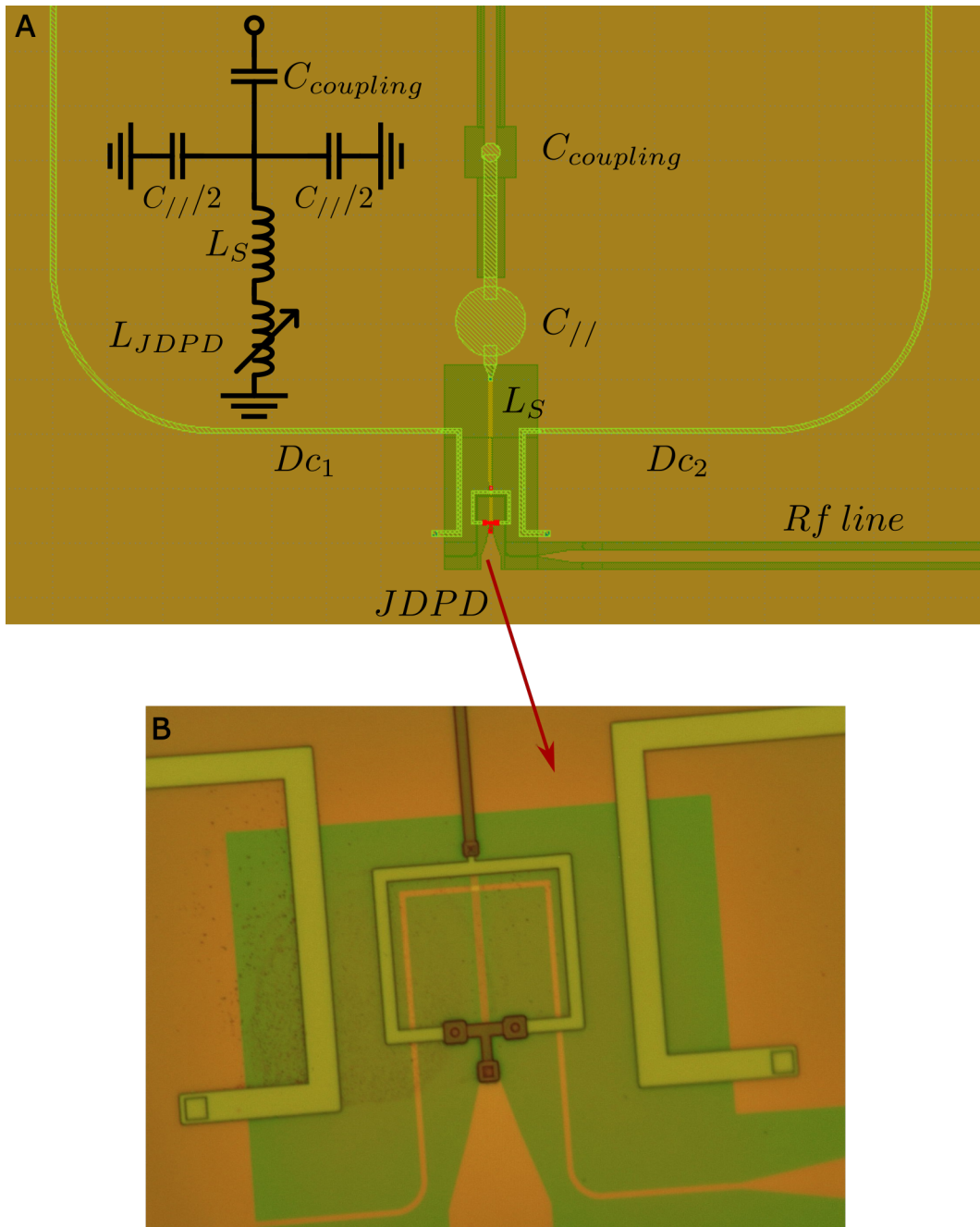


Figure 4.5: (A) JDPD layout v2. The circuit comprises an inductor L_S in series to the JDPD and a parallel plate capacitor $C_{||}$ close to the ground. A coupling capacitor $C_{coupling}$ connects this resonator to the external experimental apparatus. (B) JDPD Micrograph in layout v2.

One key feature of our technique is to work off-resonance with respect to the input; in particular, the JDPD is designed to have a higher resonance frequency to minimize the backaction, as discussed in Chapter 3. It's important to determine precisely $C_{coupling}$, which should be smaller enough to allow the passage of signal while preserving the resonance visibility.

These constraints lead us to choose $L_S = 300 \text{ pH}$, $C_{coupling} = 100 \text{ fF}$ and $C_{//} = 1.4 \text{ pF}$, determined in agreement with numerical simulation in Qucs [157] and Sonnet [159]. In terms of resonance frequency, these values correspond to:

$$\omega/2\pi = \frac{1}{\sqrt{(C_c + C_{//})(L_{JDPD} + L_s)}} \in [5.5\text{GHz}, 7.2\text{GHz}]. \quad (4.7)$$

We have also estimated a total quality factor $Q = 100$, which guarantees sufficient visibility and allows us to provide the input stimulus out of resonance.

The capacitors $C_{coupling}$ and $C_{//}$ have been realized in a parallel plate configuration between the layers $M0$ and $M1$. As schematically shown in Fig. 4.6, these $M0$ and $M1$ are separated by a dielectric layer in SiO_2 with a specific capacitance of $0.44 \text{ fF}/\mu\text{m}^2$. This choice is necessary since it's not possible to achieve large values of capacitance with interdigitated capacitors, as required in our circuit. The drawback is that these capacitors lead to higher values of the circuit internal losses [79, 80] and they are more prone to manufacture parameters spread. The inductor L_s is realized using the high kinetic inductance layer MN1, which brings to a large value of L_s in a relatively small portion of space. In contrast to RF linear part, the JDPD design is not overturned with respect to the previous release and only small modifications have been applied. As shown in Fig. 4.5, the presence of a more compact resonator part permits us to place the two dc lines symmetrically with respect to JDPD. We have also reduced the distance between the JDPD and these lines to increase their mutual inductance. Finally, we have increased the width of the M1 wires in series to the JDPD's JJs, to reduce their inductance contribution.

With this layout release, we have observed a considerable improvement in resonance visibility. As discussed in Chapter 5, with this configuration we have demonstrated the digital phase detection up to 960 MHz , which it's very significant for the feasibility of this approach applied to superconducting qubit readout.

4.3 Towards a scalable platform: JDPD-SFQ architecture

Layouts v1 and v2 have allowed us to explore the main characteristics of the JDPD approach. To simplify the experimental characterization, the JDPD was controlled and readout by means of RF signals generated and processed at Room Temperature (RT). However, one of the JDPD's key features is its compatibility with SFQ circuitry, which can be employed to perform all the operations required

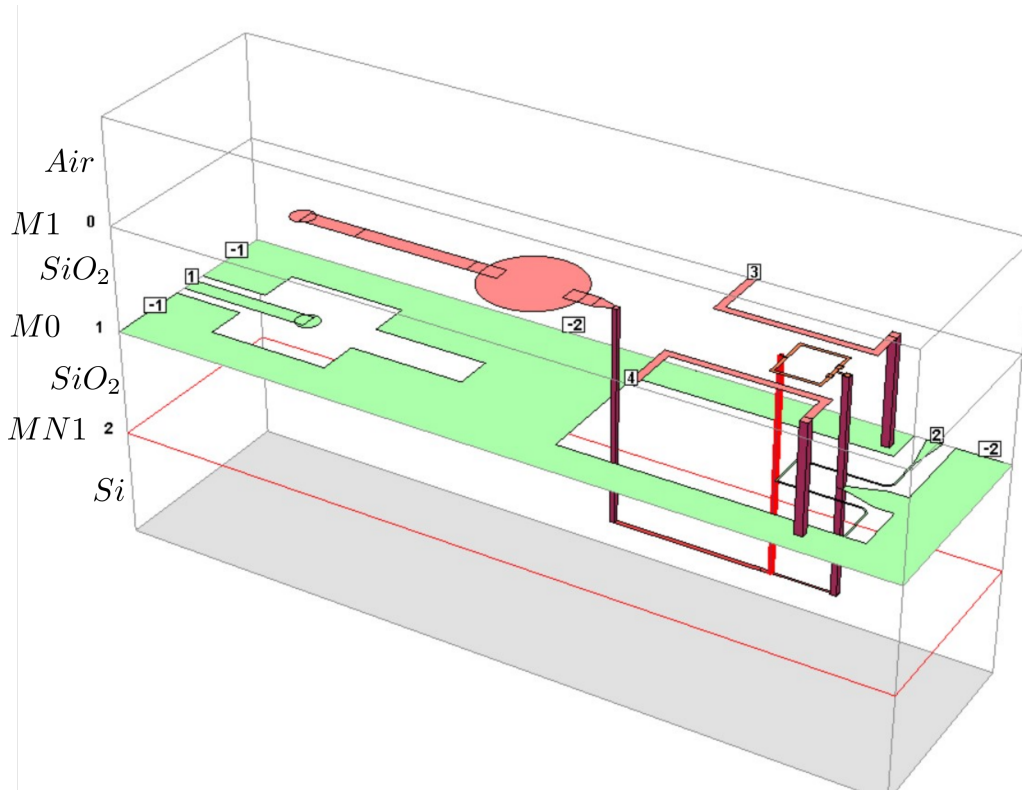


Figure 4.6: Layout v2 imported in Sonnet. Each layer has been simulated according to characteristics reported in the SEEQC design rules [145].

during the detection. SFQ devices have been indicated as a possible solution to enhance the scalability of a quantum chip since they can operate inside the fridge with small requirements in terms of connection to the RT apparatus.

Design v3 has been realized to investigate the JDPD compatibility with an SFQ Comparator and SFQ flux generator, employed respectively to readout and set the device state.

4.3.1 SFQ Comparator coupled to JDPD

As for the JPM case, the JDPD stores the information on the qubit state in the direction of the circulating current through the JDPD central inductor L . Hence, an SFQ comparator, similar to the one adopted in Ref. [93], is suitable to convert the JDPD output in SFQ fluxons [109, 111, 112, 160].

As discussed in Chapter 2, the SFQ comparator consists of two identical junctions that operate as a decision-making pair. Both junctions are biased close to their critical currents, and the signal to be compared is injected between them. This current biases one of the junctions closer to its critical current than the other, and, consequently, it switches when a pulse is applied across the comparator. The switched junction determines the passage of the SFQ pulse to the output. In the case of the JDPD SFQ readout, the current to be compared originates from the flux transformation between the JDPD central inductor L and $L_{coupling}$.

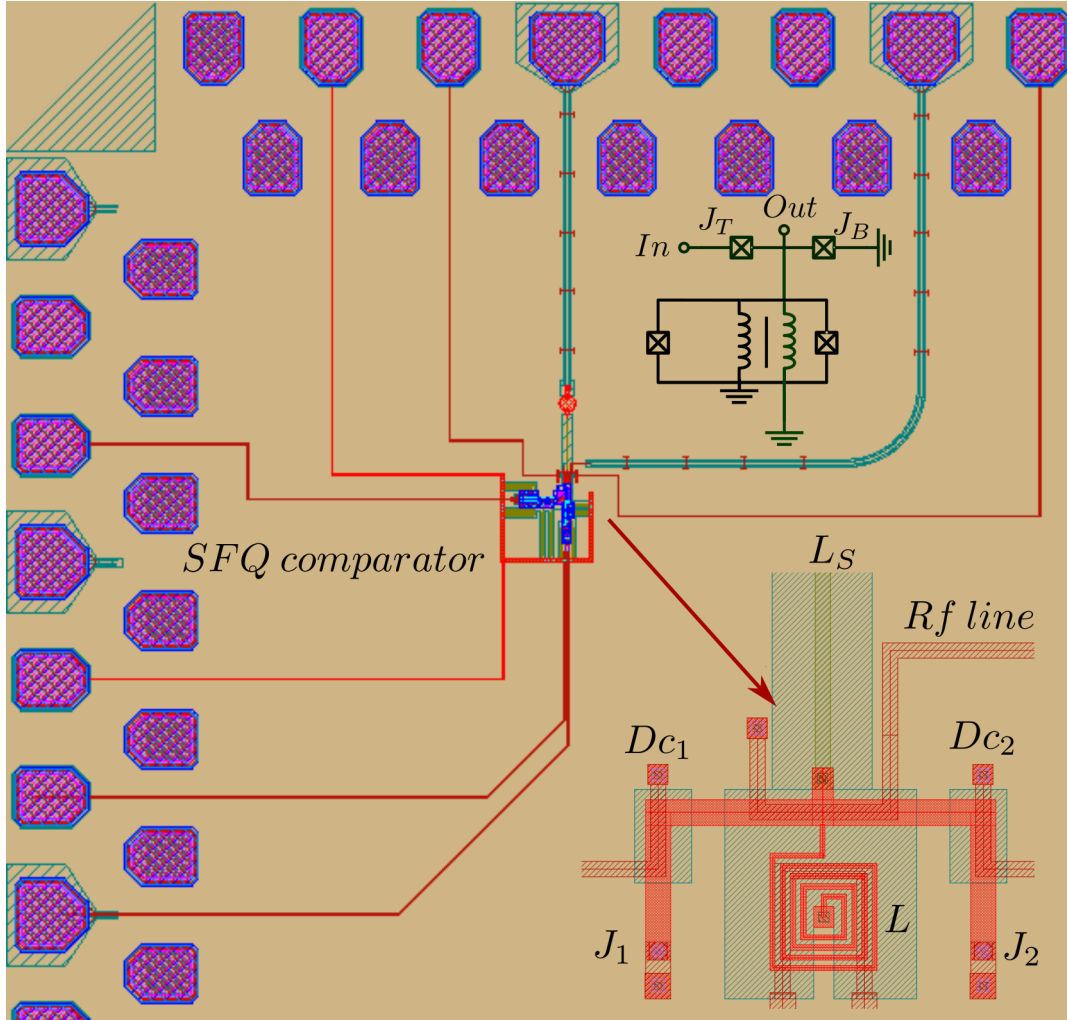


Figure 4.7: Circuit design of the JDPD coupled to the comparator. The SFQ comparator consists of two identical junctions that operate as a decision-making pair. Both junctions are biased close to their critical currents, and the signal to be compared is injected between them. This current biases one of the junctions closer to its critical current than the other, and, consequently, it switches when a pulse is applied across the comparator. The switched junction determines the passage of the SFQ pulse to the output. In the case of the JDPD SFQ readout, the current to be compared originates from the flux transformation between the JDPD central inductor L and $L_{coupling}$. The JDPD shows a similar configuration to Fig. 4.5. We have replaced the wire in MN1 with a meander structure fabricated in M2 to maximize flux transformation.

To provide a sufficient level of coupling between L and $L_{coupling}$, we have replaced the wire in MN1 with a meander structure fabricated in M2. This modification led to a substantial change in other elements composing the JDPD, as shown in Fig. 4.7. As a major modification, the fast-flux line goes now over the JDPD loop, and the two dc lines, overlap the JDPD branch before closing to ground. In both cases, these lines are produced in layer M1.

The JDPD input is connected to the lumped RLC resonator, already adopted in layout v2, to provide the input tone that mimics the output signal coming from the qubit. This resonator gives us another way to probe the JDPD state, in order to compare the SFQ and the microwave detection approaches and simplify the experimental characterization of this circuit.

The circuit parameters have been carefully determined from numerical simulations in InductEx. We want that the SFQ readout of the JDPD state can be exploited even in the presence of a 30% spread of the circuit's desired parameters, with a negligible backaction on the system. It's also desirable to achieve the JDPD detection in a nanosecond time scale. Considering these constraints, we have estimated $L = 320 \text{ pH}$, $L_{coupling} = 40 \text{ pH}$ and $M = 60 \text{ pH}$, which lead to a $\beta = 10$ considering junctions with $I_c = 5.4 \text{ }\mu\text{A}$.

The full circuit has been also simulated in PSCAN2, as reported in Fig 4.8. In a similar way to what has been done in the previous Chapter, we provide at the input node of the JDPD a signal with frequency $\omega/2\pi = 4.5 \text{ GHz}$ and gaussian envelope. When this pulse reaches its maximum, we apply a flux switch which traps the phase particle in one of the two JDPD wells. In particular, in the case of the first sequence part of Fig. 4.8, the phase particle collapses in the right state, leading to a current $I_L \simeq 3 \text{ }\mu\text{A}$ circulating through the central inductor. At this point, we clock the SFQ comparator with a sequence of 12 pulses. Because $I_L > 0$, J_b does not switch and no output pulses are produced.

Different is the case of the second stimulus pulse reported in Fig. 4.8. Having an opposite initial phase, this signal makes the phase particle fall in the left well, corresponding to a negative current circulating through L . The clock pulses sent to the SFQ comparator lead to a switch of J_T , which ultimately triggers the production of SFQ output pulses.

According to this simulation, the detection technique is non-destructive, since the phase particle position is preserved. This allows us to probe the system multiple times and average the results to enhance the fidelity of the measurement.

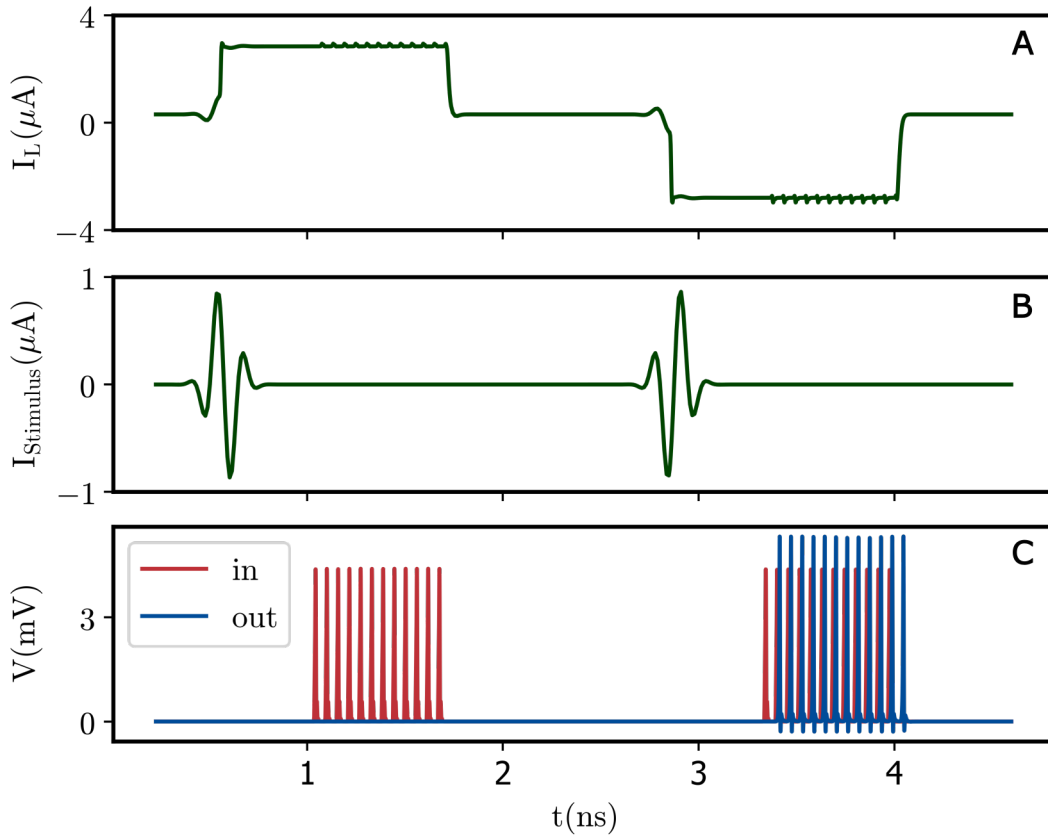


Figure 4.8: PSCAN2 simulation of the SFQ Comparator coupled to the JDPD. In panel (A),(B) and (C) are reported the time evolution of the current flowing through the JDPD central inductor (I_L), the signal stimulus ($I_{Stimulus}$) and comparator input/output SFQ voltage pulses, respectively. Simulations have been carried out providing, at the input node of the JDPD, a sinusoidal signal with frequency $\omega/2\pi = 4.5 \text{ GHz}$ with a gaussian envelope. When the stimulus signal reaches its maximum, a flux switch is applied that traps the phase particle in one of the two JDPD wells. The sequence has been repeated considering two opposite values of the input tone phase displacement. In particular, in the case of the first part of the sequence, the phase particle collapses in the right state, which leads to $I_L \simeq 3 \mu\text{A}$, as shown in panel (A). At this point, we clock the SFQ comparator with a sequence of 12 pulses. Because $I_L > 0$, J_b does not switch and no output pulses are produced, as illustrated in panel C.

In the second part of the sequence, a stimulus signal having an opposite initial phase makes the phase particle fall in the left well, corresponding to a negative current through L . The clock pulses sent to the SFQ comparator lead to a switch of J_T , which ultimately triggers the production of SFQ output pulses, shown in panel C.

According to this simulation, this detection technique is non-destructive, since the phase particle position is preserved. In this way, we can probe the system multiple times and average the results to enhance the fidelity. For example, in the case of this simulation, the JDPD readout has been performed 12 times for each stimulus signal.

4.3.2 SFQ Flux generator coupled to JDPD

The JDPD should be flux-switched very quickly to achieve fast high-fidelity measurements. An SFQ flux generator is ideal to perform this task. Clocked at very high frequencies, it can generate ramp signals with a rise time of the order of tens of picoseconds or less.

The SFQ flux generator is basically composed of a big inductor L_{flux} , that is part of a quantized superconducting loop that can store more than Φ_0 [16, 48]. When an SFQ pulse is injected inside this loop, the current flowing through L_{flux} is increased by the quantity:

$$\Delta I = \Phi_0 / L_{flux} \quad (4.8)$$

One can also reduce the current in the loop by providing an SFQ pulse in the opposite direction, as indicated by the blue arrow in Fig. 4.9 A.

SFQ flux generator can produce a mutual magnetic field in an adjacent device. In the specific case of the JDPD, we have coupled L_{flux} to the JDPD branches in series to the two JJs, in order to provide correctly ϕ_+ . However, since the current can assume discrete values, according to equation 4.8, precise calibration of the circuit parameters is required.

In our layout, the SFQ flux generator is designed to provide $4 \Phi_0 / L_{flux}$ of flux, which corresponds to 400 ps of rise time if the circuit is clocked at 20 GHz. This means that the JDPD readout can be accomplished in a time scale of a few ns, as shown in Fig. 4.10. As in the case of the SFQ comparator, the parameters L_{flux} and the mutual inductance M have been determined by performing simulations in PSCAN2 and InductEx. In particular, we have determined $L_{Flux} = 172 pH$ and $M = 13 pH$. The inductor L_{Flux} is composed of two long wires in M2 and M1 completely overlapped as shown in Fig. 4.9 B. These wires are placed in between an upper and lower ground plane, in M0 and M3 respectively, in order to minimize the flux noise. With respect to layer MN1, layers M2 and M1 have a modest value of sheet inductance ($0.4 pH/\square$) and thus L_{Flux} has a considerable size compared to JDPD central inductor L . However, wires fabricated in M2 and M1 are less prone to fabrication spread, allowing us to have more precise control of the effective magnetic flux generated by the SFQ flux controller.

In layout v3, we kept the same JDPD structure fabricated for layout v1 and v2, as reported in Fig. 4.9 B. The external branches comprising the JJs are fabricated in layer M1 while the central inductor is made in MN1. The detector is coupled to an RLC linear resonator, employed to readout the JDPD state and set the stimulus tone. A major modification regards the flux lines. L_{flux} , connected to the SFQ flux generator, plays the role of RF line and sets and resets the JDPD in the single and double well configuration. The amount of flux that L_{flux} can generate is fixed by design and it's important to have additional lines to provide ϕ_+ and ϕ_- , even diabatically. For this reason, we have equipped the JDPD with two auxiliary RF lines, that play the role of the dc lines used in the previous layouts v1 and v2.

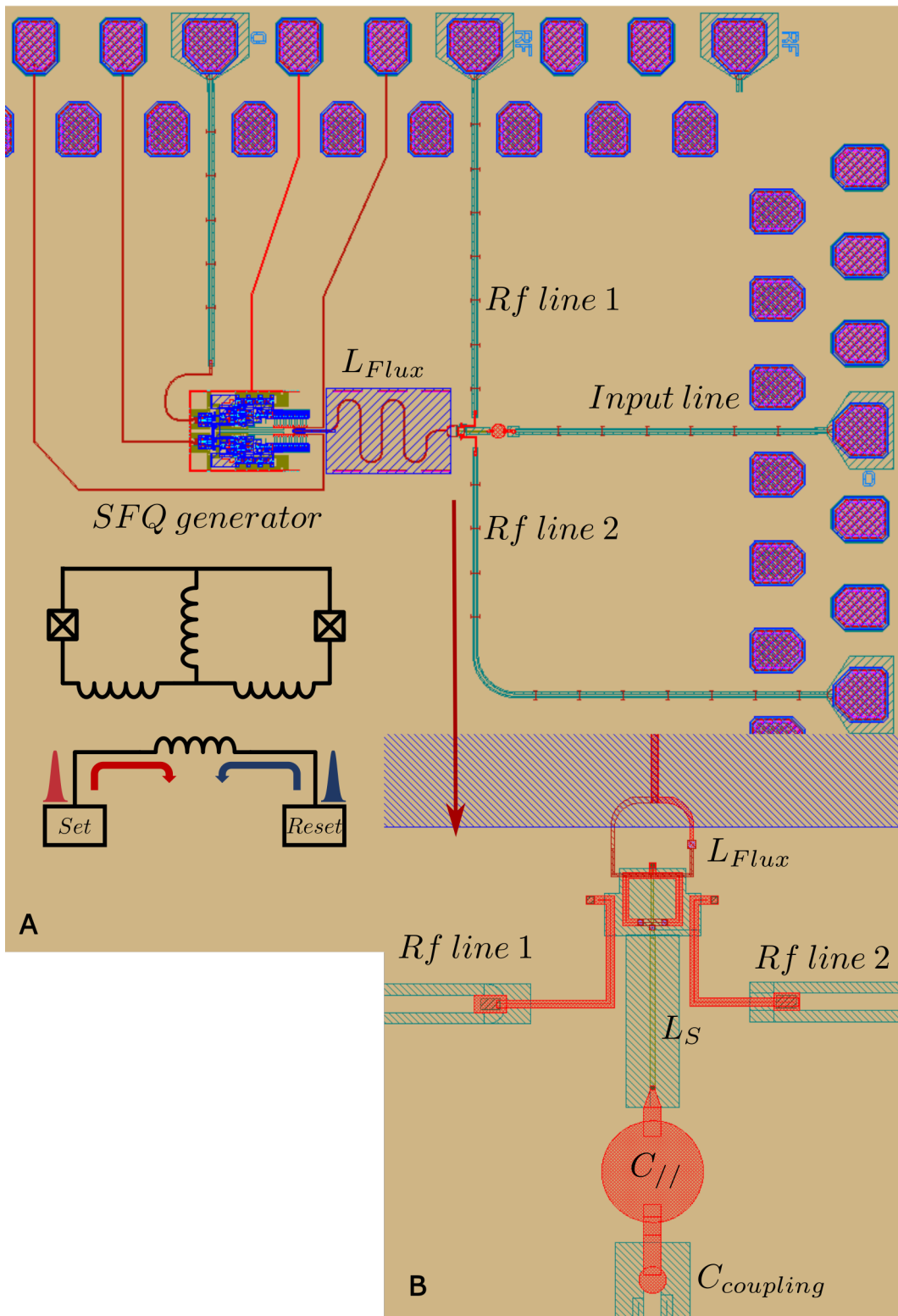


Figure 4.9: (A) Circuit design of the JDPD coupled to the SFQ flux generator. The SFQ flux generator consists of a big inductor L_{flux} that stores one or more flux quanta Φ_0 . When an SFQ pulse is injected inside this loop, the current flowing through L_{flux} provides a flux bias to a mutually coupled JDPD. (B) Zoom on the JDPD circuit

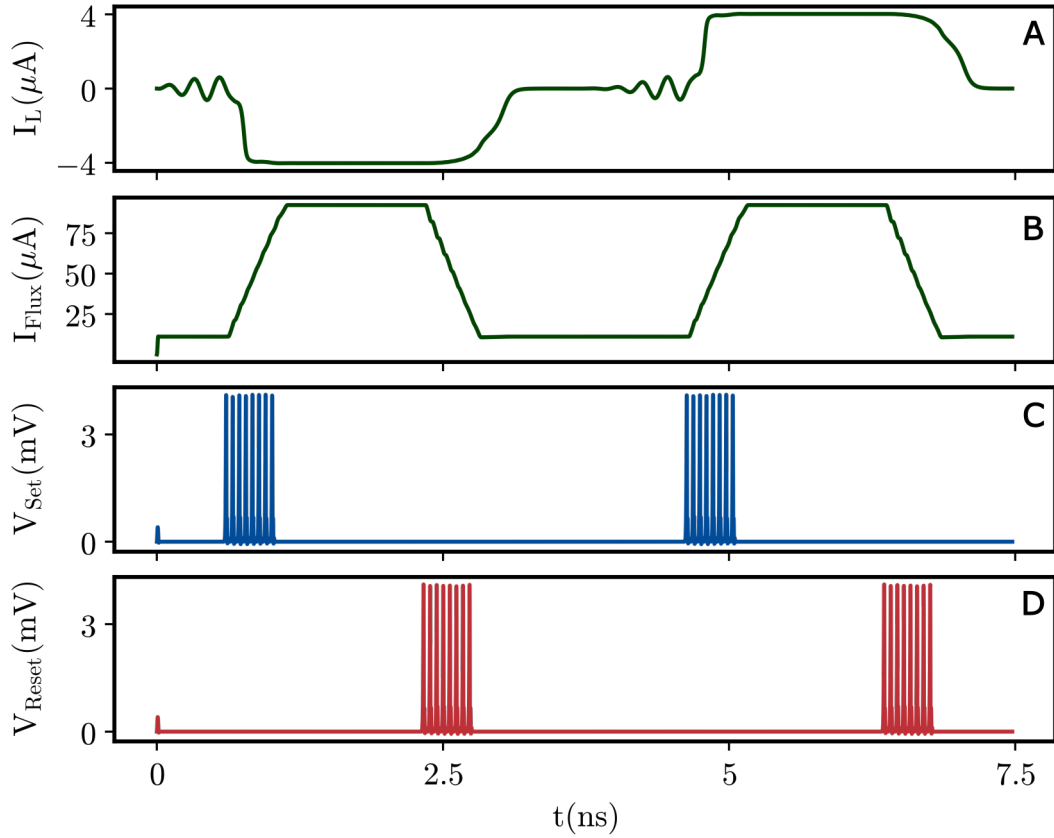


Figure 4.10: PSCAN2 simulation of the SFQ Flux generator coupled to the JDPD. The set and reset of the JDPD state are performed by means of SFQ pulses that increase or decrease the current in L_{Flux} , according to Eq. 4.8. Panel A reports the time evolution of the current I_L circulating through the JDPD central inductor L . I_{Flux} , originating from the SFQ Flux generator, is shown in panel B. Time evolution of SFQ pulses to set and reset I_{Flux} are plotted in panels C and D respectively.

Chapter 5

Measurements and Data Analysis

On the basis of the designs and simulations illustrated in the previous Chapters, the various JDPD 's layouts have been fabricated by SEEQC [145] in their facilities in the United States. After some quality tests, the samples have been sent to our lab in Naples for a complete experimental characterization at 10 mK.

In this Chapter, I will discuss the experimental outcomes and the methodology adopted to demonstrate JDPD's capability to perform digital phase detection. In particular, Sections 5.1 and 5.2, are dedicated to the description of the experimental technique and the experimental setup.

In Section 5.3 I will describe the spectroscopy measurements, performed by changing the external fluxes ϕ_+ and ϕ_- , which allows us to map the locations of the different bias points to the potential energy configurations. The latter step is only a necessary condition towards the functioning of the JDPD's read-out protocol because it is related to its capability of confining the phase particle in one of its two wells. To demonstrate that, a specific experimental protocol has been elaborated in Section 5.4 which exploits both ϕ_+ and ϕ_- to manipulate the JDPD potential energy. This flux sequence leads the system to show a hysteretic behaviour that is the direct consequence of the presence of a double well potential [79].

In Section 5.6, we discuss the procedure to calibrate the JDPD in order to achieve state-independent fidelity. Finally, we have verified the JDPD's capability to perform digital phase detection in Section 5.7. This step has been accomplished for several input stimulus amplitudes and frequencies, with consistent results. All these experiments have been carried out for several devices from release v1 and v2, which gave similar outcomes. This demonstrates the robustness of the whole approach of the digital phase detection readout.

5.1 Experimental technique

The chosen way to analyse the JDPD dynamics is based on the study of the transmissivity and the reflectivity of electromagnetic signals sent in input to a circuit that contains the JDPD.

The first feature to notice is that, in a good approximation, the JDPD is made

up of only inductive components. Neglecting the capacitance of the Josephson junctions, the JDPD can be represented as a single inductor, L_{JDPD} , equal to the equivalent inductance of the whole device, which depends on ϕ_+ and ϕ_- . L_{JDPD} can be calculated starting from the equation 3.3 that links the inductance to the concavity of the well where the phase particle is trapped [41, 42]:

$$L_{JDPD} = \left(\frac{\Phi_0}{2\pi}\right)^2 \left[\frac{d^2U}{d\varphi^2}\right]_{\varphi=\varphi_{Phase\ particle}}^{-1} \quad (5.1)$$

The system is thus characterised by a resonance frequency according to:

$$\omega_R/2\pi = \frac{1}{\sqrt{(C_c + C_i)(L_{JDPD} + L_i)}} \quad (5.2)$$

where C_c is the coupling capacitance, while L_i and C_i are the equivalent inductance L_R and capacitor C_R of the resonator in design v1 and $L_i = L_s$, $C_i = C_{\parallel}$ in design v2. Thus, the JDPD phase particle position can be traced to the potential energy curve by studying the spectroscopy of the circuit. According to Eqs. 5.1 and 5.2, a deeper well, corresponding to a smaller inductance L_{JDPD} , leads to a higher resonance frequency. As an example, in Fig 5.1 C. are reported the measured S parameters for two JDPD states corresponding to $\phi_+ = 0$ and $\phi_+ = \pi$. This technique is fundamental to the identification of the various JDPD states.

5.2 Experimental setup

In Fig. 5.2 is reported the experimental setup. The measurements have been performed at about 10 mK by using a dry dilution fridge Triton 400 from Oxford Instruments [161] and LD 400 from Blue Force [162]. The two fridges provide two sets of lines with specific filtering components dedicate to delivering DC and RF signals [161, 162]. The JDPD input is connected to room temperature (RT) instruments by one of the RF coaxial input lines. This line passes through a series of attenuators that reduce the signal power [40], as schematized in Fig. 5.2 A. The JDPD output signals go through an RF output line and travel through a cryogenic high electron mobility transistor (HEMT) amplifier produced by Low Noise Factory [163] before reaching RT. The RF input line and the RF output line are routed to port 1 and port 3 of a circulator, as indicated in Fig. 5.2. Port 2 is connected by a cryogenic coaxial line to the sample holder where our device is anchored.

To explore the dynamics of the JDPD, it is necessary to have control of the magnetic fluxes ϕ_+ and ϕ_- . As illustrated in the previous Chapters, the JDPD is coupled to two dc lines and fast flux lines (FFL), which serve to change the JDPD potential status. The two dc lines are connected to the RT instruments by the dc cables furnished in the fridges [161, 162], which show a resistance of

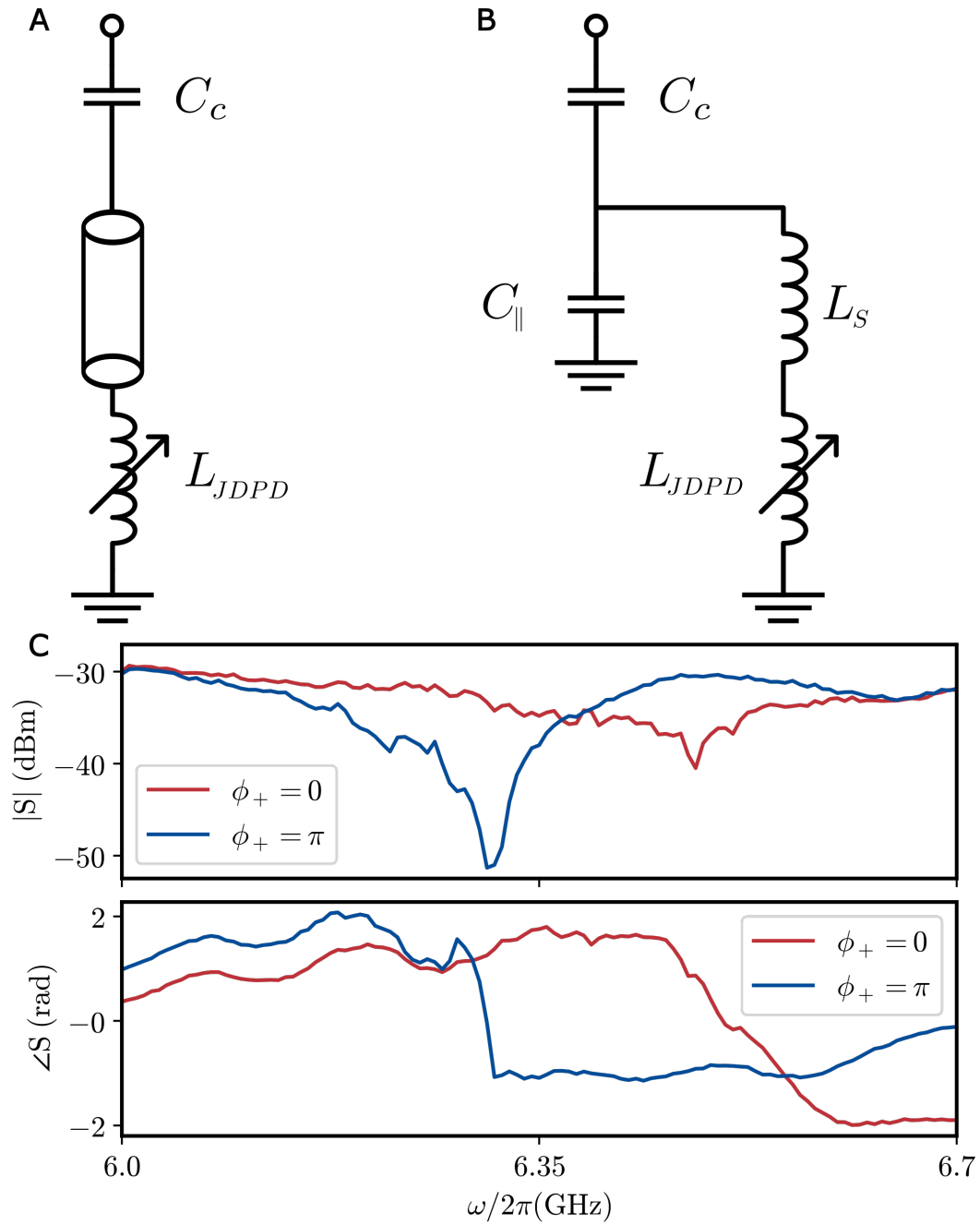


Figure 5.1: Schematic representation of the circuit measured in spectroscopy for design v1 (A) and design v2 (B). The JDPD is represented as a single inductor L_{JDPD} with a value that can be tuned changing ϕ_+ and ϕ_- . (C) For example, we reported the values of the S parameters vs frequency measured in amplitude ($|S|$) and phase ($\angle S$) for $\phi_+ = 0$ and $\phi_+ = \pi$

20 Ω when the cryostat reaches the base temperature. These lines are equipped by a low-pass RC filter with a cutoff frequency of $\omega_c/2\pi = 100$ MHz. The FFL is connected to another RF input line, in order to preserve the shape of the flux switch that has a rise time of 1 ns. Concerning the one used for the JDPD input, we removed the -20 dBm attenuator at the MXC to ensure that the room temperature AWGs are able to provide enough current to change the JDPD's state.

The fact that the FFL is connected to another RF input line gives us another way to probe the JDPD's state. As shown in Fig. 5.2 B, one can perform the heterodyne detection by sending signals through the FFL and measuring the transmitted pulse through the output line, since FFL is strongly coupled to the device. Simultaneously, one can still change the flux ϕ_+ using a bias tee, as shown in Fig. 5.2 B. The latter experimental setup has been mainly employed to characterize the JDPD's devices from release v1, where we have observed issues in reflection measurements.

The electronic setup used to measure the JDPD is composed of numerous instruments operating at room temperature and serving a variety of functions. The detector readout tone is generated through sideband mixing of shaped intermediate frequency (IF) and local oscillator (LO) tones. To produce the IF waveforms we have adopted 1 GS/s arbitrary waveform generators (AWGs). These IF waveforms are sent to the in-phase (I) and quadrature (Q) ports of an IQ mixer and are mixed with an LO to generate pulses at microwave frequencies at the output port. Similarly, the output readout signal is sent to the RF port of an IQ mixer where it is down-converted using the shared LO with the input readout AWG. Baseband I and Q signals are digitized using a 500 MS/s analog-to-digital converter (ADC). The fluxes ϕ_+ and ϕ_- are supplied by AWGs with similar characteristics to the ones described above. In this way, we can provide a flux switch with a rise time of 1 GS/s and explore the device dynamics in the diabatic regime. For measurements where precise control of the signal timing is not required, we have sometimes adopted a Vector Network Analyzer (VNA) to detect the resonance frequency associated with the JDPD's state.

5.3 Spectroscopy calibration

The first measurements on the JDPD circuit were dedicated to evaluating the control that the currents across the DC lines and the fast flux line have on the resonance frequency of the device, which is directly linked to the device's potential configuration. The simplest way to estimate these effects consists in performing spectroscopy measurements, where the resonance frequency is recorded for each value of the applied magnetic flux. In Fig. 5.3 A JDPD's spectroscopy is reported as a function of ϕ_+ .

Measurements have been carried out by sending sufficient power to ensure that the JDPD wavefunction reaches the potential's absolute minimum. The plot in Fig. 5.3 A shows the presence of arches that modulates periodically with the

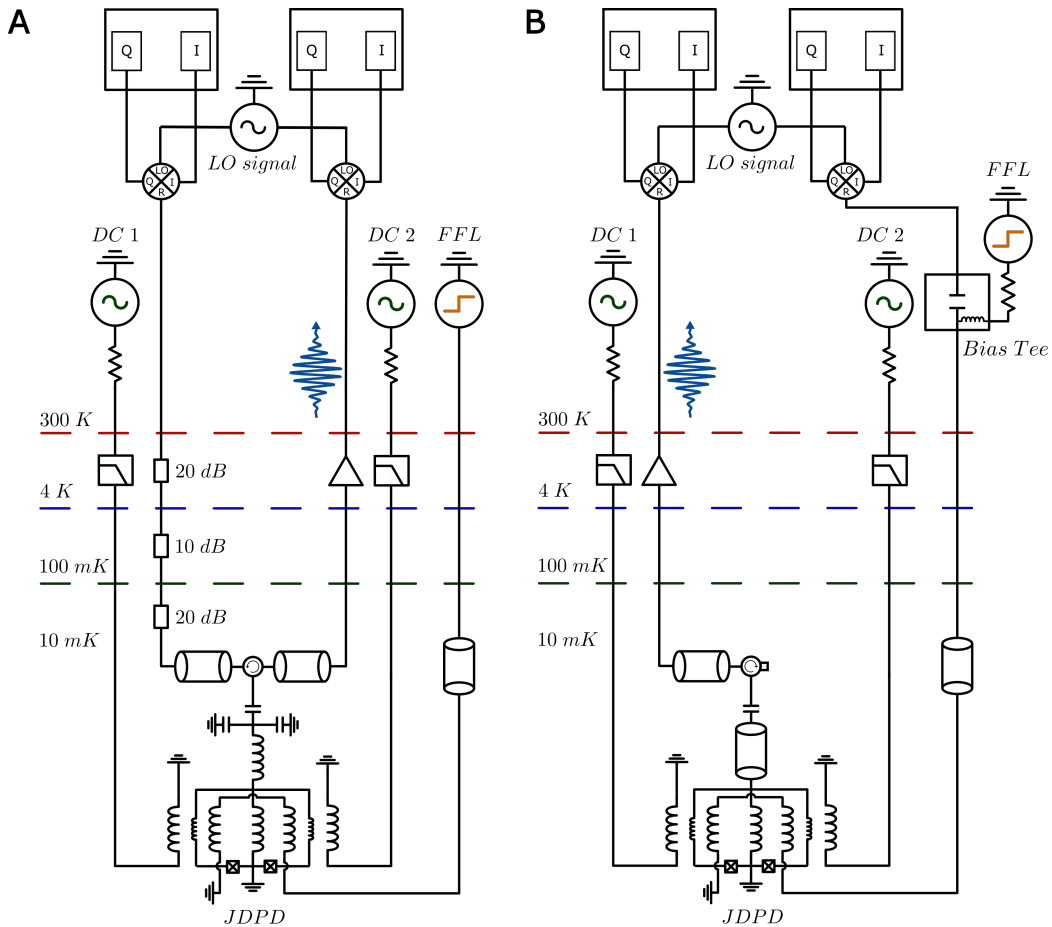


Figure 5.2: Schematic of the experimental setup adopted for the JDPD characterization. Panel A refers to the configuration adopted in reflection measurements. In panel B, we exhibit the setup in which the JDPD is measured in transmission by sending tones through FFL.

external flux. To be more precise, it's possible to observe a primary lobe, larger and slightly higher, and two secondary ones.

The periodicity is a hint related to the Josephson junctions employed in the JDPD circuit, which add a periodic term to the JDPD potential energy expression in Eq. 3.5. The pattern in Fig. 5.3 A exhibits a good agreement with the simulations in Fig. 5.3 B, performed starting from Eqs. 3.5, 5.2 and the design parameters discussed in Chapter 4. These results give evidence of the high quality of the sample and, at the same time, it demonstrates the reliability of the model used for the numerical analysis.

Comparing the experimental map with the simulated one, some relevant information can be obtained about the circuit under study. The maximum of the primary lobe coincides with the flux point $\phi_+ = 0$, where the potential is expected to have a single absolute minimum, according to Eq. 3.9. The top of the secondary lobes corresponds to $\phi_+ = \pi$ where the potential shape assumes a double well configuration. These three points allow us to calculate the peri-

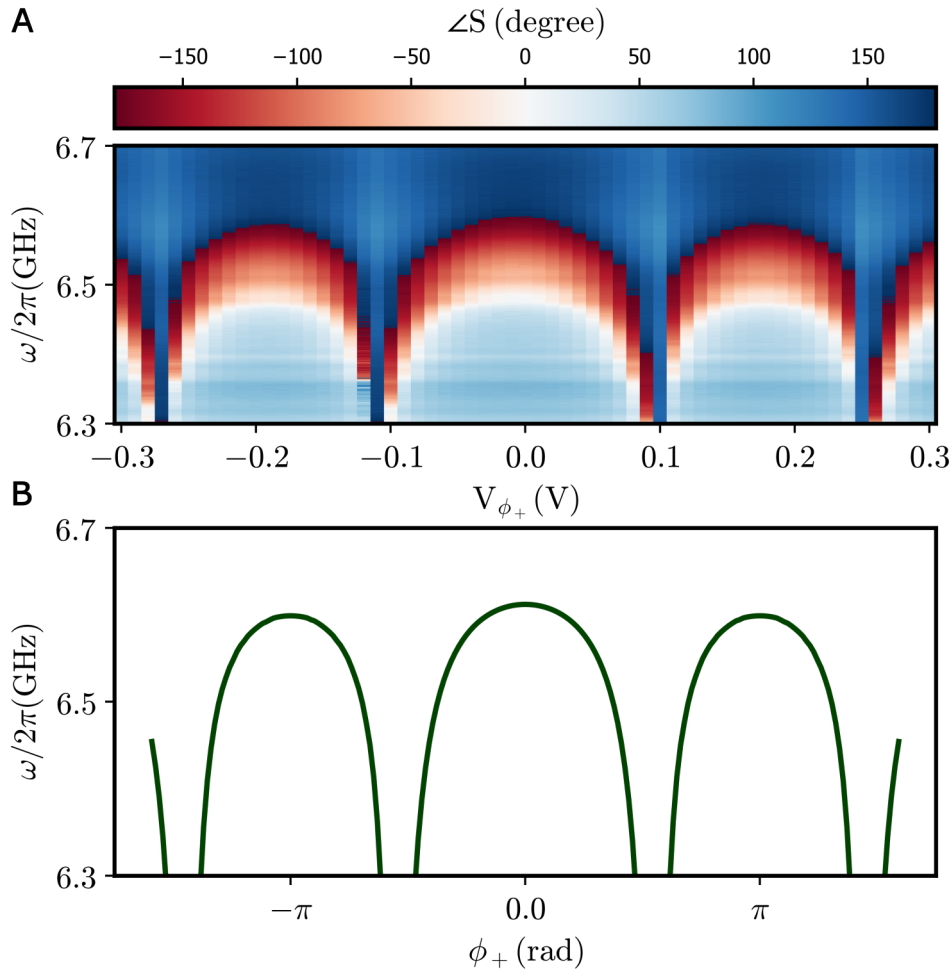


Figure 5.3: Experimental (A) and simulated (B) resonance frequency vs ϕ_+ . The plot shows the presence of arches that modulate with the external magnetic flux ϕ_+ . The periodicity is a hint related to the Josephson junctions employed in the JDPD circuit.

odicity in flux and the other interesting flux spot for the JDPD detection. For example, in the specific case of the measurement reported in Fig. 5.3 A, the voltage points corresponding to $V_{\phi_+=0} = -0.005V$ and $V_{\phi_+=\pi} = 0.186V$ leads to a periodicity of $\Delta V_{period} = 0.382V$. From these numbers, we can compute the flux point $V_{\phi_+=\pi/2} = 0.095 V$ for which the potential is expected to be in the harmonic configuration. The position of these flux points is not fixed in advance by the design and it requires a specific calibration each time the chip is cooled down.

From the relative height in frequency between the lobes, we can also obtain a rough estimation of the β parameter defined in Eq. 3.5. As mentioned in Chapter 3, β is an adimensional parameter proportional to the barrier height when the potential is set in the double well configuration. Given the experimental parameters used for the realization of our device, we have estimated $\beta = 6$, which is

large enough to guarantee the formation of a double-well potential when $\phi_+ = \pi$. Once we have determined the flux points with respect to ϕ_+ , we have to perform a similar analysis with respect to ϕ_- , which plays a fundamental role to control the system asymmetries. As discussed in the previous Chapters, ϕ_- is generated when the two dc lines provide the opposite amount of flux in the two JDPD's loops. In the ideal case, when the two lines have the same mutual coupling with the device, ϕ_- is generated when we supply the same currents from room temperature. However, in a real scenario, the two dc lines will have always different coupling due to a variety of reasons in the fabrication process. For example, improper layer alignment during manufacturing may result in a non-uniform spacing between the flux lines and the JDPD's branches.

The effect of non-uniform magnetic coupling can be observed by measuring the device resonance frequency vs ϕ_+ and ϕ_- . The theory predicts that if ϕ_- is correctly provided, the regions where the JDPD exhibits the maximum resonance frequencies are located on lines parallel to the y-axis, as reported in Fig. 5.4 B. In a real device, however, we can measure a map similar to one reported in Fig. 5.4 A, where the blue regions are tilted with respect to the x-axis, caused by the fact that the two dc lines are not biased properly and the contribution to the magnetic flux is not totally ϕ_- . By unbalancing properly the bias level of the two dc lines, the system can be calibrated to retrieve the desired condition. This has been done in Fig. 5.4 C, where the resonance vs ϕ_+ and ϕ_- shows a similar pattern to what is expected theoretically in Fig. 5.4 B.

5.4 Double well demonstration

The calibration of the JDPD is a fundamental step in order to determine the flux points and identify the various potential configuration. Before approaching phase detection, it's fundamental to find a way to distinguish where the phase particle is confined since the potential is set to have multiple wells.

In the theoretical read-out protocol described in Chapter 3, the bistable behaviour of the JDPD shows up as a superconducting current across the central inductance of the JDPD, whose direction depends on the particular well in which the phase particle has collapsed. With the actual chip design, there is no way of measuring such a current. Consequently, it is necessary to find a way to observe the bistable regime by using spectroscopy measurements. To overcome this experimental obstacle, a specific protocol has been employed which takes inspiration from the hysteresis measurement performed in the work Ref. [79]. This technique exploits both ϕ_+ and ϕ_- to adequately manipulate the JDPD potential energy in order to produce two different curves vs flux that help us to understand where the phase particle is trapped.

Initially, the potential is reset in the zero flux configuration, i.e $\phi_+ = 0$ and $\phi_- = 0$. The phase particle is expected to collapse in the absolute minimum of the potential corresponding to $\varphi = 0$. Suddenly, a little asymmetry $\phi_- = \theta_m$ ($\phi_- = -\theta_m$) is applied. The coordinates of the potential's absolute minimum

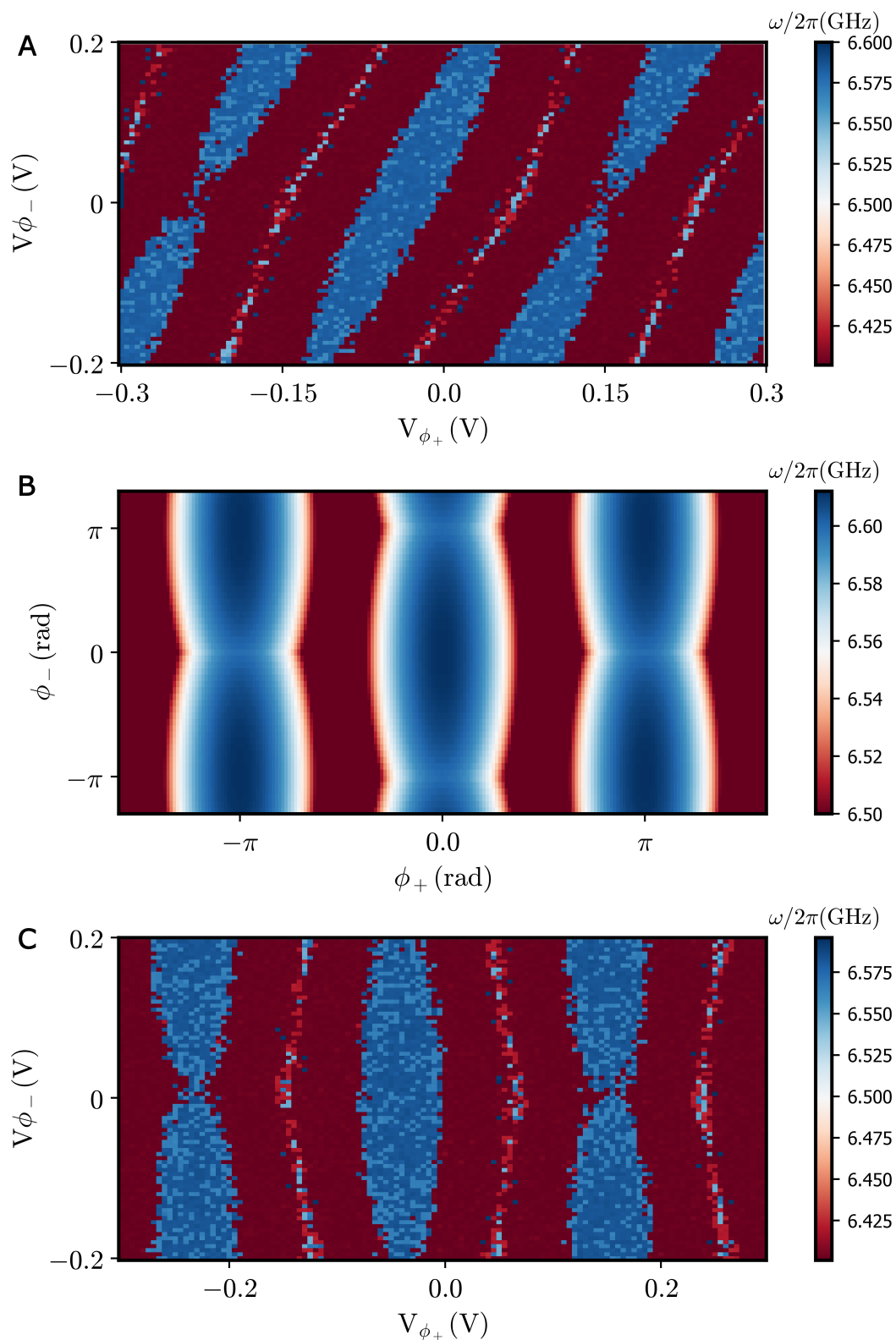


Figure 5.4: JDPD spectroscopy vs ϕ_+ and ϕ_- . (A) Experimental results assuming equally coupled dc lines. The maximum resonance frequencies are tilted with respect to the x-axis caused by the fact that ϕ_- is not provided correctly. (B) Expected resonance frequency map according to Eq. 5.2. (C) By adjusting properly the current provided through the two dc lines, it's possible to calibrate correctly the flux ϕ_-

acquire a little shift with respect to $\varphi = 0$. Since this operation is performed adiabatically, the wavefunction follows the potential time evolution and it remains trapped in the absolute minimum of the system as shown in Fig. 5.5 (b).

After this operation, a diabatic flux switch ($\phi_+ = 0 \rightarrow \phi_+ = \pi$) is applied which brings the JDPD in the double well configuration, as reported in panel (c) of Fig. 5.5. The phase particle remains bounded in the well where it has been prepared, which, for the effect of the asymmetry θ_m , corresponds to the deepest minimum in the potential energy. The deepest minimum is also the one characterised by the highest concavity and higher resonance frequency, which is the measurable quantity in the experimental setup, according to Eqs. 5.1, 5.2. At this point, by progressively decreasing (increasing) the flux ϕ_- , the initial tilt can be slowly reduced, providing a gradual decrease of the concavity related to the minimum where the phase particle is trapped. This leads to a lowering of the resonance frequency according to Eqs. 5.1, 5.2. As portrayed in Fig. 5.5 (d), the flux ϕ_- is provided step-wise from θ_m to $-\theta_m$ and between each stride, we measure the resonance frequency of the device. Repeating the entire procedure with the opposite initial condition of asymmetry θ_m , different behaviour of the resonance frequency vs flux is observed. This kind of hysteretic behaviour gives evidence of the presence of two wells that behave differently with respect to the magnetic flux inversion.

This experimental protocol has been simulated in Fig. 5.6 A on the basis of Eqs. 5.2 and 3.9 and considering the same parameters as in the experimental case, i.e $\beta = 7$ and $L = 220$ *pH*. With the condition $\phi_+ = \pi$, we have plotted the resonance frequency trend associated with the left well (blue) and right well (red) changing the external flux ϕ_- in the range $[-\pi, \pi]$. The blue and red curves cross for $\phi_- = 0$ where the two wells are expected to have the same resonance frequency.

The experimental outcomes are reported in Fig. 5.6 B. and C. In the plot of Fig. 5.6 B (1) the phase particle has been prepared in the right well and the flux has been ramped from π to $-\pi$, as indicated by the white arrow, with a total number of 41 steps; in the plot Fig. 5.6 B (2), we have arranged the wavefunction in the left well, and the flux has been provided in the opposite direction. This measurement has been performed with a power of -60 *dBm* at room temperature which is equivalent to a -110 *dBm* at the MXC stage considering the attenuation chain. The resonance frequency has been acquired in the range $\omega/2\pi = 6.5$ *GHz* to $\omega/2\pi = 6.6$ *GHz* with a step of 0.16 *MHz*.

The results are compatible with simulations in Fig. 5.6 A. In both cases, the resonance frequency decreases and there is a cross around $\phi_- = 0$ as expected theoretically. It's peculiar to observe a jump in the first plot of 5.6 B (1) near ϕ_- . The physical explanation behind this phenomenon, according to the potential energy shape, is that the phase particle has passed from the relative minimum to absolute one in the potential energy profile, which corresponds to larger concavity and a larger resonance frequency. In general, these jumps may have different origins, such as the thermal escape or the macroscopic quantum tunnelling [43] that for low enough energy separation between the minima can lead to a not neg-

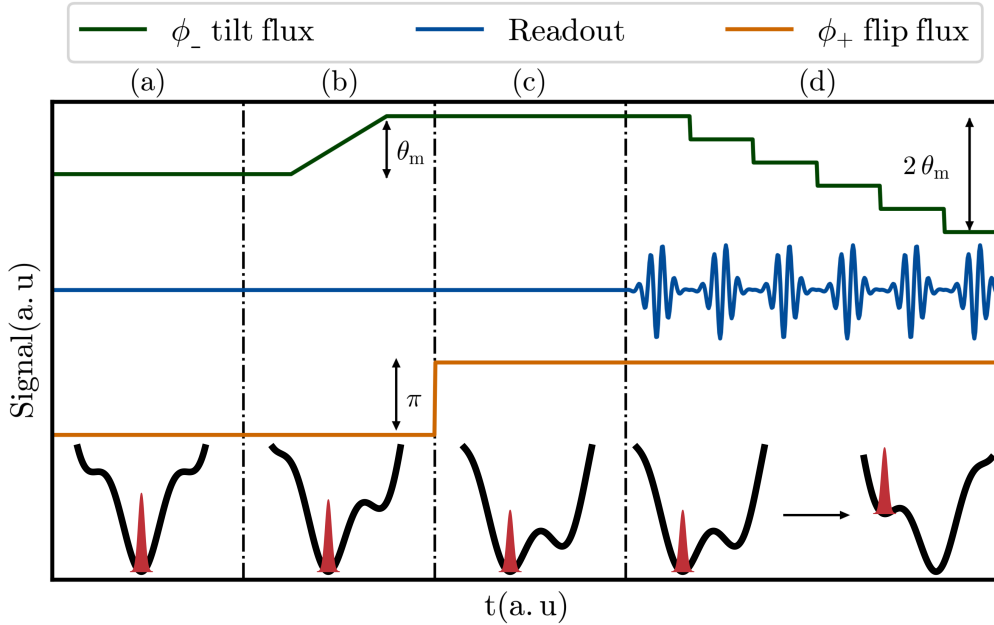


Figure 5.5: Experimental demonstration of potential energy tuning and capability to trap the phase particle in a chosen potential well.

The time evolution of ϕ_+ , ϕ_- and the readout tone to detect the JDPD's state are drawn in orange, green and blue lines respectively.

(a) Initially the potential is reset in the zero flux configuration, i.e. $\phi_+ = 0$ and $\phi_- = 0$. The phase particle is expected to collapse in the absolute minimum of the potential corresponding to $\varphi = 0$. (b) After the reset operation, the potential is prepared to be asymmetrical with respect to $\varphi = 0$ at $\phi_+ = 0$ applying $\phi_- = \theta_m$ with the dc flux lines. The coordinates of the potential's absolute minimum acquire a little shift with respect to $\varphi = 0$ corresponding to the symmetric case. Since this operation is performed adiabatically, the wavefunction evolves according to the potential time evolution and it remains trapped in the absolute minimum of the system.

(c) A diabatic flux switch ($\phi_+ = 0 \rightarrow \phi_+ = \pi$) is then applied which brings the JDPD in the double well configuration while the phase wavefunction is still trapped in the deepest minimum of the potential energy. (d) In the end, the flux ϕ_- is progressively decreased and between each step, we measure the resonance frequency of the device.

ligible escape probability of the wavefunction. Additionally, this transition can be supported by transmitted photons used to probe the system during the measurement, which can excite the phase particle. For instance, Fig. 5.6 C reports the same measurements performed with a higher power of -50 dBm. When compared to the case in Fig. 5.6 B, the power externally provided to readout the system state allows the phase particle to reach the absolute minimum of the potential energy. The same behaviour has been observed in cases with a VNA attenuation of -60 dBm, proving that in this case, the escape is caused by stochastic effects like thermal escapes and macroscopic quantum tunnelling [43].

5.5 Symmetry point determination

Once we have calibrated the flux points of the system and demonstrated the existence of a double well potential, the following step is the determination of the symmetry point θ_{symm} concerning the flux ϕ_- . As suggested by the name, θ_{symm} is the value of ϕ_- which leads to an equal distribution of the probability in the two wells when a flux switch is applied in absence of any external input signal. The determination of θ_{symm} is crucial to achieving state-independent fidelity. Theoretically, θ_{symm} should correspond to $\phi_- = 0$. However, some factors, such as asymmetric junctions, could lead to $\theta_{symm} \neq 0$, as widely discussed in Section 3.6.

To determine the symmetry point, we have experimentally realized the protocol in Fig. 5.7 composed of 5 distinct steps. Initially, the potential is set in the harmonic configuration applying a $\phi_+ = \pi/2$ pulse. We wait a cooldown time of 100 ns to ensure that the wavefunction collapses in the minimum of the potential energy. This step forces the device to “Reset” in the ground state and makes it ready to be flipped in the double well configuration. At $t = 100$ ns we supply $\phi_- = \theta_{symm}$, which is the variable that we want to determine. The potential is flipped in the double well configuration at 140 ns, as indicated in Fig. 5.7 (c). The flux switch is provided diabatically, with a rise time of 1 ns corresponding to the maximum achievable by our AWGs. The effect of the potential flipping makes the wavefunction collapse in a probabilistic way in the left $|L\rangle$ or right $|R\rangle$ state. If the applied asymmetry θ_{symm} is a suitable value to remove the intrinsic asymmetry, we expect to observe an equal splitting of the wavefunction in the two available states.

The readout of the JDPD state is accomplished in steps (d) and (e). As discussed in the previous Sections, with the actual chip design, there is no way of measuring the superconducting current that passes through the inductor L and the JDPD’s readout is performed by using the spectroscopy measurement. However, in the symmetric condition when left $|L\rangle$ and $|R\rangle$ states are equiprobable, the two wells have the same resonance frequency and it’s tricky to distinguish them.

To overcome this difficulty, we can unbalance a little bit the frequency of the two states by applying $\phi_- = \theta_{detect}$. Reasonably, θ_{detect} should be small enough to not perturb too much the system. In the case of our measurement, we have chosen

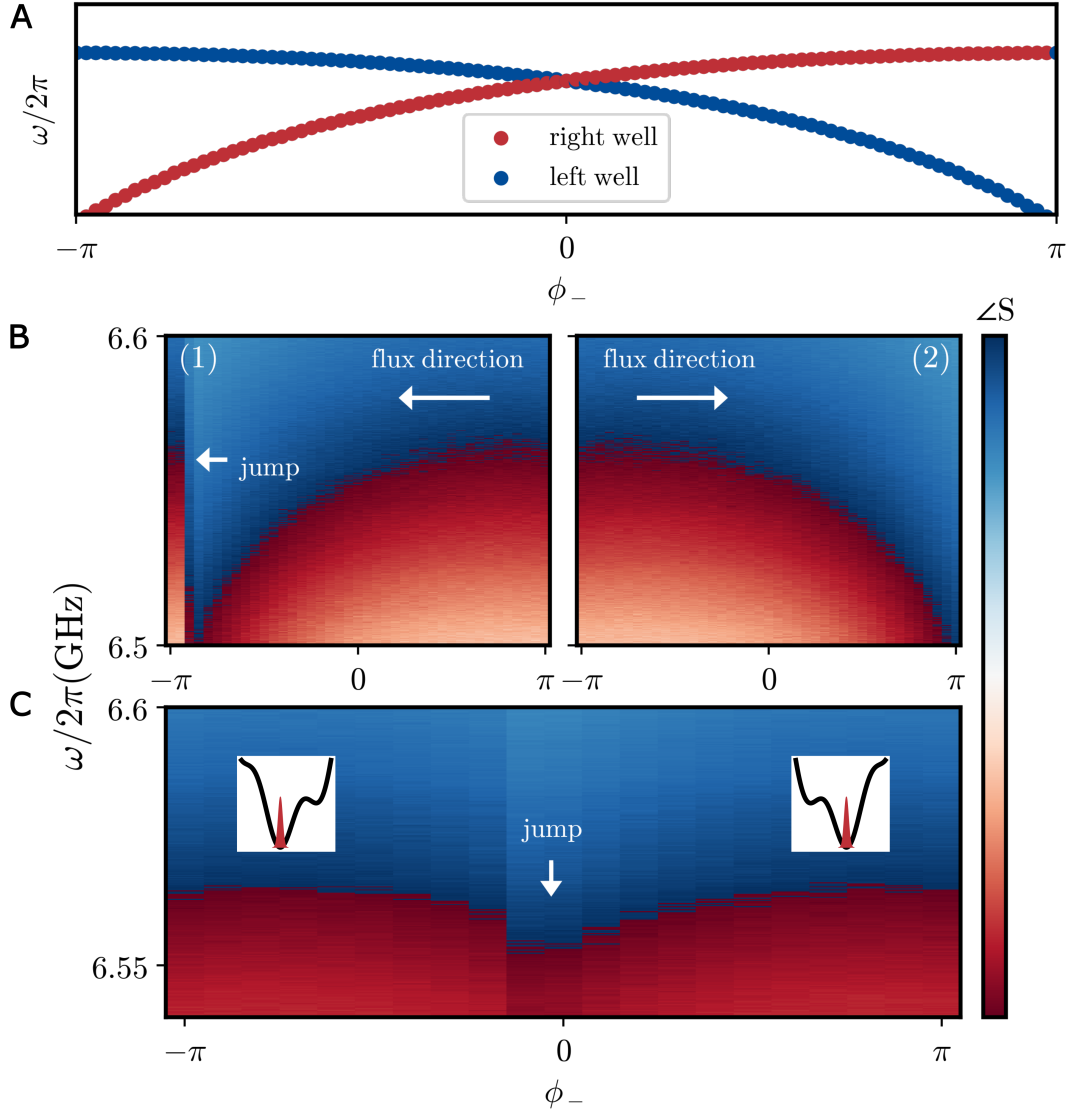


Figure 5.6: (A) Simulation of the protocol reported in Fig. 5.5 according to Eqs. 5.2, 3.9 and considering the design parameters, i.e $\beta = 7$ and $L = 220$ pH. The figure shows the resonance frequency trend associated with the left well (blue) and right well (red) changing the external flux ϕ_- in the range $[-\pi, \pi]$ and considering $\phi_+ = \pi$. The blue and red curves cross for $\phi_- = 0$ where the two wells are expected to have the same resonance frequency. (B) Experimental results from the realization of the timing diagram are reported in Fig. 5.5. In plot (1), the phase particle has been prepared in the right well and the flux has been ramped from π to $-\pi$, as indicated by the white arrow; in the plot (2), we have prepared the wavefunction in the left well and the flux has been provided in the opposite direction. This measurement has been performed with a power of -60 dBm at room temperature. The resonance frequency has been acquired in the range $\omega/2\pi = 6.5$ GHz to $\omega/2\pi = 6.6$ GHz with a step of 0.16 MHz. The results are consistent with simulations in Fig. 5.6 A. In both cases, the resonance frequency decreases and there is a cross around $\phi_- = 0$ as expected theoretically. (C) Measurements performed with the same sequence as in B but with larger power to readout the JDPD's state (-50 dBm). The phase particle reaches the absolute minimum of the potential energy which corresponds to larger concavity and so to a larger resonance frequency

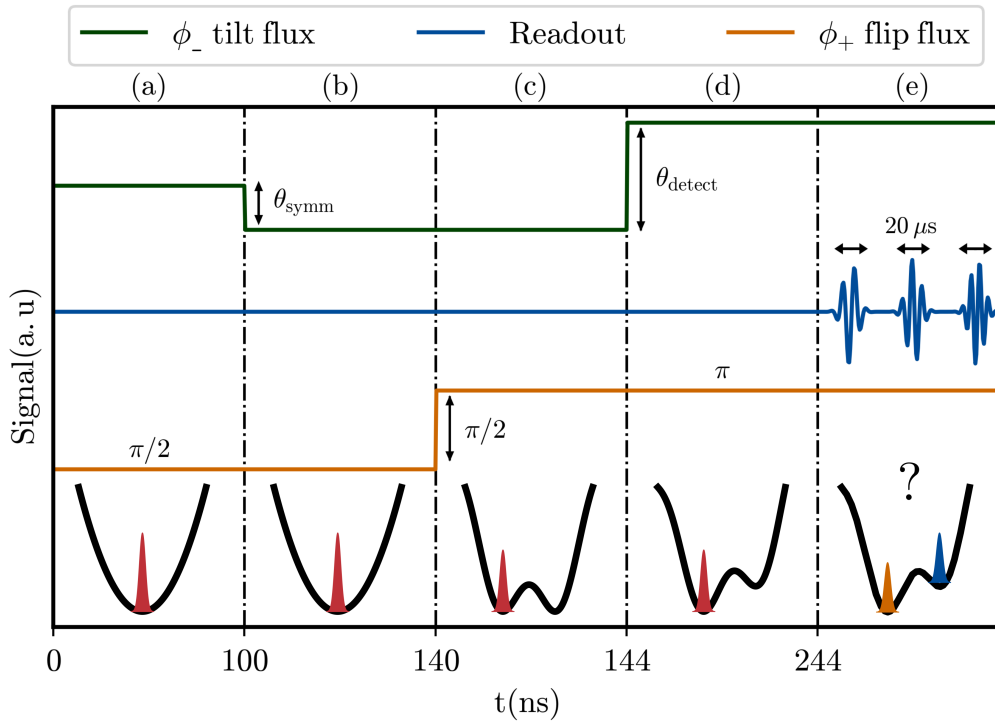


Figure 5.7: Timing sequence to determine θ_{symm} . (a) Initially, the potential is set in the harmonic configuration which forces the device to “Reset” in its ground state. (b) A $\phi_- = \theta_{symm}$ is supplied to correct the intrinsic asymmetries of the device. (c) A flux switch sets the JDPD in the double well configuration and the wavefunction collapses in a probabilistic way in the left $|L\rangle$ or $|R\rangle$ state. If the applied asymmetry θ_{symm} is adequate to remove the intrinsic asymmetry, we expect to observe an equal splitting of the wavefunction in the two available states. (d) Since the left $|L\rangle$ and $|R\rangle$ states have very similar resonance frequencies, it’s tricky to distinguish them. We unbalance a little bit the frequency of the two states by applying $\phi_- = \theta_{detect}$ to increase their measurement separability. (e) The detector is read out by applying tones at different frequencies. The sequence is repeated several times to make statistics and measure the trapping probability for each value of θ_m .

$\theta_{detect} = 0.2 \text{ rad}$, which has proven to be a good value for the observability of the $|L\rangle$ and $|R\rangle$ states.

Starting from $t = 244 \text{ ns}$ we read out the detector by applying tones at different frequencies. The sequence in Fig. 5.7 is repeated several times to make statistics and measure the trapping probability for each value of θ_m .

An experimental realization of the protocol described above is reported in Fig. 5.8 for $\theta_{symm} = 0.03 \text{ rad}$. Plots A and B in Fig. 5.8 show respectively the amplitude and phase of the S parameters as a function of the number of reps and the frequency $\omega/2\pi$. The measurements have been performed in the range $[6.496, 6.502] \text{ GHz}$ with a total number of 60 steps and 500 repetitions, with a time duration of $20 \mu\text{s}$ for each repetition. In the figures, it's possible to observe fringes corresponding to the two JDPD states when it's flipped in the double well configuration. The presence of two states is confirmed by the quadrature amplitude analysis reported in Fig 5.8 C. Counting the red and blue points we get a trapping probability of 49.5% in the left well and 50.5% in the well. These values correspond to an equal probability to reach left and right states, within the statistical error.

5.6 Phase detection demonstration

With the determination of θ_{symm} , the JDPD calibration is concluded and we can evaluate experimentally the JDPD's capability to work as a phase detector. The detection time sequence is very similar to the one discussed for the symmetry point determination, as reported in Fig. 5.9. Phase detection begins resetting the system in the harmonic configuration (Fig. 5.9 A.). The system evolves in this condition for 100 ns which is long enough to ensure the collapsing of the wavefunction in the ground state. At $t = 100 \text{ ns}$, we apply $\phi_- = \theta_{symm}$ to compensate for the device's asymmetries and to guarantee state-independent fidelity, as discussed in the previous Section. With respect to the protocol illustrated in Fig. 5.7, where the wavefunction evolves without any external perturbation, in step (c) of Fig. 5.9 an input stimulus is supplied for a total duration of $3 \mu\text{s}$. The application of this tone makes the wavefunction oscillate coherently around the potential minimum, as expected from simulations reported in Chapter 3. In step (d) the JDPD is flipped in the double well configuration. As for the case of θ_{symm} determination, the flux-switch is provided diabatically with a rise time of 1 ns . As a consequence, the wavefunction collapses in the $|R\rangle$ or $|L\rangle$ state depending on its position with respect to $\varphi = 0$ at the instant when the flux switch is applied. To ensure the overlap between the pulses, we retarded the end of the stimulus by $\Delta\tilde{t} = 4 \text{ ns}$ with respect to the beginning of the flux switch, as shown in Fig. 5.9

The JDPD readout is accomplished in steps (e) and (f). Similar to what has been done for the "symmetry point determination", we unbalance the frequency of $|L\rangle$ and $|R\rangle$ supplying $\phi_- = \theta_{detect}$. The JDPD is measured in reflection at different readout frequencies. The detection time sequence reported in Fig. 5.9

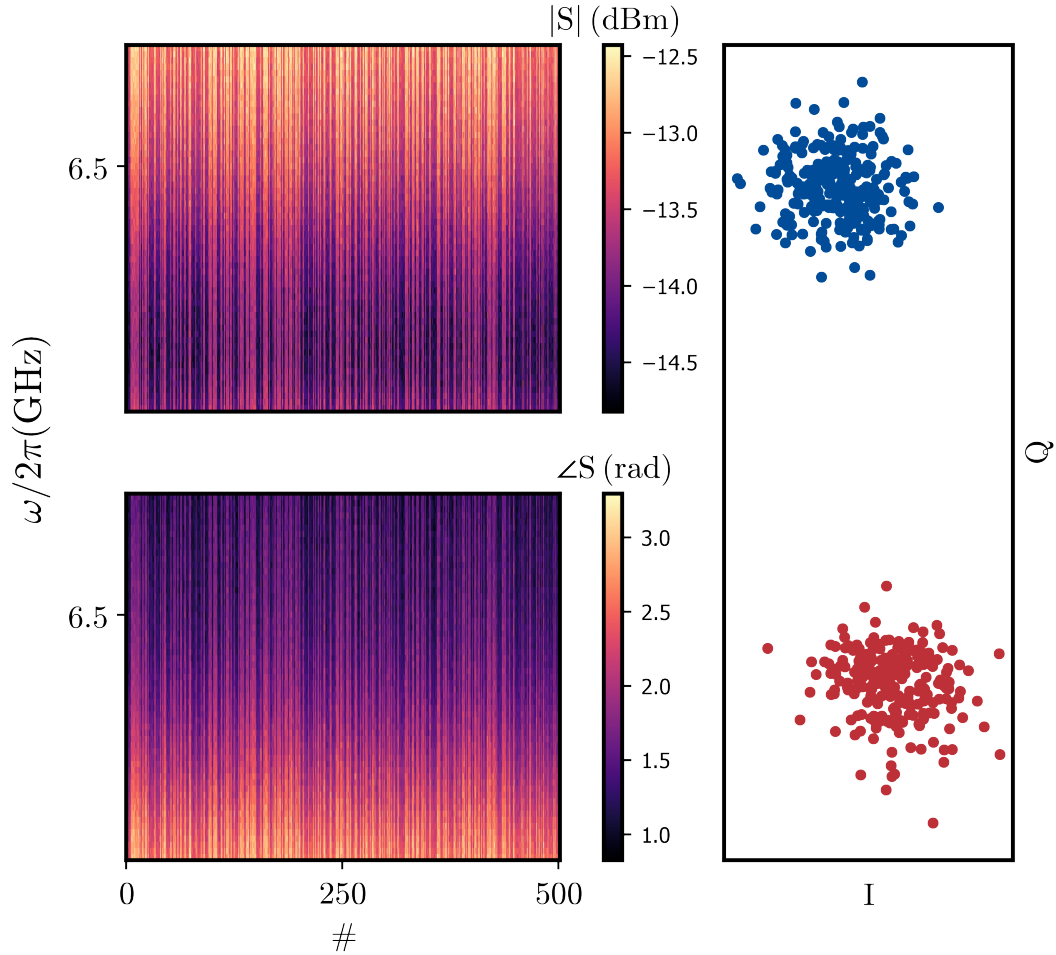


Figure 5.8: Experimental realization of the θ_{symm} protocol reported in Fig. 5.7 for $\theta_{symm} = 0.03$ rad. (A) and (B) show respectively the amplitude and phase of the S parameters as a function of the number of reps $\#$ and the frequency $\omega/2\pi$. The measurements have been performed in the range $[6.496, 6.502]$ GHz with a total number of 60 steps and 500 repetitions. It's possible to observe fringes corresponding to the two JDPD states when it's flipped in the double well configuration. Probability is calculated by counting the number of fringes corresponding to the two states (C) Quadrature amplitude measurements, which demonstrate the presence of two blobs of points.

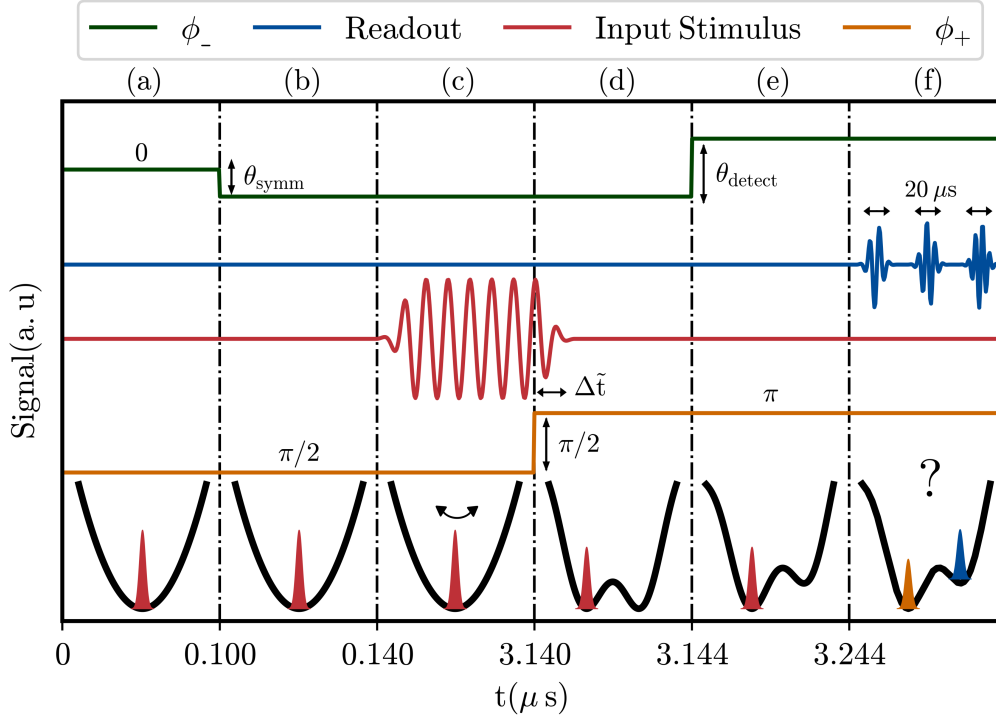


Figure 5.9: Experimental protocol to demonstrate phase detection. The time sequence of the fluxes applied to the JDPD is reported, following the legend in the upper part of the figure. (a) The detector is initially reset in the ground state of the harmonic configuration. (b) $\phi_- = \theta_{\text{symm}}$ is supplied to compensate for the device’s asymmetries and to guarantee state-independent fidelity. (c) An input stimulus is supplied which makes the wavefunction oscillate coherently around the potential minimum. This input tone is provided for a total duration of $3 \mu\text{s}$. (d) The JDPD is flipped, with 1 ns rise time flux switch, in the double well configuration and the wavefunction collapses in the $|R\rangle$ or $|L\rangle$ state depending on its position with respect to $\varphi = 0$ when the flux-switch is applied. To ensure the overlap between the pulses, we retarded the end of the stimulus by $\Delta\tilde{t} = 4 \text{ ns}$ with respect to the beginning of the flux switch. (e) Similar to what was done for the symmetry point determination, we unbalance $|L\rangle$ and $|R\rangle$ supplying $\phi_- = \theta_{\text{detect}}$ to make the two-state frequency distinguishable. (f) The JDPD is measured in reflection at different frequencies around the resonance one.

is repeated several times to make statistics on the trapping probability. One can play with the initial phase θ of the input stimulus to investigate how probability is affected by this factor.

The duration of the sequence reported in Fig. 5.9 is around a few μs . However, most of the time steps can be sped up by employing appropriate SFQ devices such as an SFQ comparator and an SFQ flux generator. We think that by using these devices it's possible to perform the detection in a time scale of tens of nanoseconds, as demonstrated theoretically in Chapters 3 and 4.

The primary mode to send the input stimulus exploits the use of the input line. However, there is another possibility to provide the input tone through two dc lines. In the following, I will explore both the approaches and the related results.

5.6.1 Input signal through dc lines

One possibility to provide the input tone is through the dc lines coupled with the JDPD. When properly biased, their geometrical position guarantees that only a contribution ϕ_- is generated.

When $\phi_- = 0$, the two JDPD loops (assumed to be perfectly symmetrical) are threading by the same amount of magnetic flux, which means that $\phi_1 = \phi_2$. By applying Kirchhoff's current law at the input node, the net current flowing through the central inductor L is zero. For the same principle, when $\phi_- \neq 0$, the total current flowing through the inductor L is non-zero which is formally equivalent to a signal sent at the input node. In other words, the application of $\phi_- \neq 0$ offers the possibility to provide an input stimulus.

This evidence can be demonstrated mathematically by applying the transformation:

$$\tilde{\varphi} \equiv \varphi + \phi_- \quad (5.3)$$

to the Eq. 3.5. The overall Hamiltonian can be now written as:

$$H = 2E_c n^2 + \frac{E_L}{2} \left(\tilde{\varphi} - \phi_- \right)^2 - 2E_J \cos(\phi_+) \cos(\tilde{\varphi}) + C \dot{\phi}_+ \quad (5.4)$$

In the "ready" state the device is prepared at $\phi_+ = \pi/2$. In this case, the Hamiltonian reads:

$$\begin{aligned} H &= 2E_c n^2 + \frac{E_L}{2} \left(\tilde{\varphi} - \phi_- \right)^2 = \\ &2E_c n^2 + \frac{E_L}{2} \left(\tilde{\varphi}^2 - 2\phi_- \tilde{\varphi} \right) + \frac{E_L}{2} \phi_-^2 \end{aligned} \quad (5.5)$$

From this expression is clear that, in the ready state, this expression is equivalent to the Hamiltonian of a driven LC oscillator.

This technique has been exploited principally for the devices from release v1, where the presence of a high Q CPW resonator limits the propagation of signals out of resonance through the input line. Some experimental outcomes for differ-

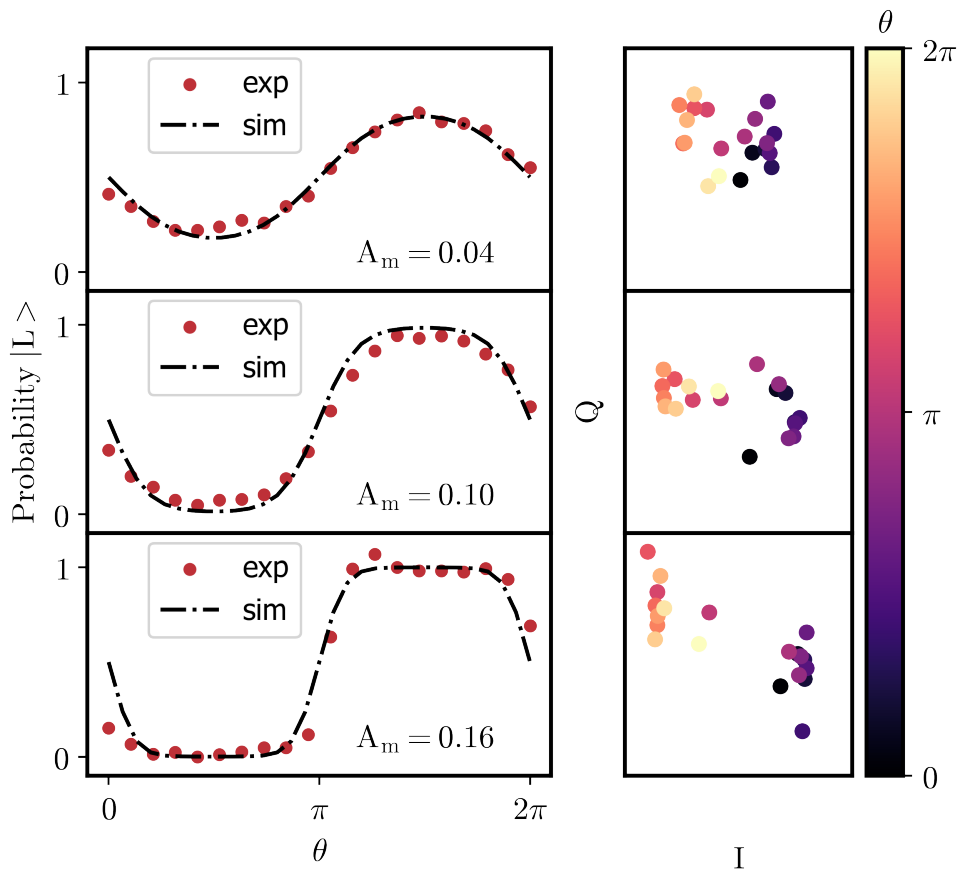


Figure 5.10: Experimental results of phase detection performed by providing the input tone through the dc lines. Detection has been performed with a stimulus having a frequency of 1 MHz and changing the amplitude A_m , expressed in terms of the flux ϕ_- . When the amplitude is large enough, as in the case of $A_m = 0.16\text{ rad}$, the JDPD is able to perform a full digitalization of the stimulus phase θ . More precisely, repeating the sequence 50 times, the wavefunction collapses with a probability 1 in the state $|R\rangle$ for $\theta \in [1, 3]$ and in the state $|L\rangle$ for $\theta \in [3.9, 5.9]$. This range of values reasonably decreases, as for $A_m = 0.10\text{ rad}$, until, in the case of small input amplitudes ($A_m = 0.04\text{ rad}$), independently on the value of θ , the wavefunction is no more capable to reach the $|L\rangle$ and $|R\rangle$ states with probability equal to 1. In this situation, the points interpolation of the *Probability* $|L\rangle$ vs θ exhibits a sinusoidal shape compatible with the input tone profile. When the A_m increases, the effect of digitalization leads to a “clipping” of shape, which is evident for $A_m = 0.16\text{ rad}$.

ent values of the input tone phase θ are reported in Fig. 5.10.

Detection has been performed with a stimulus having a frequency of 1 *MHz*. This value is small compared to the typical frequencies of superconducting qubits but it's the maximum achievable considering the signal's distortions produced at relatively high frequency.

The signal amplitude is expressed in terms of ϕ_m extracted from a spectroscopy map as the one reported in Fig. 5.4 C. Fig. 5.10 shows the probability to reach the state $|L\rangle$ for three different amplitudes A_m of the stimulus input. When the amplitude is large enough, as in the case of $A_m = 0.16 \text{ rad}$, the JDPD is able to perform the digitalization of the stimulus phase θ . More precisely, repeating the sequence of Fig. 5.9 50 times, the wavefunction collapses with a probability 1 in the state $|R\rangle$ for $\theta \in [1, 3]$ and in the state $|L\rangle$ for $\theta \in [3.9, 5.9]$. This range of values reasonably decreases, as for $A_m = 0.10 \text{ rad}$, until, in the case of small input amplitudes ($A_m = 0.04 \text{ rad}$), independently on the value of θ , the wavefunction is no more capable to reach the $|L\rangle$ and $|R\rangle$ states with probability equal to 1. In this situation, the points interpolation of the *Probability* $|L\rangle$ vs θ exhibits a sinusoidal shape compatible with the input tone profile. When the A_m increases, the effect of digitalization leads to a “clipping” of shape, which is evident for $A_m = 0.16 \text{ rad}$.

Experimental results, reported with red points in the left panel of Fig. 5.10, have been compared with simulations in QuTip, revealing a significant agreement between theory and experiments. The averaged measurement points in the I-Q plane varying the input displacement θ are shown in the right panel of Fig. 5.10. It's possible to note two main “blobs” of points. According to the analysis performed *Probability* $|L\rangle$ vs θ , the distance between their centre progressively increases with the amplitude A_m .

5.6.2 Input signal through input line

The experimental results reported in the previous Section and the remarkable agreement with simulations demonstrate the capability of the JDPD to work as a phase detector.

However, due to the transmission limitation through the dc lines, detection has been performed in a range of frequencies very distant from the microwave regime. To verify the compatibility with qubit readout, it's necessary to demonstrate the feasibility of the JDPD technique at frequencies around 1 *GHz*. Devices from release v2 have been adequately designed to perform phase detection near the microwave regime to overcome the limitations encountered with layout v1. As discussed in Chapter 4, the JDPDs from this release are coupled to low external Q resonators which allow signals with frequencies below the resonance to be transmitted with relatively low power from RT. This makes detection through the input line in principle possible in a wide range of stimulus frequencies.

Experimental outcomes performed within this approach are reported in Fig. 5.11. Considering as reference the sequence reported in Fig. 5.9, the detection protocol

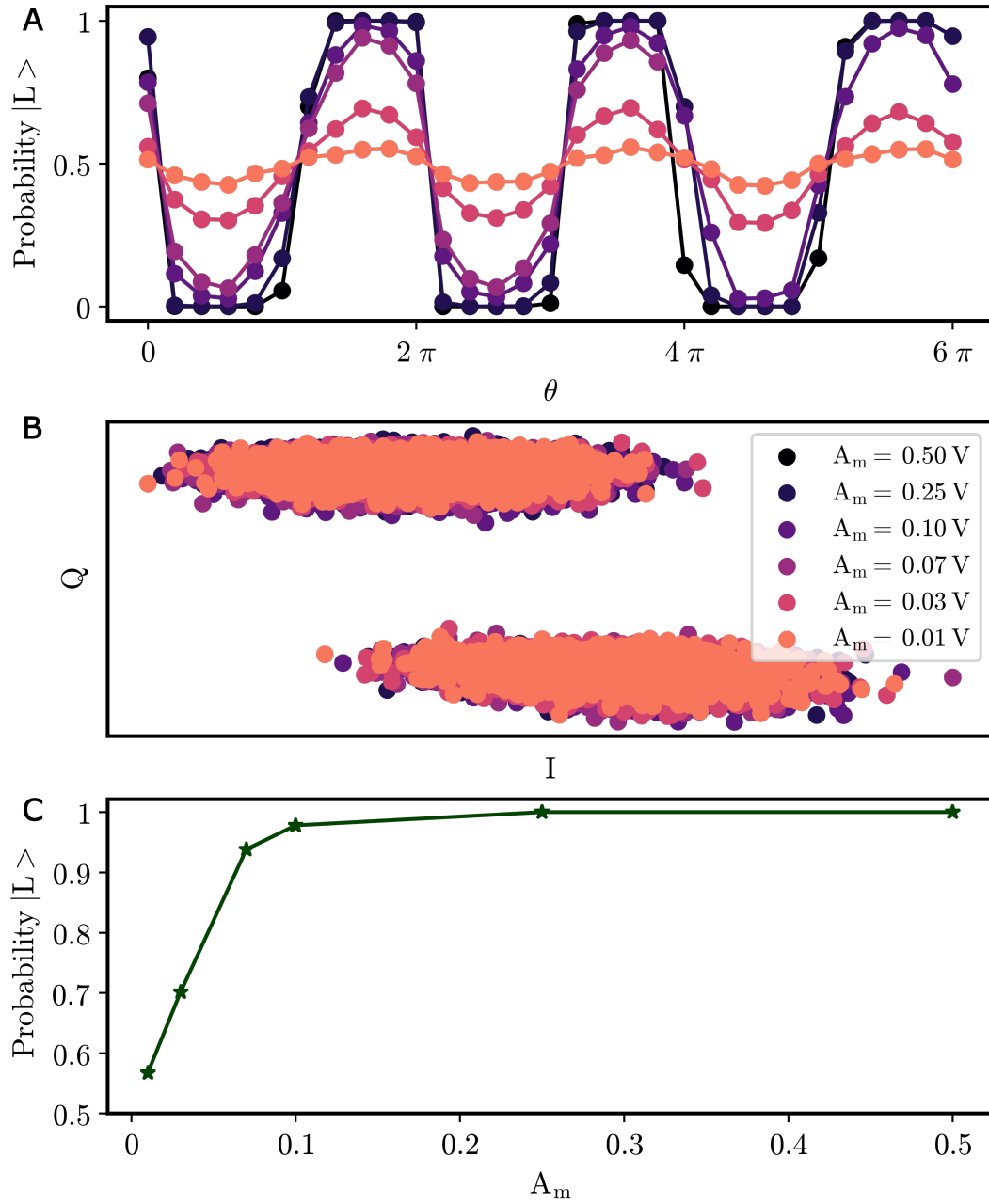


Figure 5.11: (A) Detection through the input line performed at 200 MHz for several values of input amplitude A_m . The JDPD demonstrates to be capable to digitalize the stimulus phase θ when the amplitude is large enough. (B) The state $|L\rangle$ and $|R\rangle$ corresponds to well-separated blobs in the I, Q plane. The centre of these spots is amplitude independent, which means that it's possible to fix a unique threshold for each A_m value. (C) Decreasing the stimulus amplitude, the *Probability* $|L\rangle$ shows an exponential drop until it's not possible to distinguish the two states below $A_m = 0.01\text{V}$

has been performed changing the stimulus initial phase θ in the range $\theta \in [0, 6\pi]$. For each value of θ , we have repeated the measurements sequence 5000 times to have representative statistical samples.

Measurements have been carried out with an input frequency of 200 MHz and in a wide range of amplitudes A_m . This value is expressed in terms of the AWG amplitude at Room Temperature. We cannot determine a direct link between the amplitude expressed in voltage and the flux ϕ_- , as done in the case of phase detection performed through dc lines. However, from the electrical model of our device, we roughly estimated an equivalent current at the JDPD input node [$\simeq 0.2 \mu, 1 \mu A$], given the amplitudes provided at RT and reported in Fig. 5.11. Results are compatible with what has been observed in Fig. 5.10. The JDPD is capable to digitalize the stimulus phase θ when the amplitude is large enough. This is the case of $A_m = 0.5 \text{ V}$ or $A_m = 0.25 \text{ V}$. Decreasing the stimulus amplitude, the *Probability* $|L\rangle$ shows an exponential drop until it's not possible to distinguish the two states below $A_m = 0.01 \text{ V}$, as reported in Fig. 5.11 C. The states $|L\rangle$ and $|R\rangle$ correspond to well-separated blobs in the I, Q plane, according to Fig. 5.11 B. It's worth noting that the centre of these spots is amplitude independent, which means that it's possible to fix a unique threshold for each A_m value. The JDPD capability to perform phase detection has been demonstrated for multiple frequencies of the input stimulus, as reported in Fig. 5.12 with similar results as in the case of $\omega = 200 \text{ MHz}$.

According to Qucs simulations, for $\omega = 100 \text{ MHz}$ the signal is too small to produce large oscillations of the wavefunction in the harmonic configuration. As a consequence, the JDPD fails to distinguish the left $|L\rangle$ and right $|R\rangle$ state even if the amplitude provided at room temperature is 0.5 V . For $\omega = 250 \text{ MHz}$ and $\omega = 400 \text{ MHz}$ the separability of the two states is recovered and the JDPD demonstrates the capability to digitally discriminate the input phase θ .

Since the maximum sampling rate is equal to 1 GS/s , it's not possible to generate input tones with frequencies higher than 400 MHz using directly the AWGs. One possibility to overcome this difficulty is to mix the signals generated from the AWG with a LO tone, following the approach described in Chapter 2. However, to generate an input tone with a precise value of θ , the IQ and the carrier tone from the LO should be phase-locked together. This condition can be satisfied by using another AWG channel as LO provider. Our AWGs can produce tones at frequencies up to 400 MHz , which means that we need to exploit higher harmonics of the mixing process in order to reach a frequency around 1 GHz . Furthermore, it's necessary to calibrate the mixer to suppress the other tones that otherwise could contribute to the generated signal.

We have found an ideal working point for $\omega_I = 320 \text{ MHz}$, $\omega_Q = 320 \text{ MHz}$ and $\omega_{LO} = 320 \text{ MHz}$ corresponding to an output signal dominated by the second harmonic at 960 MHz and 1 V of amplitude and a secondary contribution at 320 MHz and 0.2 V . Phase detection has been performed with a little modification with respect to the protocol described in Fig. 5.9. To avoid unwanted effects during the mixing process, we set the phase θ of the input tone to a fixed value and change the instant when the JDPD is flux-switched. In this way, we

5.6. PHASE DETECTION DEMONSTRATION

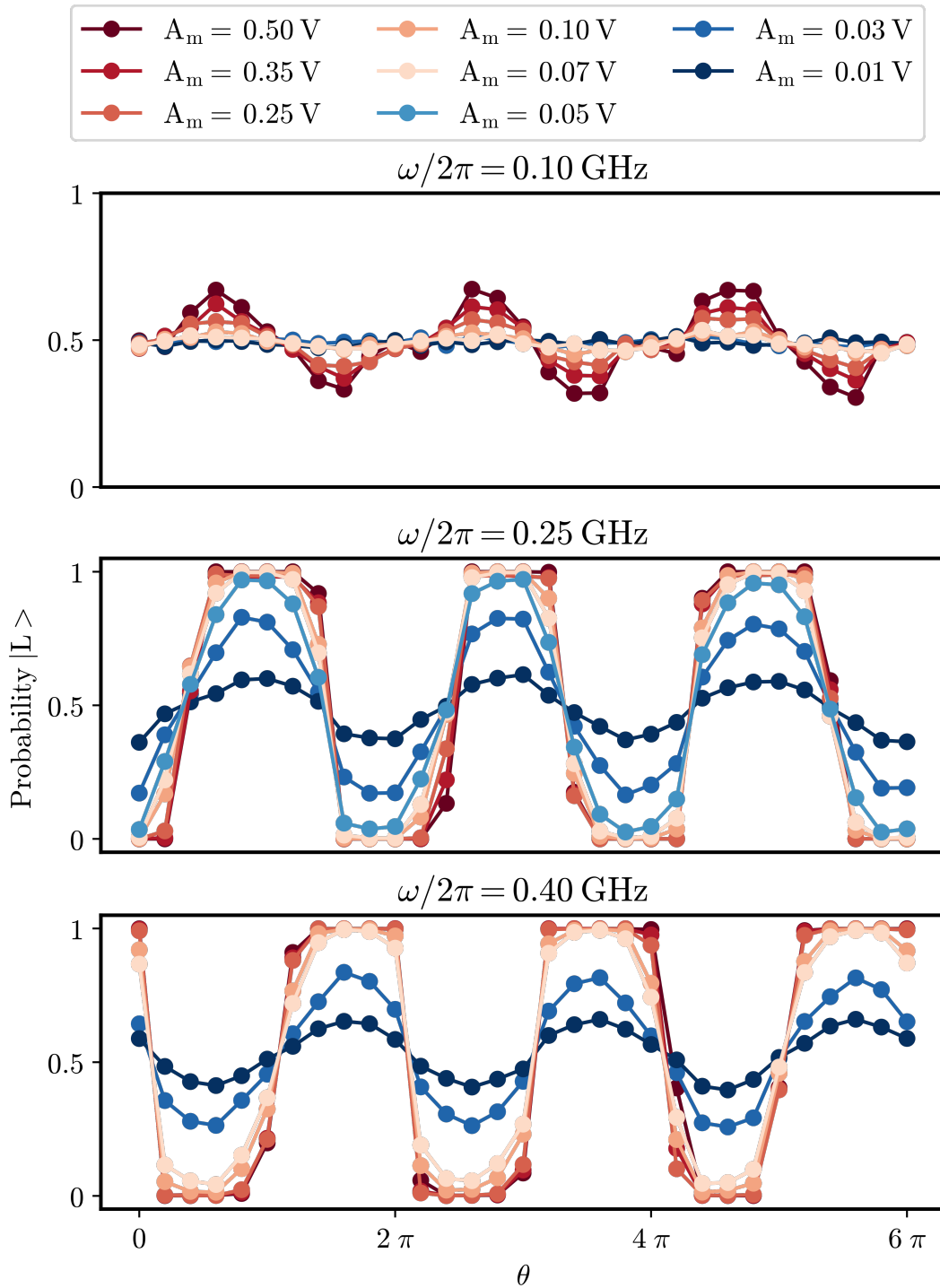


Figure 5.12: Phase detection performed for different input frequencies and amplitudes A_m . The JDPD is able to perform a full digitalization of the input tone phase sign when A_m is large enough. Instead, for small values of A_m , the phase particle does not reach the $|R\rangle$ and $|L\rangle$ states with probability equal to 1, as in the case of amplitudes related to blue points. The effective power that reaches the JDPD depends on the stimulus frequency since the lumped resonator in series to the device works as a bandpass filter. This explains why JDPD fails to digital detect the stimulus at $\omega/2\pi = 0.10 \text{ GHz}$ while its performance is better at higher frequencies.

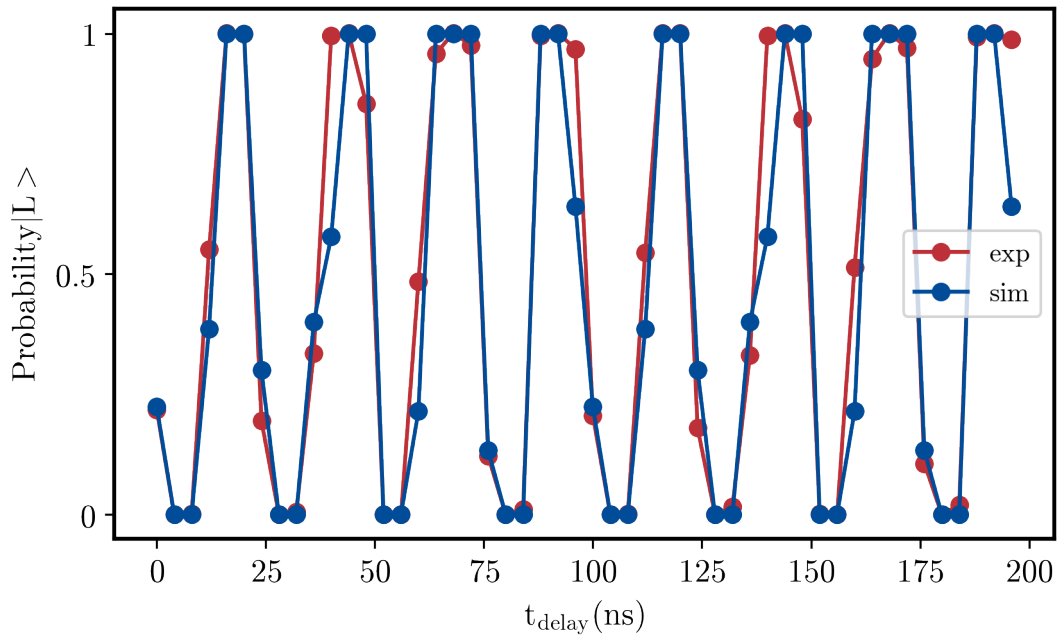


Figure 5.13: Digital Phase detection of a signal at 960 MHz , generated mixing together tones at 320 MHz . To avoid unwanted effects during the mixing process, we set the phase θ of the input tone to a fixed value and change the instant when the JPDP is flux-switched. In this way, we can modify “artificially” the stimulus phase with respect to the moment when the discrimination is performed. Experimental results show a remarkable agreement with numerical simulation, which demonstrate the feasibility of the JPDP approach with tones in the microwave regime.

can modify “artificially” the stimulus phase with respect to the moment when the discrimination is performed.

Experimental results obtained with this approach are reported in Fig. 5.13. The flux-switch is delayed from 0 to 200 ns with steps of 4 ns . Also in these more stringent conditions, the JPDP is able to digitalize the input stimulus with good agreement with simulations. This is important evidence of the fact that the JPDP can work with tones in the microwave regime, and thus can be employed to readout the state of a superconducting qubit.

Conclusions

In this PhD thesis, I have proposed an SFQ-compatible readout technique based on a flux-switchable JDPD.

The detection protocol exploits the possibility for the JDPD to change from a harmonic to a double-well potential configuration. The device is capable of digitalizing the phase sign of an input signal at GHz frequencies, encoding the information in the occupation probability of the phase particle in either of two wells in the bistable configuration.

The JDPD approach has been completely investigated from a theoretical and experimental perspective. Numerical simulations demonstrate that detection can be accomplished in a time scale of few nanoseconds with fidelity approaching 1. During the operations, the JDPD is not required to be in resonance with the input signal frequency. Thus, the device can be designed to have precise energy transitions, which allow us to reduce as much as possible the backaction on the rest of the circuit. The JDPD shows resilience to the presence of asymmetries or fabrication spread, which can be corrected by the advanced control offered by ϕ_+ and ϕ_- .

These theoretical estimations are supported by experimental results obtained on several devices from two different releases. We have demonstrated digital phase detection in a wide range of operation regimes and device configurations.

Of great interest is the compatibility of this approach with the SFQ architecture. We have investigated numerically the integration of JDPD with an SFQ flux generator and SFQ comparator, which can speed up the detection and guarantees the necessary phase locking during the operations. The results motivated us to prepare a chip layout in which this compatibility is explored and it will be tested experimentally very soon.

The JDPD is indicated to perform a digital readout of superconducting qubits. This task can be performed very efficiently by sending a readout pulse at the frequency of the bare resonator ω_r , where the readout tone encodes the information on the qubit state in its phase.

Therefore, we propose this device as part of a more complex architecture, in which the classical qubit control, measurement, and data processing are performed by a classical SFQ processor. This approach can be a valid solution to enhance the scalability of superconducting quantum systems, which remains a big engineering challenge to realize practical error-corrected quantum computers.

Bibliography

- [1] John Clarke and Frank K. Wilhelm. “Superconducting quantum bits”. In: *Nature* 453 (June 2008), pp. 1031–1042. ISSN: 1476-4687. DOI: [10.1038/nature07128](https://doi.org/10.1038/nature07128).
- [2] R. Barends et al. “Superconducting quantum circuits at the surface code threshold for fault tolerance”. In: *Nature* 508 (Apr. 2014), pp. 500–503. ISSN: 1476-4687. DOI: [10.1038/nature13171](https://doi.org/10.1038/nature13171).
- [3] Chuan-Hong Liu et al. “Single Flux Quantum-Based Digital Control of Superconducting Qubits in a Multi-Chip Module”. In: *arXiv* (Jan. 2023). DOI: [10.48550/arXiv.2301.05696](https://doi.org/10.48550/arXiv.2301.05696). eprint: [2301.05696](https://arxiv.org/abs/2301.05696).
- [4] T. Walter et al. “Rapid High-Fidelity Single-Shot Dispersive Readout of Superconducting Qubits”. In: *Phys. Rev. Appl.* 7 (5 May 2017), p. 054020. DOI: [10.1103/PhysRevApplied.7.054020](https://doi.org/10.1103/PhysRevApplied.7.054020). URL: <https://link.aps.org/doi/10.1103/PhysRevApplied.7.054020>.
- [5] Austin G. Fowler et al. “Surface codes: Towards practical large-scale quantum computation”. In: *Phys. Rev. A* 86 (3 Sept. 2012), p. 032324. DOI: [10.1103/PhysRevA.86.032324](https://doi.org/10.1103/PhysRevA.86.032324). URL: <https://link.aps.org/doi/10.1103/PhysRevA.86.032324>.
- [6] Frank Arute et al. “Quantum supremacy using a programmable superconducting processor”. In: *Nature* 574 (Oct. 2019), pp. 505–510. ISSN: 1476-4687. DOI: [10.1038/s41586-019-1666-5](https://doi.org/10.1038/s41586-019-1666-5).
- [7] Sebastian Krinner et al. “Realizing repeated quantum error correction in a distance-three surface code”. In: *Nature* 605 (May 2022), pp. 669–674. ISSN: 1476-4687. DOI: [10.1038/s41586-022-04566-8](https://doi.org/10.1038/s41586-022-04566-8).
- [8] Youwei Zhao et al. “Realization of an Error-Correcting Surface Code with Superconducting Qubits”. In: *Phys. Rev. Lett.* 129 (3 July 2022), p. 030501. DOI: [10.1103/PhysRevLett.129.030501](https://doi.org/10.1103/PhysRevLett.129.030501). URL: <https://link.aps.org/doi/10.1103/PhysRevLett.129.030501>.
- [9] O. Mukhanov et al. “Scalable Quantum Computing Infrastructure Based on Superconducting Electronics”. In: *2019 IEEE International Electron Devices Meeting (IEDM)*. 2019, pp. 31.2.1–31.2.4. DOI: [10.1109/IEDM19573.2019.8993634](https://doi.org/10.1109/IEDM19573.2019.8993634).

- [10] R. McDermott et al. “Quantum–classical interface based on single flux quantum digital logic”. In: *Quantum Sci. Technol.* 3.2 (Jan. 2018), p. 024004. ISSN: 2058-9565. DOI: [10.1088/2058-9565/aaa3a0](https://doi.org/10.1088/2058-9565/aaa3a0).
- [11] Meraj Ahmad et al. “Scalable Cryoelectronics for Superconducting Qubit Control and Readout”. In: *Adv. Intell. Syst.* 4.9 (Sept. 2022), p. 2200079. ISSN: 2640-4567. DOI: [10.1002/aisy.202200079](https://doi.org/10.1002/aisy.202200079).
- [12] Oleg A. Mukhanov. “Energy-Efficient Single Flux Quantum Technology”. In: *IEEE Transactions on Applied Superconductivity* 21.3 (2011), pp. 760–769. DOI: [10.1109/TASC.2010.2096792](https://doi.org/10.1109/TASC.2010.2096792).
- [13] D. E. Kirichenko, S. Sarwana, and A. F. Kirichenko. “Zero Static Power Dissipation Biasing of RSFQ Circuits”. In: *IEEE Transactions on Applied Superconductivity* 21.3 (2011), pp. 776–779. DOI: [10.1109/TASC.2010.2098432](https://doi.org/10.1109/TASC.2010.2098432).
- [14] E. Leonard et al. “Digital Coherent Control of a Superconducting Qubit”. In: *Phys. Rev. Appl.* 11 (1 Jan. 2019), p. 014009. DOI: [10.1103/PhysRevApplied.11.014009](https://doi.org/10.1103/PhysRevApplied.11.014009). URL: <https://link.aps.org/doi/10.1103/PhysRevApplied.11.014009>.
- [15] Kangbo Li, R. McDermott, and Maxim G. Vavilov. “Hardware-Efficient Qubit Control with Single-Flux-Quantum Pulse Sequences”. In: *Phys. Rev. Appl.* 12 (1 July 2019), p. 014044. DOI: [10.1103/PhysRevApplied.12.014044](https://doi.org/10.1103/PhysRevApplied.12.014044). URL: <https://link.aps.org/doi/10.1103/PhysRevApplied.12.014044>.
- [16] K.K. Likharev and V.K. Semenov. “RSFQ logic/memory family: a new Josephson-junction technology for sub-terahertz-clock-frequency digital systems”. In: *IEEE Transactions on Applied Superconductivity* 1.1 (1991), pp. 3–28. DOI: [10.1109/77.80745](https://doi.org/10.1109/77.80745).
- [17] *PSCAN2 Superconducting circuit simulator*.
- [18] P. D. Nation & J. R. Johansson. *QuTiP - Quantum Toolbox in Python*. [Online; accessed 8. Sep. 2022]. July 2022. URL: <https://qutip.org/citing.html>.
- [19] Nicolas Gisin and Rob Thew. “Quantum communication”. In: *Nat. Photonics* 1 (Mar. 2007), pp. 165–171. ISSN: 1749-4893. DOI: [10.1038/nphoton.2007.22](https://doi.org/10.1038/nphoton.2007.22).
- [20] C. L. Degen, F. Reinhard, and P. Cappellaro. “Quantum sensing”. In: *Rev. Mod. Phys.* 89.3 (July 2017), p. 035002. ISSN: 1539-0756. DOI: [10.1103/RevModPhys.89.035002](https://doi.org/10.1103/RevModPhys.89.035002).
- [21] G. Wendin. “Quantum information processing with superconducting circuits: a review”. In: *Rep. Prog. Phys.* 80.10 (Sept. 2017), p. 106001. ISSN: 0034-4885. DOI: [10.1088/1361-6633/aa7e1a](https://doi.org/10.1088/1361-6633/aa7e1a).
- [22] J. I. Cirac and P. Zoller. “Quantum Computations with Cold Trapped Ions”. In: *Phys. Rev. Lett.* 74.20 (May 1995), pp. 4091–4094. ISSN: 1079-7114. DOI: [10.1103/PhysRevLett.74.4091](https://doi.org/10.1103/PhysRevLett.74.4091).

-
- [23] D. Leibfried et al. “Quantum dynamics of single trapped ions”. In: *Rev. Mod. Phys.* 75 (1 Mar. 2003), pp. 281–324. DOI: [10.1103/RevModPhys.75.281](https://doi.org/10.1103/RevModPhys.75.281). URL: <https://link.aps.org/doi/10.1103/RevModPhys.75.281>.
- [24] D. Porras and J. I. Cirac. “Effective Quantum Spin Systems with Trapped Ions”. In: *Phys. Rev. Lett.* 92 (20 May 2004), p. 207901. DOI: [10.1103/PhysRevLett.92.207901](https://doi.org/10.1103/PhysRevLett.92.207901). URL: <https://link.aps.org/doi/10.1103/PhysRevLett.92.207901>.
- [25] R. Blatt and David Wineland. “Entangled States of Trapped Atomic Ions”. In: *Nature* 453 (July 2008), pp. 1008–15. DOI: [10.1038/nature07125](https://doi.org/10.1038/nature07125).
- [26] Maciej Lewenstein et al. “Ultracold atomic gases in optical lattices: mimicking condensed matter physics and beyond”. In: *Advances in Physics* 56.2 (Mar. 2007), pp. 243–379. DOI: [10.1080/00018730701223200](https://doi.org/10.1080/00018730701223200). URL: <https://doi.org/10.1080%2F00018730701223200>.
- [27] Immanuel Bloch, Jean Dalibard, and Wilhelm Zwerger. “Many-body physics with ultracold gases”. In: *Rev. Mod. Phys.* 80 (3 July 2008), pp. 885–964. DOI: [10.1103/RevModPhys.80.885](https://doi.org/10.1103/RevModPhys.80.885). URL: <https://link.aps.org/doi/10.1103/RevModPhys.80.885>.
- [28] Christian Gross and Immanuel Bloch. “Quantum simulations with ultracold atoms in optical lattices”. In: *Science* 357.6355 (Sept. 2017), pp. 995–1001. ISSN: 0036-8075. DOI: [10.1126/science.aal3837](https://doi.org/10.1126/science.aal3837).
- [29] Daniel Loss and David P. DiVincenzo. “Quantum computation with quantum dots”. In: *Phys. Rev. A* 57.1 (Jan. 1998), pp. 120–126. ISSN: 2469-9934. DOI: [10.1103/PhysRevA.57.120](https://doi.org/10.1103/PhysRevA.57.120).
- [30] B. E. Kane. “A silicon-based nuclear spin quantum computer”. In: *Nature* 393 (May 1998), pp. 133–137. ISSN: 1476-4687. DOI: [10.1038/30156](https://doi.org/10.1038/30156).
- [31] Rogerio de Sousa, J. D. Delgado, and S. Das Sarma. “Silicon quantum computation based on magnetic dipolar coupling”. In: *Phys. Rev. A* 70 (5 Nov. 2004), p. 052304. DOI: [10.1103/PhysRevA.70.052304](https://doi.org/10.1103/PhysRevA.70.052304). URL: <https://link.aps.org/doi/10.1103/PhysRevA.70.052304>.
- [32] A. Imamoglu et al. “Quantum Information Processing Using Quantum Dot Spins and Cavity QED”. In: *Phys. Rev. Lett.* 83 (20 Nov. 1999), pp. 4204–4207. DOI: [10.1103/PhysRevLett.83.4204](https://doi.org/10.1103/PhysRevLett.83.4204). URL: <https://link.aps.org/doi/10.1103/PhysRevLett.83.4204>.
- [33] Dirk Englund et al. “Controlling the Spontaneous Emission Rate of Single Quantum Dots in a Two-Dimensional Photonic Crystal”. In: *Phys. Rev. Lett.* 95 (1 July 2005), p. 013904. DOI: [10.1103/PhysRevLett.95.013904](https://doi.org/10.1103/PhysRevLett.95.013904). URL: <https://link.aps.org/doi/10.1103/PhysRevLett.95.013904>.
- [34] J. R. Petta et al. “Coherent Manipulation of Coupled Electron Spins in Semiconductor Quantum Dots”. In: *Science* 309.5744 (Sept. 2005), pp. 2180–2184. ISSN: 0036-8075. DOI: [10.1126/science.1116955](https://doi.org/10.1126/science.1116955).

- [35] M. V. Gurudev Dutt et al. “Quantum Register Based on Individual Electronic and Nuclear Spin Qubits in Diamond”. In: *Science* 316.5829 (June 2007), pp. 1312–1316. ISSN: 0036-8075. DOI: [10.1126/science.1139831](https://doi.org/10.1126/science.1139831).
- [36] R. Hanson, O. Gywat, and D. D. Awschalom. “Room-temperature manipulation and decoherence of a single spin in diamond”. In: *Phys. Rev. B* 74 (16 Oct. 2006), p. 161203. DOI: [10.1103/PhysRevB.74.161203](https://doi.org/10.1103/PhysRevB.74.161203). URL: <https://link.aps.org/doi/10.1103/PhysRevB.74.161203>.
- [37] E. Knill, R. Laflamme, and G. J. Milburn. “A scheme for efficient quantum computation with linear optics”. In: *Nature* 409 (Jan. 2001), pp. 46–52. ISSN: 1476-4687. DOI: [10.1038/35051009](https://doi.org/10.1038/35051009).
- [38] T. B. Pittman, B. C. Jacobs, and J. D. Franson. “Probabilistic quantum logic operations using polarizing beam splitters”. In: *Phys. Rev. A* 64 (6 Nov. 2001), p. 062311. DOI: [10.1103/PhysRevA.64.062311](https://doi.org/10.1103/PhysRevA.64.062311). URL: <https://link.aps.org/doi/10.1103/PhysRevA.64.062311>.
- [39] J. D. Franson et al. “High-Fidelity Quantum Logic Operations Using Linear Optical Elements”. In: *Phys. Rev. Lett.* 89 (13 Sept. 2002), p. 137901. DOI: [10.1103/PhysRevLett.89.137901](https://doi.org/10.1103/PhysRevLett.89.137901). URL: <https://link.aps.org/doi/10.1103/PhysRevLett.89.137901>.
- [40] Andreas Wallraff et al. “Strong coupling of a single photon to a superconducting qubit using circuit quantum electrodynamics”. In: *Nature* 431 (Oct. 2004), pp. 162–7. DOI: [10.1038/nature02851](https://doi.org/10.1038/nature02851).
- [41] M. H. Devoret, A. Wallraff, and J. M. Martinis. “Superconducting Qubits: A Short Review”. In: (2004). DOI: [10.48550/ARXIV.COND-MAT/0411174](https://doi.org/10.48550/ARXIV.COND-MAT/0411174). URL: <https://arxiv.org/abs/cond-mat/0411174>.
- [42] Uri Vool and Michel Devoret. “Introduction to quantum electromagnetic circuits”. In: *International Journal of Circuit Theory and Applications* 45.7 (June 2017), pp. 897–934. DOI: [10.1002/cta.2359](https://doi.org/10.1002/cta.2359). URL: <https://doi.org/10.1002/cta.2359>.
- [43] D. Massarotti et al. “Macroscopic quantum tunnelling in spin filter ferromagnetic Josephson junctions”. In: *Nat. Commun.* 6.7376 (June 2015), pp. 1–6. ISSN: 2041-1723. DOI: [10.1038/ncomms8376](https://doi.org/10.1038/ncomms8376).
- [44] A.O Caldeira and A.J Leggett. “Quantum tunnelling in a dissipative system”. In: *Annals of Physics* 149.2 (1983), pp. 374–456. ISSN: 0003-4916. DOI: [https://doi.org/10.1016/0003-4916\(83\)90202-6](https://doi.org/10.1016/0003-4916(83)90202-6). URL: <https://www.sciencedirect.com/science/article/pii/0003491683902026>.
- [45] A. J. Leggett and Anupam Garg. “Quantum mechanics versus macroscopic realism: Is the flux there when nobody looks?” In: *Phys. Rev. Lett.* 54 (9 Mar. 1985), pp. 857–860. DOI: [10.1103/PhysRevLett.54.857](https://doi.org/10.1103/PhysRevLett.54.857). URL: <https://link.aps.org/doi/10.1103/PhysRevLett.54.857>.
- [46] F. Tafuri. “Fundamentals and Frontiers of the Josephson Effect”. In: Springer Series in Materials Science, 2019. Chap. 7.4, pp. 248–253.

- [47] A. Barone and G. Paterno. “Physics and Applications of the Josephson effect”. In: John Wiley Sons, Inc. Publishers, 1982. Chap. 2, pp. 25–49.
- [48] K.K.Likharev. “Dynamics of Josephson junctions and circuits”. In: Gordon and Breach Science Publishers, 1986. Chap. 2.3, pp. 49–53.
- [49] B. D. Josephson. “Possible new effects in superconductive tunnelling”. In: *Physics Letters* 1.7 (July 1962), pp. 251–253. ISSN: 0031-9163. DOI: [10.1016/0031-9163\(62\)91369-0](https://doi.org/10.1016/0031-9163(62)91369-0).
- [50] Halima Giovanna Ahmad et al. “Critical Current Suppression in Spin-Filter Josephson Junctions”. In: *J. Supercond. Novel Magn.* 33.10 (Oct. 2020), pp. 3043–3049. ISSN: 1557-1947. DOI: [10.1007/s10948-020-05577-0](https://doi.org/10.1007/s10948-020-05577-0).
- [51] M. Steffen et al. “Quantum computing: An IBM perspective”. In: *IBM Journal of Research and Development* 55.5 (2011), 13:1–13:11. DOI: [10.1147/JRD.2011.2165678](https://doi.org/10.1147/JRD.2011.2165678).
- [52] Michel H. Devoret and John M. Martinis. “Implementing Qubits with Superconducting Integrated Circuits”. In: *Quantum Inf. Process.* 3.1 (Oct. 2004), pp. 163–203. ISSN: 1573-1332. DOI: [10.1007/s11128-004-3101-5](https://doi.org/10.1007/s11128-004-3101-5).
- [53] G. Wendin and V. S. Shumeiko. “Superconducting Quantum Circuits, Qubits and Computing”. In: *arXiv* (Aug. 2005). DOI: [10.48550/arXiv.cond-mat/0508729](https://doi.org/10.48550/arXiv.cond-mat/0508729). eprint: [cond-mat/0508729](https://arxiv.org/abs/cond-mat/0508729).
- [54] Xiu Gu et al. “Microwave photonics with superconducting quantum circuits”. In: *Physics Reports* 718-719 (2017). Microwave photonics with superconducting quantum circuits, pp. 1–102. ISSN: 0370-1573. DOI: <https://doi.org/10.1016/j.physrep.2017.10.002>. URL: <https://www.sciencedirect.com/science/article/pii/S0370157317303290>.
- [55] Morten Kjaergaard et al. “Superconducting Qubits: Current State of Play”. In: *Annu. Rev. Condens. Matter Phys.* 11.1 (Mar. 2020), pp. 369–395. ISSN: 1947-5454. DOI: [10.1146/annurev-conmatphys-031119-050605](https://doi.org/10.1146/annurev-conmatphys-031119-050605).
- [56] Feng Bao et al. “Fluxonium: An Alternative Qubit Platform for High-Fidelity Operations”. In: *Phys. Rev. Lett.* 129 (1 June 2022), p. 010502. DOI: [10.1103/PhysRevLett.129.010502](https://doi.org/10.1103/PhysRevLett.129.010502). URL: <https://link.aps.org/doi/10.1103/PhysRevLett.129.010502>.
- [57] Quentin Ficheux et al. “Fast Logic with Slow Qubits: Microwave-Activated Controlled-Z Gate on Low-Frequency Fluxoniums”. In: *Phys. Rev. X* 11 (2 May 2021), p. 021026. DOI: [10.1103/PhysRevX.11.021026](https://doi.org/10.1103/PhysRevX.11.021026). URL: <https://link.aps.org/doi/10.1103/PhysRevX.11.021026>.
- [58] Haonan Xiong et al. “Arbitrary controlled-phase gate on fluxonium qubits using differential ac Stark shifts”. In: *Phys. Rev. Res.* 4 (2 Apr. 2022), p. 023040. DOI: [10.1103/PhysRevResearch.4.023040](https://doi.org/10.1103/PhysRevResearch.4.023040). URL: <https://link.aps.org/doi/10.1103/PhysRevResearch.4.023040>.

- [59] Jens Koch et al. “Charge-insensitive qubit design derived from the Cooper pair box”. In: *Phys. Rev. A* 76 (4 Oct. 2007), p. 042319. DOI: [10.1103/PhysRevA.76.042319](https://doi.org/10.1103/PhysRevA.76.042319). URL: <https://link.aps.org/doi/10.1103/PhysRevA.76.042319>.
- [60] Chenlu Wang et al. “Towards practical quantum computers: transmon qubit with a lifetime approaching 0.5 milliseconds”. In: *npj Quantum Inf.* 8.3 (Jan. 2022), pp. 1–6. ISSN: 2056-6387. DOI: [10.1038/s41534-021-00510-2](https://doi.org/10.1038/s41534-021-00510-2).
- [61] A. A. Houck et al. “Controlling the Spontaneous Emission of a Superconducting Transmon Qubit”. In: *Phys. Rev. Lett.* 101 (8 Aug. 2008), p. 080502. DOI: [10.1103/PhysRevLett.101.080502](https://doi.org/10.1103/PhysRevLett.101.080502). URL: <https://link.aps.org/doi/10.1103/PhysRevLett.101.080502>.
- [62] Matthias Steffen et al. “Quantum information storage using tunable flux qubits”. In: *Journal of Physics: Condensed Matter* 22.5 (Jan. 2010), p. 053201. DOI: [10.1088/0953-8984/22/5/053201](https://doi.org/10.1088/0953-8984/22/5/053201). URL: <https://dx.doi.org/10.1088/0953-8984/22/5/053201>.
- [63] L. DiCarlo et al. “Demonstration of two-qubit algorithms with a superconducting quantum processor”. In: *Nature* 460 (July 2009), pp. 240–244. ISSN: 1476-4687. DOI: [10.1038/nature08121](https://doi.org/10.1038/nature08121).
- [64] J. A. Schreier et al. “Suppressing charge noise decoherence in superconducting charge qubits”. In: *Phys. Rev. B* 77 (18 May 2008), p. 180502. DOI: [10.1103/PhysRevB.77.180502](https://doi.org/10.1103/PhysRevB.77.180502). URL: <https://link.aps.org/doi/10.1103/PhysRevB.77.180502>.
- [65] V. A. Sevriuk et al. “Fast control of dissipation in a superconducting resonator”. In: *Appl. Phys. Lett.* 115.8 (Aug. 2019), p. 082601. ISSN: 0003-6951. DOI: [10.1063/1.5116659](https://doi.org/10.1063/1.5116659).
- [66] A. Megrant et al. “Planar superconducting resonators with internal quality factors above one million”. In: *Appl. Phys. Lett.* 100.11 (Mar. 2012), p. 113510. ISSN: 0003-6951. DOI: [10.1063/1.3693409](https://doi.org/10.1063/1.3693409).
- [67] D. C. Mattis and J. Bardeen. “Theory of the Anomalous Skin Effect in Normal and Superconducting Metals”. In: *Phys. Rev.* 111 (2 July 1958), pp. 412–417. DOI: [10.1103/PhysRev.111.412](https://doi.org/10.1103/PhysRev.111.412). URL: <https://link.aps.org/doi/10.1103/PhysRev.111.412>.
- [68] Sergio Boixo et al. “Evidence for quantum annealing with more than one hundred qubits”. In: *Nat. Phys.* 10 (Mar. 2014), pp. 218–224. ISSN: 1745-2481. DOI: [10.1038/nphys2900](https://doi.org/10.1038/nphys2900).
- [69] P. Krantz et al. “A quantum engineer’s guide to superconducting qubits”. In: *Appl. Phys. Rev.* 6.2 (June 2019), p. 021318. ISSN: 1931-9401. DOI: [10.1063/1.5089550](https://doi.org/10.1063/1.5089550).
- [70] Jerry M. Chow et al. “Implementing a strand of a scalable fault-tolerant quantum computing fabric”. In: *Nat. Commun.* 5.4015 (June 2014), pp. 1–9. ISSN: 2041-1723. DOI: [10.1038/ncomms5015](https://doi.org/10.1038/ncomms5015).

-
- [71] D. A. Buck. “The Cryotron-A Superconductive Computer Component”. In: *Proceedings of the IRE* 44 (1956), pp. 482–493.
- [72] M.B. Ketchen et al. “A Josephson technology system level experiment”. In: *IEEE Electron Device Letters* 2.10 (1981), pp. 262–265. DOI: [10.1109/EDL.1981.25426](https://doi.org/10.1109/EDL.1981.25426).
- [73] Hisao Hayakawa. “Josephson Computer Technology”. In: *Phys. Today* 39.3 (Jan. 2008), p. 46. ISSN: 0031-9228. DOI: [10.1063/1.881055](https://doi.org/10.1063/1.881055).
- [74] Paul Bunyk, Konstantin Likharev, and Dmitry Zinoviev. *RSFQ technology: Physics and devices*. Vol. 11. Mar. 2001. ISBN: 978-981-02-4638-9. DOI: [10.1142/S012915640100085X](https://doi.org/10.1142/S012915640100085X).
- [75] K.K. Likharev, O.A. Mukhanov, and V.K. Semenov. “RESISTIVE SINGLE FLUX QUANTUM LOGIC FOR THE JOSEPHSON-JUNCTION DIGITAL TECHNOLOGY”. In: *Proceedings of the Third International Conference on Superconducting Quantum Devices, Berlin (West), June 25-28, 1985*. Ed. by Hans-D. Hahlbohm and Heinz Lübbig. Berlin, Boston: De Gruyter, 1986, pp. 1103–1108. ISBN: 9783110862393. DOI: [doi:10.1515/9783110862393.1103](https://doi.org/10.1515/9783110862393.1103). URL: <https://doi.org/10.1515/9783110862393.1103>.
- [76] Oleg A. Mukhanov, Vasili K. Semenov, and Konstantin K. Likharev. “Ultimate performance of the RSFQ logic circuits”. In: *IEEE Transactions on Magnetics* 23 (1987), pp. 759–762.
- [77] W. Chen et al. “Rapid single flux quantum T-flip flop operating up to 770 GHz”. In: *IEEE Transactions on Applied Superconductivity* 9.2 (1999), pp. 3212–3215. DOI: [10.1109/77.783712](https://doi.org/10.1109/77.783712).
- [78] R. McDermott and M. G. Vavilov. “Accurate Qubit Control with Single Flux Quantum Pulses”. In: *Phys. Rev. Applied* 2 (1 July 2014), p. 014007. DOI: [10.1103/PhysRevApplied.2.014007](https://doi.org/10.1103/PhysRevApplied.2.014007). URL: <https://link.aps.org/doi/10.1103/PhysRevApplied.2.014007>.
- [79] A. Opremcak et al. “Measurement of a superconducting qubit with a microwave photon counter”. In: *Science* 361.6408 (Sept. 2018), pp. 1239–1242. ISSN: 0036-8075. DOI: [10.1126/science.aat4625](https://doi.org/10.1126/science.aat4625).
- [80] A. Opremcak et al. “High-Fidelity Measurement of a Superconducting Qubit Using an On-Chip Microwave Photon Counter”. In: *Phys. Rev. X* 11.1 (Feb. 2021), p. 011027. ISSN: 2160-3308. DOI: [10.1103/PhysRevX.11.011027](https://doi.org/10.1103/PhysRevX.11.011027).
- [81] Caleb Howington et al. “Interfacing Superconducting Qubits With Cryogenic Logic: Readout”. In: *IEEE Transactions on Applied Superconductivity* 29.5 (2019), pp. 1–5. DOI: [10.1109/TASC.2019.2908884](https://doi.org/10.1109/TASC.2019.2908884).
- [82] John Preskill. “FAULT-TOLERANT QUANTUM COMPUTATION”. In: *Introduction to Quantum Computation and Information*. Singapore: WORLD SCIENTIFIC, Oct. 1998, pp. 213–269. ISBN: 978-981-02-3399-0. DOI: [10.1142/9789812385253_0008](https://doi.org/10.1142/9789812385253_0008).

- [83] M. D. Reed et al. “High-Fidelity Readout in Circuit Quantum Electrodynamics Using the Jaynes-Cummings Nonlinearity”. In: *Phys. Rev. Lett.* 105 (17 Oct. 2010), p. 173601. DOI: [10.1103/PhysRevLett.105.173601](https://doi.org/10.1103/PhysRevLett.105.173601). URL: <https://link.aps.org/doi/10.1103/PhysRevLett.105.173601>.
- [84] O. Astafiev et al. “Single-shot measurement of the Josephson charge qubit”. In: *Phys. Rev. B* 69 (18 May 2004), p. 180507. DOI: [10.1103/PhysRevB.69.180507](https://doi.org/10.1103/PhysRevB.69.180507). URL: <https://link.aps.org/doi/10.1103/PhysRevB.69.180507>.
- [85] Y. Nakamura, Yu. A. Pashkin, and J. S. Tsai. “Coherent control of macroscopic quantum states in a single-Cooper-pair box”. In: *Nature* 398 (Apr. 1999), pp. 786–788. ISSN: 1476-4687. DOI: [10.1038/19718](https://doi.org/10.1038/19718).
- [86] Caspar H. van der Wal et al. “Quantum Superposition of Macroscopic Persistent-Current States”. In: *Science* 290.5492 (Oct. 2000), pp. 773–777. ISSN: 0036-8075. DOI: [10.1126/science.290.5492.773](https://doi.org/10.1126/science.290.5492.773).
- [87] J. E. Mooij et al. “Josephson Persistent-Current Qubit”. In: *Science* 285.5430 (Aug. 1999), pp. 1036–1039. ISSN: 0036-8075. DOI: [10.1126/science.285.5430.1036](https://doi.org/10.1126/science.285.5430.1036).
- [88] John M. Martinis et al. “Rabi Oscillations in a Large Josephson-Junction Qubit”. In: *Phys. Rev. Lett.* 89 (11 Aug. 2002), p. 117901. DOI: [10.1103/PhysRevLett.89.117901](https://doi.org/10.1103/PhysRevLett.89.117901). URL: <https://link.aps.org/doi/10.1103/PhysRevLett.89.117901>.
- [89] Alexandre Blais et al. “Cavity quantum electrodynamics for superconducting electrical circuits: An architecture for quantum computation”. In: *Phys. Rev. A* 69 (6 June 2004), p. 062320. DOI: [10.1103/PhysRevA.69.062320](https://doi.org/10.1103/PhysRevA.69.062320). URL: <https://link.aps.org/doi/10.1103/PhysRevA.69.062320>.
- [90] Jay Gambetta et al. “Quantum trajectory approach to circuit QED: Quantum jumps and the Zeno effect”. In: *Phys. Rev. A* 77 (1 Jan. 2008), p. 012112. DOI: [10.1103/PhysRevA.77.012112](https://doi.org/10.1103/PhysRevA.77.012112). URL: <https://link.aps.org/doi/10.1103/PhysRevA.77.012112>.
- [91] Maxime Boissonneault, J. M. Gambetta, and Alexandre Blais. “Dispersive regime of circuit QED: Photon-dependent qubit dephasing and relaxation rates”. In: *Phys. Rev. A* 79.1 (Jan. 2009), p. 013819. ISSN: 2469-9934. DOI: [10.1103/PhysRevA.79.013819](https://doi.org/10.1103/PhysRevA.79.013819).
- [92] Mahdi Naghiloo. “Introduction to Experimental Quantum Measurement with Superconducting Qubits”. In: *arXiv* (Apr. 2019). DOI: [10.48550/arXiv.1904.09291](https://doi.org/10.48550/arXiv.1904.09291). eprint: [1904.09291](https://arxiv.org/abs/1904.09291).
- [93] Caleb Jordan Howington. “Digital Readout and Control of a Superconducting Qubit”. In: *PhD dissertation, Syracuse University* (2019). URL: <https://surface.syr.edu/etd/1121>.

-
- [94] R. Vijay, D. H. Slichter, and I. Siddiqi. “Observation of Quantum Jumps in a Superconducting Artificial Atom”. In: *Phys. Rev. Lett.* 106 (11 Mar. 2011), p. 110502. DOI: [10.1103/PhysRevLett.106.110502](https://doi.org/10.1103/PhysRevLett.106.110502). URL: <https://link.aps.org/doi/10.1103/PhysRevLett.106.110502>.
- [95] Byeong Ho Eom et al. “A wideband, low-noise superconducting amplifier with high dynamic range”. In: *Nat. Phys.* 8 (Aug. 2012), pp. 623–627. ISSN: 1745-2481. DOI: [10.1038/nphys2356](https://doi.org/10.1038/nphys2356).
- [96] J. Y. Mutus et al. “Strong environmental coupling in a Josephson parametric amplifier”. In: *Appl. Phys. Lett.* 104.26 (June 2014), p. 263513. ISSN: 0003-6951. DOI: [10.1063/1.4886408](https://doi.org/10.1063/1.4886408).
- [97] C. Macklin et al. “A near-quantum-limited Josephson traveling-wave parametric amplifier”. In: *Science* 350.6258 (Oct. 2015), pp. 307–310. ISSN: 0036-8075. DOI: [10.1126/science.aaa8525](https://doi.org/10.1126/science.aaa8525).
- [98] Luke C. G. Govia et al. “High-fidelity qubit measurement with a microwave-photon counter”. In: *Phys. Rev. A* 90 (6 Dec. 2014), p. 062307. DOI: [10.1103/PhysRevA.90.062307](https://doi.org/10.1103/PhysRevA.90.062307). URL: <https://link.aps.org/doi/10.1103/PhysRevA.90.062307>.
- [99] J. Martinis. “Superconducting phase qubits”. In: *Quantum Inf. Process.* (2009). URL: <https://www.semanticscholar.org/paper/Superconducting-phase-qubits-Martinis/3dae37a31c5082425b0a2801b3a1fc5b096b6b0b>.
- [100] Dmitri V. Averin, Kristian Rabenstein, and Vasili K. Semenov. “Rapid ballistic readout for flux qubits”. In: *Phys. Rev. B* 73 (9 Mar. 2006), p. 094504. DOI: [10.1103/PhysRevB.73.094504](https://doi.org/10.1103/PhysRevB.73.094504). URL: <https://link.aps.org/doi/10.1103/PhysRevB.73.094504>.
- [101] Caspar H. van der Wal et al. “Quantum Superposition of Macroscopic Persistent-Current States”. In: *Science* 290.5492 (Oct. 2000), pp. 773–777. ISSN: 0036-8075. DOI: [10.1126/science.290.5492.773](https://doi.org/10.1126/science.290.5492.773).
- [102] Arkady Fedorov et al. “Reading out the state of a flux qubit by Josephson transmission line solitons”. In: *Phys. Rev. B* 75 (22 June 2007), p. 224504. DOI: [10.1103/PhysRevB.75.224504](https://doi.org/10.1103/PhysRevB.75.224504). URL: <https://link.aps.org/doi/10.1103/PhysRevB.75.224504>.
- [103] Anna Herr et al. “Design of a ballistic fluxon qubit readout”. In: *Supercond. Sci. Technol* 20 (Nov. 2007), pp. 450–454. DOI: [10.1088/0953-2048/20/11/S29](https://doi.org/10.1088/0953-2048/20/11/S29).
- [104] I. I. Soloviev et al. “Symmetrical Josephson vortex interferometer as an advanced ballistic single-shot detector”. In: *Appl. Phys. Lett.* 105.20 (Nov. 2014), p. 202602. ISSN: 0003-6951. DOI: [10.1063/1.4902327](https://doi.org/10.1063/1.4902327).
- [105] I. I. Soloviev et al. “Soliton scattering as a measurement tool for weak signals”. In: *Phys. Rev. B* 92 (1 July 2015), p. 014516. DOI: [10.1103/PhysRevB.92.014516](https://doi.org/10.1103/PhysRevB.92.014516). URL: <https://link.aps.org/doi/10.1103/PhysRevB.92.014516>.

- [106] I. I. Soloviev et al. “Soliton scattering as a measurement tool for weak signals”. In: *Phys. Rev. B* 92 (1 July 2015), p. 014516. DOI: [10.1103/PhysRevB.92.014516](https://doi.org/10.1103/PhysRevB.92.014516). URL: <https://link.aps.org/doi/10.1103/PhysRevB.92.014516>.
- [107] N. V. Klenov et al. “Flux qubit interaction with rapid single-flux quantum logic circuits: Control and readout”. In: *Low Temp. Phys.* 43.7 (July 2017), pp. 789–798. ISSN: 1063-777X. DOI: [10.1063/1.4995627](https://doi.org/10.1063/1.4995627).
- [108] Kirill G. Fedorov et al. “Fluxon Readout of a Superconducting Qubit”. In: *Phys. Rev. Lett.* 112 (16 Apr. 2014), p. 160502. DOI: [10.1103/PhysRevLett.112.160502](https://doi.org/10.1103/PhysRevLett.112.160502). URL: <https://link.aps.org/doi/10.1103/PhysRevLett.112.160502>.
- [109] Thomas J. Walls, Timur V. Filippov, and Konstantin K. Likharev. “Quantum Fluctuations in Josephson Junction Comparators”. In: *Phys. Rev. Lett.* 89 (21 Nov. 2002), p. 217004. DOI: [10.1103/PhysRevLett.89.217004](https://doi.org/10.1103/PhysRevLett.89.217004). URL: <https://link.aps.org/doi/10.1103/PhysRevLett.89.217004>.
- [110] Thomas J. Walls, Dmitri V. Averin, and Konstantin K. Likharev. “Josephson Junction Comparator as a Quantum-Limited Detector for Flux Qubit Readout”. In: *IEEE Trans. Appl. Supercond.* 17.2 (June 2007), pp. 136–141. ISSN: 1558-2515. DOI: [10.1109/TASC.2007.898632](https://doi.org/10.1109/TASC.2007.898632).
- [111] Tom Ohki et al. “Balanced Comparator for RSFQ Qubit Readout”. In: *IEEE Transactions on Applied Superconductivity* 17.2 (2007), pp. 128–131. DOI: [10.1109/TASC.2007.897319](https://doi.org/10.1109/TASC.2007.897319).
- [112] H. Ko and T. Van Duzer. “A new high-speed periodic-threshold comparator for use in a Josephson A/D converter”. In: *IEEE Journal of Solid-State Circuits* 23.4 (1988), pp. 1017–1021. DOI: [10.1109/4.355](https://doi.org/10.1109/4.355).
- [113] P. Bradley and H. Dang. “Design and testing of quasi-one junction SQUID-based comparators at low and high speed for superconductive flash A/D convertors”. In: *IEEE Transactions on Applied Superconductivity* 1.3 (1991), pp. 134–139. DOI: [10.1109/77.84627](https://doi.org/10.1109/77.84627).
- [114] D.K. Brock et al. “Design and testing of QOS comparators for an RSFQ based analog to digital converter”. In: *IEEE Transactions on Applied Superconductivity* 5.2 (1995), pp. 2244–2247. DOI: [10.1109/77.403032](https://doi.org/10.1109/77.403032).
- [115] K. Loe and E. Goto. “Analysis of flux input and output Josephson pair device”. In: *IEEE Transactions on Magnetism* 21.2 (1985), pp. 884–887. DOI: [10.1109/TMAG.1985.1063734](https://doi.org/10.1109/TMAG.1985.1063734).
- [116] Mutsumi Hosoya et al. “Quantum flux parametron: a single quantum flux device for Josephson supercomputer”. In: *IEEE Transactions on Applied Superconductivity* 1.2 (1991), pp. 77–89.
- [117] Yutaka Harada et al. “Basic operations of the quantum flux parametron”. In: *IEEE transactions on magnetism* 23.5 (1987), pp. 3801–3807.

-
- [118] Naoki Takeuchi et al. “Adiabatic Quantum-Flux-Parametron: A Tutorial Review”. In: *IEICE Trans. Electron.* E105-C.6 (June 2022), pp. 251–263. ISSN: 1745-1353. URL: https://search.ieice.org/bin/summary.php?id=e105-c_6_251.
- [119] Juan Casas et al. “A Quantum Flux Parametron (QFP) 12-Bit Shift Register Capable of Stable Microwave Frequency Operation”. In: *Japanese Journal of Applied Physics* 30.12S (Dec. 1991), p. 3938. DOI: [10.1143/JJAP.30.3938](https://doi.org/10.1143/JJAP.30.3938). URL: <https://dx.doi.org/10.1143/JJAP.30.3938>.
- [120] J. Casas, R. Kamikawai, and R. Goto. “High-frequency operation of quantum flux parametron (QFP) based shift registers and frequency prescalers”. In: *IEEE Journal of Solid-State Circuits* 27.1 (1992), pp. 97–105. DOI: [10.1109/4.109561](https://doi.org/10.1109/4.109561).
- [121] N. Shimizu et al. “A new A/D converter with quantum flux parametron”. In: *IEEE Transactions on Magnetics* 25.2 (1989), pp. 865–868. DOI: [10.1109/20.92423](https://doi.org/10.1109/20.92423).
- [122] Y. Harada and J.B. Green. “High-speed experiments on a QFP-based comparator for ADCs with 18-GHz sample rate and 5-GHz input frequency”. In: *IEEE Transactions on Applied Superconductivity* 2.1 (1992), pp. 21–25. DOI: [10.1109/77.124924](https://doi.org/10.1109/77.124924).
- [123] Eiichi Goto, Willy Hioe, and Mutsumi Hosoya. “Physical limits to quantum flux parametron operation”. In: *Physica C: Superconductivity* 185-189 (1991), pp. 385–390. ISSN: 0921-4534. DOI: [https://doi.org/10.1016/0921-4534\(91\)92004-U](https://doi.org/10.1016/0921-4534(91)92004-U). URL: <https://www.sciencedirect.com/science/article/pii/092145349192004U>.
- [124] M G Castellano et al. “Deep-well ultrafast manipulation of a SQUID flux qubit”. In: *New Journal of Physics* 12.4 (Apr. 2010), p. 043047. DOI: [10.1088/1367-2630/12/4/043047](https://doi.org/10.1088/1367-2630/12/4/043047). URL: <https://doi.org/10.1088/1367-2630/12/4/043047>.
- [125] F Chiarello et al. “Superconducting qubit manipulated by fast pulses: experimental observation of distinct decoherence regimes”. In: *New Journal of Physics* 14.2 (Feb. 2012), p. 023031. DOI: [10.1088/1367-2630/14/2/023031](https://doi.org/10.1088/1367-2630/14/2/023031). URL: <https://doi.org/10.1088/1367-2630/14/2/023031>.
- [126] S Poletto et al. “Coherent oscillations in a superconducting tunable flux qubit manipulated without microwaves”. In: *New Journal of Physics* 11.1 (Jan. 2009), p. 013009. DOI: [10.1088/1367-2630/11/1/013009](https://doi.org/10.1088/1367-2630/11/1/013009). URL: <https://doi.org/10.1088/1367-2630/11/1/013009>.
- [127] Fabio Chiarello et al. “Superconducting tunable flux qubit with direct readout scheme”. In: *Superconductor Science and Technology* 18.10 (Aug. 2005), p. 1370. DOI: [10.1088/0953-2048/18/10/021](https://doi.org/10.1088/0953-2048/18/10/021). URL: <https://dx.doi.org/10.1088/0953-2048/18/10/021>.

- [128] G. S. Lee et al. “Superconducting race arbiter with subpicosecond timing discrimination”. In: *Appl. Phys. Lett.* 59.22 (Nov. 1991), pp. 2892–2894. ISSN: 0003-6951. DOI: [10.1063/1.105843](https://doi.org/10.1063/1.105843).
- [129] Yuki Yamanashi et al. “Evaluation of current sensitivity of quantum flux parametron”. In: *Supercond. Sci. Technol.* 30.8 (July 2017), p. 084004. ISSN: 0953-2048. DOI: [10.1088/1361-6668/aa73be](https://doi.org/10.1088/1361-6668/aa73be).
- [130] H.L. Ho et al. “A single QFP timing discriminator”. In: *IEEE Transactions on Applied Superconductivity* 3.1 (1993), pp. 2756–2759. DOI: [10.1109/77.233510](https://doi.org/10.1109/77.233510).
- [131] Nobuyuki Yoshikawa. “Superconducting Digital Electronics for Controlling Quantum Computing Systems”. In: *IEICE Trans. Electron.* 102-C (2019), pp. 217–223.
- [132] O. A. Mukhanov. “Energy-Efficient Single Flux Quantum Technology”. In: *IEEE Transactions on Applied Superconductivity* 21.3 (2011), pp. 760–769. DOI: [10.1109/TASC.2010.2096792](https://doi.org/10.1109/TASC.2010.2096792).
- [133] D. E. Kirichenko, S. Sarwana, and A. F. Kirichenko. “Zero Static Power Dissipation Biasing of RSFQ Circuits”. In: *IEEE Transactions on Applied Superconductivity* 21.3 (2011), pp. 776–779. DOI: [10.1109/TASC.2010.2098432](https://doi.org/10.1109/TASC.2010.2098432).
- [134] Naoki Takeuchi et al. “An adiabatic quantum flux parametron as an ultra-low-power logic device”. In: *Superconductor Science and Technology* 26.3 (Jan. 2013), p. 035010. DOI: [10.1088/0953-2048/26/3/035010](https://doi.org/10.1088/0953-2048/26/3/035010). URL: <https://doi.org/10.1088/0953-2048/26/3/035010>.
- [135] R. McDermott et al. “Simultaneous State Measurement of Coupled Josephson Phase Qubits”. In: *Science* 307.5713 (Feb. 2005), pp. 1299–1302. ISSN: 0036-8075. DOI: [10.1126/science.1107572](https://doi.org/10.1126/science.1107572).
- [136] Abraham G. Kofman et al. “Theoretical analysis of measurement crosstalk for coupled Josephson phase qubits”. In: *Phys. Rev. B* 75.1 (Jan. 2007), p. 014524. ISSN: 2469-9969. DOI: [10.1103/PhysRevB.75.014524](https://doi.org/10.1103/PhysRevB.75.014524).
- [137] T. L. Robertson et al. “Superconducting quantum interference device with frequency-dependent damping: Readout of flux qubits”. In: *Phys. Rev. B* 72 (2 July 2005), p. 024513. DOI: [10.1103/PhysRevB.72.024513](https://doi.org/10.1103/PhysRevB.72.024513). URL: <https://link.aps.org/doi/10.1103/PhysRevB.72.024513>.
- [138] Matthias Steffen et al. “Decoherence of floating qubits due to capacitive coupling”. In: *New Journal of Physics* 11.3 (Mar. 2009), p. 033030. DOI: [10.1088/1367-2630/11/3/033030](https://doi.org/10.1088/1367-2630/11/3/033030). URL: <https://doi.org/10.1088/1367-2630/11/3/033030>.
- [139] N. R. Werthamer. “Nonlinear Self-Coupling of Josephson Radiation in Superconducting Tunnel Junctions”. In: *Phys. Rev.* 147 (1 July 1966), pp. 255–263. DOI: [10.1103/PhysRev.147.255](https://doi.org/10.1103/PhysRev.147.255). URL: <https://link.aps.org/doi/10.1103/PhysRev.147.255>.

-
- [140] D. R. Gulevich, L. V. Filippenko, and V. P. Koshelets. “Microscopic Tunneling Model of Nb–AlN–NbN Josephson Flux-Flow Oscillator”. In: *J. Low Temp. Phys.* 194.3 (Feb. 2019), pp. 312–324. ISSN: 1573-7357. DOI: [10.1007/s10909-018-2106-x](https://doi.org/10.1007/s10909-018-2106-x).
- [141] Semenov V. K. Odintsov A.A and A. Zorinet B. “Specific problems of numerical analysis of the Josephson junction circuit.” In: *IEEE Transactions on magnetics* MAG-23 (1987), pp. 763–765.
- [142] A.I. Larkin and YuN Ovchinnikov. “Tunnel effect between Superconductors in an alternating field”. In: *Sov. Phys. JETP* 24 (1967), pp. 1035–1040.
- [143] A. A. Golubov and M. Yu. Kupriyanov. “Theoretical investigation of Josephson tunnel junctions with spatially inhomogeneous superconducting electrodes”. In: *J. Low Temp. Phys.* 70.1 (Jan. 1988), pp. 83–130. ISSN: 1573-7357. DOI: [10.1007/BF00683247](https://doi.org/10.1007/BF00683247).
- [144] Max Hofheinz et al. “Synthesizing arbitrary quantum states in a superconducting resonator”. In: *Nature* 459 (May 2009), pp. 546–549. ISSN: 1476-4687. DOI: [10.1038/nature08005](https://doi.org/10.1038/nature08005).
- [145] *SEEQC Design Rules*. <https://seeqc.com/chip-foundry-services>.
- [146] Daniel A Lidar. “Lecture notes on the theory of open quantum systems”. In: *arXiv preprint arXiv:1902.00967* (2019).
- [147] Daniel Manzano. “A short introduction to the Lindblad master equation”. In: *AIP Adv.* 10.2 (Feb. 2020), p. 025106. ISSN: 2158-3226. DOI: [10.1063/1.5115323](https://doi.org/10.1063/1.5115323).
- [148] N. Y. Haboubi and R. D. Montgomery. *The Theory of Open Quantum Systems*. Vol. 21. 5. Oxford, England, UK: Oxford University Press, Sept. 1992. DOI: [10.1093/ageing/21.5.381-a](https://doi.org/10.1093/ageing/21.5.381-a).
- [149] Piotr Szańkowski. “Introduction to the theory of open quantum systems”. In: *arXiv* (Sept. 2022). DOI: [10.48550/arXiv.2209.10928](https://doi.org/10.48550/arXiv.2209.10928). eprint: [2209.10928](https://arxiv.org/abs/2209.10928).
- [150] A. Isar, A. Sandulescu, and W. Scheid. “Lindblad master equation for the damped harmonic oscillator with deformed dissipation”. In: *Physica A* 322 (May 2003), pp. 233–246. ISSN: 0378-4371. DOI: [10.1016/S0378-4371\(02\)01828-9](https://doi.org/10.1016/S0378-4371(02)01828-9).
- [151] L. O. Castaños and A. Zuñiga-Segundo. “The forced harmonic oscillator: Coherent states and the RWA”. In: *Am. J. Phys.* 87.10 (Sept. 2019), p. 815. ISSN: 0002-9505. DOI: [10.1119/1.5115395](https://doi.org/10.1119/1.5115395).
- [152] Mika Sillanpää, Jae I. Park, and R. W. Simmonds. “Coherent quantum state storage and transfer between two phase qubits via a resonant cavity”. In: *Nature* 449.7161 (Sept. 2007), pp. 438–442. DOI: [10.1038/nature06124](https://doi.org/10.1038/nature06124).

- [153] S. J. Weber et al. “Mapping the optimal route between two quantum states”. In: *Nature* 511 (July 2014), pp. 570–573. ISSN: 1476-4687. DOI: [10.1038/nature13559](https://doi.org/10.1038/nature13559).
- [154] O. Mukhanov, V. Semenov, and K. Likharev. “Ultimate performance of the RSFQ logic circuits”. In: *IEEE Trans. Magn.* 23.2 (Mar. 1987), pp. 759–762. ISSN: 1941-0069. DOI: [10.1109/TMAG.1987.1064951](https://doi.org/10.1109/TMAG.1987.1064951).
- [155] K. Likharev and V. Semenov. “RSFQ logic/memory family: a new Josephson-junction technology for sub-terahertz-clock-frequency digital systems”. In: *undefined* (1991). URL: <https://www.semanticscholar.org/paper/RSFQ-logic%2Fmemory-family%3A-a-new-Josephson-junction-Likharev-Semenov/ae5b0f6732b93593115ac00b6873ec6912563e31>.
- [156] Timur V. Filippov et al. “Gray Zone and Threshold Current Measurements of the Josephson Balanced Comparator”. In: *IEEE Transactions on Applied Superconductivity* 31.5 (2021), pp. 1–7. DOI: [10.1109/TASC.2021.3063329](https://doi.org/10.1109/TASC.2021.3063329).
- [157] Michael Margraf. *QucsStudio – A Free and Powerful Circuit Simulator*. URL: <http://qucsstudio.de>.
- [158] *Ansys HFSS | 3D High Frequency Simulation Software*. URL: <https://www.ansys.com/products/electronics/ansys-hfss>.
- [159] *Sonnet Software*. [Online; accessed 28. Jan. 2023]. June 2022. URL: <https://www.sonnetsoftware.com>.
- [160] M. Wulf et al. “An unshunted comparator as a device for quantum measurements”. In: *IEEE Transactions on Applied Superconductivity* 13.2 (2003), pp. 974–977. DOI: [10.1109/TASC.2003.814117](https://doi.org/10.1109/TASC.2003.814117).
- [161] *Dry Systems - Nanoscience - Oxford Instruments*. [Online; accessed 5. Jan. 2023]. Jan. 2023. URL: <https://nanoscience.oxinst.com/dry-systems>.
- [162] *LD dilution refrigerator measurement system - Bluefors*. [Online; accessed 5. Jan. 2023]. Dec. 2020. URL: <https://bluefors.com/products/ld-dilution-refrigerator/#technical-specifications2>.
- [163] *LNF-LNC4_8F - Low Noise Factory*. [Online; accessed 13. Jan. 2023]. Jan. 2023. URL: https://lownoiseactory.com/product/lnf-lnc4_8f.

Scientific contributions

List of Publications

- **L. Di Palma**, A. Miano, P. Mastrovito, D. Massarotti, M. Arzeo, G.P. Pepe, F. Tafuri, and O. A. Mukhanov, “Discriminating the phase of a weak coherent tone with a flux-switchable superconducting circuit”.
In: *PRX Quantum*, under review
- H. G. Ahmad, **L. Di Palma**, R. Caruso, A. Pal, G. P. Pepe, M. G. Blamire, F. Tafuri, “Critical Current Suppression in Spin-Filter Josephson Junctions”.
In: *Journal of Superconductivity and Novel Magnetism*, 33 (2020), pp. 3043–3049.
DOI: <https://doi.org/10.1007/s10948-020-05577-0>.
- H. G. Ahmad, **L. Di Palma**, D. Massarotti, M. Arzeo, G. P. Pepe, F. Tafuri, O. A. Mukhanov and I. P. Nevirkovets. “Characterization of Lateral Junctions and Micro-SQUIDs Involving Magnetic Multilayers”.
In: *IEEE Transactions on Applied Superconductivity* (2023), pp.1-5.
DOI: <https://doi.org/10.1109/TASC.2023.3247361>.
- H. G. Ahmad, V. Brosco, A. Miano, **L. Di Palma**, M. Arzeo, D. Montemurro, P. Lucignano, G. P. Pepe, F. Tafuri, R. Fazio, and D. Massarotti, “A hybrid ferromagnetic transmon qubit: Circuit design, feasibility and detection protocols for magnetic fluctuations”.
In: *Physical Review B* 105 (2022), pp. 214522.
DOI: <https://doi.org/10.1103/PhysRevB.105.214522>
- H. G. Ahmad, V. Brosco, A. Miano, **L. Di Palma**, M. Arzeo, R. Satariano, R. Ferraiuolo, P. Lucignano, A. Vettoliere, C. Granata, L. Parlato, G. Ausanio, D. Montemurro, G. P. Pepe, R. Fazio, F. Tafuri and D. Massarotti, “Competition of Quasiparticles and Magnetization Noise in Hybrid Ferromagnetic Transmon Qubits”.
In: *IEEE Transactions on Applied Superconductivity* 33 (2023), pp. 1-6.
DOI: <https://doi.org/10.1109/TASC.2023.3243197>
- D. Salvoni, L. Parlato, M. Ejrnaes, F. Mattioli, A. Gaggero, F. Martini, G. Ausanio, D. Massarotti, D. Montemurro, H.G. Ahmad, **L. Di Palma**,

- F. Tafuri, R. Cristiano and G.P. Pepe, "Demonstration of single photon detection in amorphous Molybdenum Silicide / Aluminium nanostrip".
In: *IEEE Instrumentation Measurement Magazine* 24 (2021), pp. 69-74.
DOI: <https://doi.org/0.1109/MIM.2021.9491006>.
- A. Vettoliere, R. Satariano, R. Ferraiuolo, **L. Di Palma**, H. G. Ahmad, G. Ausanio, G. P. Pepe, F. Tafuri, D. Massarotti, D. Montemurro, C. Granata, and L. Parlato, "High-quality ferromagnetic Josephson Junctions based on Al-technology".
In: *Nanomaterials* 1.23 (2022).
DOI: <https://doi.org/10.3390/nano12234155>.
 - D. Salvoni, M. Ejrnaes, A. Gaggero, F. Mattioli, F. Martini, H. G. Ahmad, **L. Di Palma**, R. Satariano, X. Y. Yang, L. You, F. Tafuri, G.P. Pepe, D. Massarotti, D. Montemurro, and L. Parlato, "Activation Energies in MoSI/Al Superconducting Nanowire Single-Photon Detectors".
In: *Phys. Rev. Appl.* 18 (2022), pp. 014006.
DOI: <https://doi.org/10.1103/PhysRevApplied.18.014006>.
 - A. Vettoliere, R. Satariano, R. Ferraiuolo, **L. Di Palma**, H. G. Ahmad, G. Ausanio, G. P. Pepe, F. Tafuri, D. Montemurro, C. Granata, L. Parlato, and D. Massarotti, "Aluminum-ferromagnetic Josephson tunnel junctions for high-quality magnetic switching devices".
In: *Appl. Phys. Lett.* 120 (2022), pp. 262601.
DOI: <https://doi.org/10.1063/5.0101686>.
 - R. Satariano, L. Parlato, A. Vettoliere, R. Caruso, H. G. Ahmad, A. Miano, **L. Di Palma**, D. Salvoni, D. Montemurro, C. Granata, G. Lamura, F. Tafuri, G. P. Pepe, D. Massarotti and G. Ausanio, "Investigation of the Inverse Magnetic Hysteresis of the Josephson Supercurrent in Magnetic Josephson Junctions".
In: *IEEE Trans. Appl. Supercond.* 32 (2022), pp. 1800105.
DOI: [10.1109/TASC.2021.3129983](https://doi.org/10.1109/TASC.2021.3129983).
 - R. Satariano, L. Parlato, A. Vettoliere, R. Caruso, H. G. Ahmad, A. Miano, **L. Di Palma**, D. Salvoni, D. Montemurro, C. Granata, G. Lamura, F. Tafuri, G. P. Pepe, D. Massarotti and G. Ausanio, "Inverse magnetic hysteresis of the Josephson supercurrent: study of the magnetic properties of thin Niobium/Permalloy (Fe₂₀Ni₈₀) interfaces".
In: *Phys. Rev. B* 103 (2021), pp. 224521.
DOI: <https://doi.org/10.1103/PhysRevB.103.224521>.
 - R. Satariano, L. Parlato, A. Vettoliere, R. Caruso, H. G. Ahmad, A. Miano, **L. Di Palma**, D. Salvoni, D. Montemurro, C. Granata, G. Lamura, F. Tafuri, G. P. Pepe, D. Massarotti and G. Ausanio, "Unconventional magnetic hysteresis of the Josephson supercurrent in magnetic Josephson Junctions".

In: *2021 IEEE 14th Workshop on Low Temperature Electronics (WOLTE)* (2021), pp. 1-4.

DOI: 10.1109/WOLTE49037.2021.9555441

- L. Parlato, D. Salvoni, M. Ejrnaes, A. Gaggero, F. Mattioli, F. Martini, H. G. Ahmad, D. Massarotti, D. Montemurro, R. Ferraiuolo, **L. Di Palma**, R. Satariano, F. Tafuri and G. P. Pepe, “Superconducting Molybdenum Silicide nanowires for single photon detectors”.

In: *2021 IEEE 14th Workshop on Low Temperature Electronics (WOLTE)* (2021)

- H. G. Ahmad, D. Massarotti, V. Brosco, A. Pal, A. Miano, **L. Di Palma**, R. Satariano, R. Caruso, D. Montemurro, P. Lucignano, G. P. Pepe, R. Fazio, M. Blamire, F. Tafuri, “Electrodynamics of tunnel ferromagnetic Josephson junctions: dissipation mechanisms and study of noise fluctuations”.

In: *APS March Meeting*, S47. 007 (2021)

Conferences

- Workshop on Low-Temperature Electronics (WOLTE14), oral talk entitled: “Tunable Superconducting devices for digital phase detection”
- European Conference on Applied Superconductivity EUCAS 2021, poster contribution entitled: “Tunable Superconducting devices for digital phase detection”, which won the young researcher prize
- The 14th Italian Quantum Information Science Conference, oral talk entitled: “Discriminating the phase of a weak coherent tone with a flux-switchable superconducting circuit”